UNIVERSIDADE FEDERAL DE UBERLÂNDIA
INSTITUTO DE FÍSICA
PROGRAMA DE PÓS-GRADUAÇÃO EM FÍSICA

SYNTHESIS AND PHYSICAL CHARACTERIZATION OF $KNbO_3$-BASED ELECTRO-CERAMICS

Uberlândia, Minas Gerais, Brasil
October, 2021

Mykaelle Cristina Oliveira Silva

SYNTHESIS AND PHYSICAL CHARACTERIZATION OF $KNbO_3$-BASED ELECTRO-CERAMICS

Dissertação de Mestrado apresentada ao Programa de Pós-Graduação em Física da Universidade Federal de Uberlândia, como requisito parcial para obtenção de título de mestre em Física. Área de concentração: Física da Matéria Condensada.

Orientador: Prof. Dr. José de los Santos Guerra
Coorientador: Prof. Dr. Atair Carvalho da Silva

Uberlândia, Minas Gerais, Brasil
September, 2021

Ficha Catalográfica Online do Sistema de Bibliotecas da UFU
com dados informados pelo(a) próprio(a) autor(a).

S586 Silva, Mykaelle Cristina Oliveira, 1995-
2021 Synthesis and physical characterization of KNbO3-based electro-ceramics [recurso eletrônico] / Mykaelle Cristina Oliveira Silva. - 2021.

Orientador: José de los Santos Guerra.
Coorientador: Atair Carvalho da Silva.
Dissertação (Mestrado) - Universidade Federal de Uberlândia, Pós-graduação em Física.
Modo de acesso: Internet.
Disponível em: http://doi.org/10.14393/ufu.di.2021.690
Inclui bibliografia.
Inclui ilustrações.

1. Física. I. Guerra, José de los Santos,1972-, (Orient.). II. Silva, Atair Carvalho da,1989-, (Coorient.). III. Universidade Federal de Uberlândia. Pós-graduação em Física. IV. Título.

CDU: 53

Bibliotecários responsáveis pela estrutura de acordo com o AACR2:

Gizele Cristine Nunes do Couto - CRB6/2091

UNIVERSIDADE FEDERAL DE UBERLÂNDIA
Coordenação do Programa de Pós-Graduação em Física
Av. João Naves de Ávila, 2121, Bloco 1A, Sala 213 - Bairro Santa Mônica, Uberlândia-MG, CEP 38400-902
Telefone: (34) 3239-4309 - www.infis.ufu.br - cpgfisica@ufu.br

ATA DE DEFESA - PÓS-GRADUAÇÃO

Programa de Pós-Graduação em:	Física				
Defesa de:	Defesa de dissertação de Mestrado				
Data:	Vinte e Oito de Outubro de 2021	Hora de início:	09:00	Hora de encerramento:	11:40
Matrícula do Discente:	11922FIS004				
Nome do Discente:	Mykaelle Cristina Oliveira Silva				
Título do Trabalho:	Synthesis and physical characterization of $KNbO_3$-based electro-ceramics				
Área de concentração:	Física				
Linha de pesquisa:	Propriedades magnéticas, estruturais e elétricas de materiais				
Projeto de Pesquisa de vinculação:	Síntese e investigação das propriedades físicas de filmes finos e cerâmicas ferroelétricas nano-estruturadas				

Reuniu-se por meio de Videoconferência a Banca Examinadora, designada pelo Colegiado do Programa de Pós-graduação em Física, assim composta: Professores Doutores: Daiane Damasceno Borges - INFIS/UFU, Elton Carvalho de Lima - UFT e José de los Santos Guerra - INFIS/UFU orientador da candidata.

Iniciando os trabalhos o presidente da mesa, Dr. José de los Santos Guerra, apresentou a Comissão Examinadora e a candidata, agradeceu a presença do público, e concedeu a Discente a palavra para a exposição do seu trabalho. A duração da apresentação da Discente e o tempo de arguição e resposta foram conforme as normas do Programa.

A seguir o senhor(a) presidente concedeu a palavra, pela ordem sucessivamente, aos(às) examinadores(as), que passaram a arguir o(a) candidato(a). Ultimada a arguição, que se desenvolveu dentro dos termos regimentais, a Banca, em sessão secreta, atribuiu o resultado final, considerando o(a) candidato(a):

Aprovada

Esta defesa faz parte dos requisitos necessários à obtenção do título de Mestre.

O competente diploma será expedido após cumprimento dos demais requisitos, conforme as normas do Programa, a legislação pertinente e a regulamentação interna da UFU.

Nada mais havendo a tratar foram encerrados os trabalhos. Foi lavrada a presente ata que após lida e achada conforme foi assinada pela Banca Examinadora.

Documento assinado eletronicamente por **José de los Santos Guerra**, **Professor(a) do Magistério Superior**, em 28/10/2021, às 13:49, conforme horário oficial de Brasília, com fundamento no art. 6º, § 1º, do Decreto nº 8.539, de 8 de outubro de 2015.

Documento assinado eletronicamente por **ELTON CARVALHO DE LIMA**, **Usuário Externo**, em 28/10/2021, às 17:41, conforme horário oficial de Brasília, com fundamento no art. 6º, § 1º, do Decreto nº 8.539, de 8 de outubro de 2015.

Documento assinado eletronicamente por **Daiane Damasceno Borges**, **Professor(a) do Magistério Superior**, em 28/10/2021, às 22:38, conforme horário oficial de Brasília, com fundamento no art. 6º, § 1º, do Decreto nº 8.539, de 8 de outubro de 2015.

A autenticidade deste documento pode ser conferida no site https://www.sei.ufu.br/sei/controlador_externo.php?acao=documento_conferir&id_orgao_acesso_externo=0, informando o código verificador **3134130** e o código CRC **F3D702C6**.

Referência: Processo nº 23117.071679/2021-42 SEI nº 3134130

Dedico este trabalho à minha família, singularmente ao meu amado pai (*in memorian*).

ACKNOWLEDGEMENTS

Primeiramente agradeço à Deus por toda força e conforto que tem me fornecido durante todo esse tempo, por me mostrar que Seu amor por mim me faz suportar dificuldades que nunca imaginei que conseguiria enfrentar sã, e que tudo tem um propósito, seja ele oriundo de qual for a situação.

Minha eterna gratidão à minha família, que me deram todo apoio necessário nesses anos, o qual foi fundamental para minha formação e a conquista de mais um título. Um agradecimento especial ao meu pai. Sei que, de onde estiver, o senhor está torcendo por mim e continua me guiando no meu caminho. Serei eternamente grata por tudo que fez por mim. Eu o amo de todo o meu coração!

Agradeço ao meu orientador Pro. Dr. José de los Santos Guerra e ao meu coorientador Prof. Dr. Atair Carvalho da Silva pelos ensinamentos, compreensão e suporte fornecidos. Agradeço também a todos do Grupo de Ferroelétricos e Materiais Multifuncionais (GFeMM) pelas trocas de conhecimento da área, discussões que foram riquíssimas para o desenvolvimento do trabalho, e pelos momentos especiais vividos que ficarão em minha memória. Foi um prazer trabalhar com todos vocês!

Por fim, aos professores do Instituto de Física (INFIS) da UFU e todos os profissionais que contribuíram para a realização deste trabalho, obrigada!

RESUMO

Os materiais ferroelétricos baseados em $KNbO_3$ têm sido amplamente investigados como resultado de muitas propriedades físicas interessantes que os tornam adequados para o desenvolvimento de componentes eletrônicos multifuncionais. Em particular, soluções sólidas ferroelétricas de $(1-x)KNbO_3 - xBaNi_{1/2}Nb_{1/2}O_{3-\delta}$ (KBNN) têm recebido especial atenção para aplicações ópticas, inclusive para dispositivos fotovoltaicos de alto desempenho. Neste trabalho, cerâmicas de KBNN foram produzidas por meio do método de sinterização convencional (reação de estado sólido), e as propriedade estruturais, microestruturais, elétricas e ópticas foram investigadas. Os resultados foram analisados e discutidos considerando o efeito dos defeitos estruturais de vacâncias de oxigênio nesses materiais e do tamanho do grão, no caso específico da resposta elétrica observada. Os resultados obtidos sugerem que os materiais propostos, baseados em óxidos ferroelétricos semicondutores com estrutura perovskita, são uma boa alternativa para aplicações em células solares.

Palavras-chave: cerâmicas, $KNbO_3$, vacâncias, ferroelétricos, dispositivos fotovoltaicos.

ABSTRACT

$KNbO_3$-based ferroelectric materials have been largely investigated as a result of many interesting physical properties that make them suitable for designing multifunctional electronic components. In particular, ferroelectric $(1-x)KNbO_3 - xBaNi_{1/2}Nb_{1/2}O_{3-\delta}$ (KBNN) solid solutions have received special attention for optical applications, including for high-performance photovoltaic devices. In this work, KBNN ceramics were produced via conventional sintering process (solid-state reaction), and the structural, microstructural, electrical and optical properties were investigated. The results were analyzed and discussed in terms of the effect from structural oxygen vacancy defects in such materials and from the grain size, in the specific case of the observed electrical response. Overall, the results suggest these perovskite-structured semiconducting ferroelectric oxides as a good alternative for solar cell applications.

Keywords: ceramics, $KNbO_3$, vacancies, ferroelectrics, photovoltaic devices.

LIST OF FIGURES

LIST OF TABLES

CONTENTS

INTRODUCTION

Conventional energy sources based on coal, gas and oil have been worldwide extensively used over several centuries for the improvement of the countries' economy. However, from another perspective, many negative impacts of these resources on the environment have forced the human body to use them within certain limits and have turned-on our thinking toward new alternatives, which include renewable energy resources. Among them, photovoltaic (PV) devices have been considered one of the most sustainable renewable energy sources, which can be helpful for the mitigation of the greenhouse effect and the global warming effect [1, 2]. Over the last 10 years, perovskite-structured materials made from low-cost and non-toxic elements have emerged as potential candidates for photovoltaic materials. In fact, perovskite-based solar cells have experienced a promising growth over the last few years. Since 2010, for instance, the efficiency of perovskites has increased from around 5% up to 22%, as can be seen in figure 1, according to Green and Ho-Baillie [1].

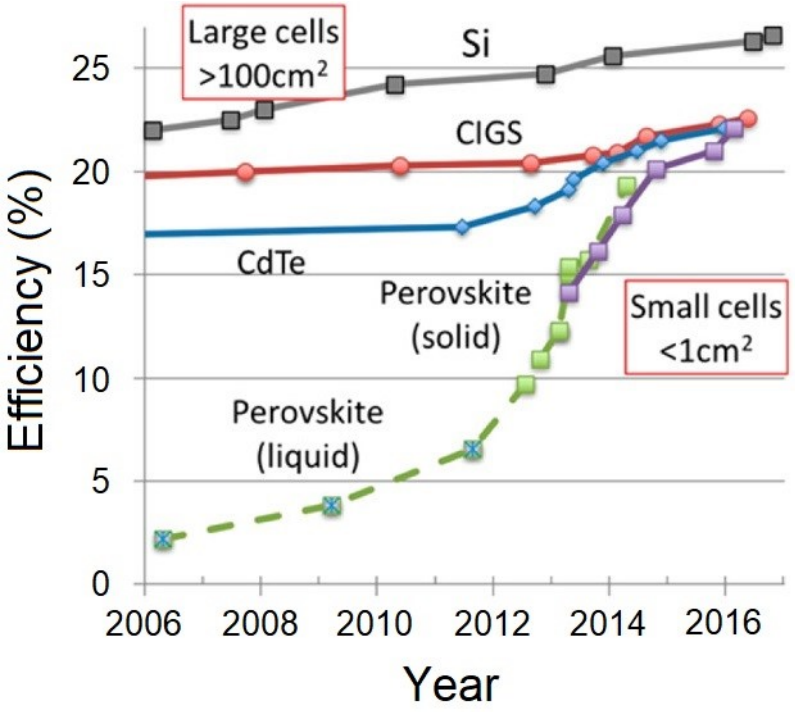

Figure 1 – Evolution of standard (Si, CdTe, and CIGS) and perovskite cells efficiency over the last and current decade. Source: adapted from [1].

Nevertheless, along with the outstanding advantages of these PV resources, some deficiencies, such as stability and the rapid degradation, are still present. In this context, ferroelectric perovskite systems based on potassium niobate ($KNbO_3$) have gained atten-

tion because of their multifunctional properties, making them potential candidates for technological applications, mainly in PV cells [2–4]. A common problem in most photovoltaic ferroelectric materials is the wide bandgap they present (typically higher than 3.0 eV) [5–9], which limits their light absorption mainly in the ultraviolet (UV) region that it is equivalent to absorbing only 20% of the solar spectrum. However, despite the great interest in semiconductor ferroelectrics for photovoltaic applications, ferroelectric oxides with an appropriate bandgap to solar energy had not been reported until recently. One approach to narrow the bandgap is to control the chemical ordering of the species, i.e., introducing several types of ions into the B-site of the perovskite structure and promoting oxygen vacancies by mixing solid-solutions. In this context, previous studies have been conducted to the modification of the electronic structure of these materials in order to produce bandgap ranges that may cover a larger spectrum percentage [10–14].

In particular, introducing the Ni^{2+} ion into the B-site of the perovskite structure and creating oxygen vacancies by mixing $BaNi_{0.5}Nb_{0.5}O_{3-\delta}$ (BNN) with $KNbO_3$ (KN) [in 20 μm thick-films] effectively allows for a tunable bandgap of around 1.1–2.0 eV [10,11], which is too much lower than the reported bandgap for the pure $KNbO_3$ ceramic ($\sim$ 3.8 eV) [8]. This is the key point behind the observation that KBNN-based materials absorb three to six times more solar energy than conventional ferroelectric systems [10], although the real mechanism still remains unclear. Previous investigations, reported by Wang & Rappe [12], elucidated the origin of this bandgap narrowing from first-principles calculations. The maximum valence band is composed by hybridized Ni-3d and O-2p orbitals, while the minimum conduction band is occupied by Nb-4d states. Hence, they suggested that the filled Ni-3d gap states in the KN–BNN ceramics play an important role in narrowing the bandgap, which provides a guide for designing and optimizing new FE photovoltaic materials. Thus, these compositions based on $(1-x)KNbO_3-xBaNi_{1/2}Nb_{1/2}O_3$ (KBNN) emerged as lead-free advanced systems due to the excellent photophysical properties, including enhanced photocatalytic activity [10, 13].

Others researches have encouraged the development of theoretical and experimental works based on bandgap tuning of perovskite compounds, which include the $KNbO_3$ system. In this way, systematic bandgap narrowing was reported in different solid solutions, such as $(1-x)KNbO_3 - xBa(Co_{0.5}Nb_{0.5})O_{3-\delta}$ (KBCNO), which shifts down to 2.4 eV [14]. Very recently, alternative lead-free systems have been also studied, such as $KNb_{1-x}Fe_xO_{3-\delta}$ [15] and $(1-x)KNbO_3 - xBa(Nb_{0.5}Fe_{0.5})O_3$ (KBNFO), which show a reduction in the bandgap from 3.2 eV to 1.74 eV [16]. It can be observed that all these ferroelectric oxides based on $KNbO_3$ with lower bandgaps are characterized by the presence of a large concentration of oxygen vacancies. Indeed, such defects strongly affects the polarization switching phenomenon in ferroelectrics and can also trap the photo-excited carriers and, consequently, increase the charge recombination rate. Therefore, since oxygen vacancies seem to be a key factor in both ferroelectric and photovoltaic properties

this mechanism was the main motivation in the present work for the investigation of alternative strategies, which lead to reduce the bandgap in the proposed materials while preserving their ferroelectric properties.

According to the reported work in the literature up today, despite the interest in the study of the optical properties in KBNN-based materials, it can be seen that less effort has been devoted to the understanding of the relationship between microstructural and electrical response in the original $KNbO_3 - BaNi_{1/2}Nb_{1/2}O_3$ (KBNN) system. However, this study could be crucial in order to get additional insights into its final photophysical properties [10]. In this context, the aim of the present dissertation is to synthesize KBNN-based electro-ceramics and investigate their physical properties, focusing on the influence of the oxygen vacancy concentration on the structural, microstructural as well as electrical and optical properties, where the effect from grain-size is also evaluated. Moreover, one of the aims of this investigation is to contribute for the scientific community the good practice of preparing $KNbO_3$–based compounds via conventional routes and to fill the gap that exists in the literature about the electric properties of this compound, due to the presented difficulties in the synthesis of the samples and low densification they present.

The dissertation structure has been organized as follows:

Chapter 1 presents a literature review about the theoretical insights of the ferroelectric materials, which includes the historic context of ferroelectricity and discussion of the main properties, characteristics and phenomena related to these materials. Furthermore, it presents a review of the KBNN system, discussing its importance, optical behavior and applications with a focus on photovoltaic devices, where a brief physical theory about optical mechanisms is presented.

Chapter 2 describes the experimental section, presenting the methods used for the synthesis of the samples as well as the main characterization techniques for the analyzed physical properties.

Chapter 3 includes the results corresponding to the studied KBNN binary systems. The discussions have been analyzed evaluating the effect from the oxygen vacancy concentrations of the ceramics through the studied theories reported in the literature.

Chapter 4 presents the main conclusions of this research work.

Finally, in **Chapter 5**, the future perspectives are presented.

1 LITERATURE REVIEW

1.1 Ferroelectricity

1.1.1 History and definition

After 100 years of the discovery of ferroelectricity in 1921 [17], the ferroelectric materials are still widely studied due to the development and emergence of new materials over the years. Consequently, the understanding of the their physical properties that could contribute for innovation and development of new technological applications remains a priority. The main characteristic of theses class of materials, also classified as typical dielectrics, is that they have a spontaneous electrical polarization in the absence of an electric field, in a wide temperature range, with the ability to reverse the polarization direction under an alternate applied electric field [18].

Ferroelectrics can be basically classified into three crystalline structure types, according to the atomic arrangement in the structural unit-cell: perovskite, tungsten-bronze and bismuth layered structures ferroelectrics (so-called Aurivillius compounds) [19]. Between them, probably the most studied one is the perovskite structure, not only because of the simplest structural arrangement, in comparison with the other, but also because of the very interesting physical properties it manifests. Ferroelectric oxides with perosvkite structure include, for instance, conventional ferroelectric systems such as the barium titanate ($BaTiO_3$, BT) and lead zirconate titanate ($Pb(ZrTi)O_3$, PZT). The perovskite structure, presented in figure 2, is commonly represented by a general chemical formula given in the form of ABO_3, where the A-site cations (with larger ionic radius) are located at the corners, the B-site cations (with smaller ionic radius) are body centered with the oxygen (O) anions faces centered forming an octahedral structure (O_6) surrounding the B-site cations [20].

According to the chemical bonding, ferroelectrics are also classified as “proper“ and “improper“, in which classes the ferroelectricity is dominated by different mechanisms [21]. Most of the ferroelectric perovskites belong to the “proper” class, where the ferroelectricity can be revealed in two ways: *i*-covalent bonds and *ii*- lone-pair mechanism. For the first one to occur it is necessary that the transition metal ions (B-site cations) have an empty d^0 orbital [1], since it will allow the formation of strong covalent bonds with one or more oxygen ions. In this mechanism, a virtual transfer of electrons from oxygen to the transition metal

[1] But it does not mean that all perovskite oxides with empty d-shell transition metal ions must exhibit ferroelectricity.

ions occurs, thus filling the empty d layers [22, 23]. These bonds lead to a distortion of the unit-cell, where the B-cations are displaced along one of the diagonal directions of the cubic structure, or even they can move along the axial-directions (up, down, left or right), inside of the O_6 octahedra (the one in which always tends to minimize its energy). This mechanism promotes a center of charge imbalance and, hence, the occurrence of the electric dipoles [20]. An example of this polarization mechanism is shown in the same figure 1, and can be observed in the $BaTiO_3$.

On the other hand, in the lone-pair mechanism the ferroelectricity occurs due to the A–O hybridization (involving the A-site cations and oxygens). In this case, the mechanism involves the orbitals with a ns^2 valence electron configuration, where the two electrons (so-called as lone-pair) participate in chemical bonds using (sp)-hybridized states (such as sp^2 or sp^3) [2], thus causing a displacement of the A-site ions from the centrosymmetric positions with respect to the surrounded oxygen ions. As a consequence, a distortion in the oxygen octahedra is observed [24]. Ferroelectric systems such as $BiMnO_3$ and $BiFeO_3$ are some kind materials that manifest lone-pair type ferroelectricity [21].

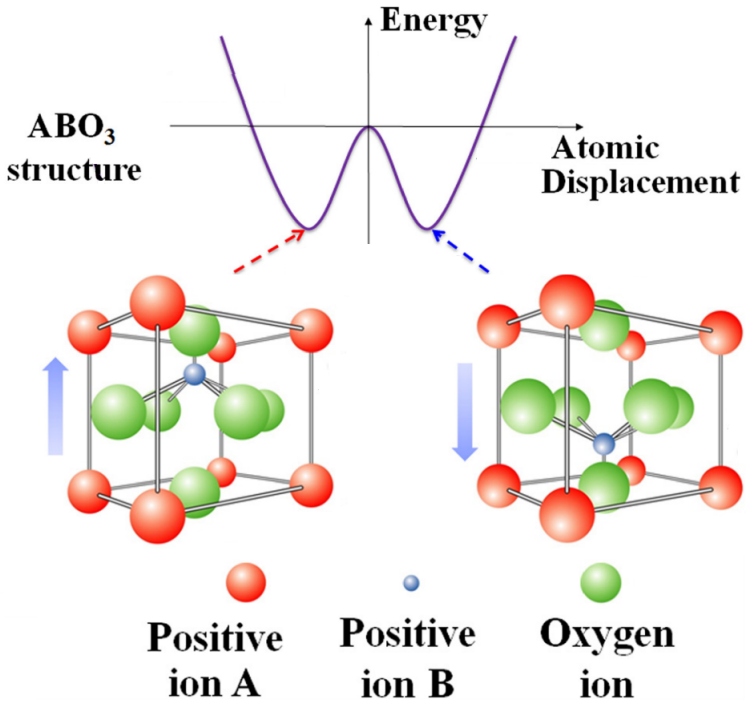

Figure 2 – Illustration of the unit-cell of a perovskite structure ABO_3 ferroelectric system. A double-well model as a function of the position of the B-site ion, between the oxygen anions, is presented. Source: adapted from [20].

For those system, however, where the ferroelectrity manifests itself by others mechanisms (called order parameters) that have others physical meaning and phase transition

[2] This tendency is also not always true, these two electrons may not participate in such bonding in some materials.

properties, i.e. the polarization originates from a complex lattice distortion, are known as "improper" ferroelectrics. The class of ferroelectricity includes the geometric, electronic, and magnetic ferroelectrics [21,25,26]. Details about these types of distortion mechanisms are still intriguing and confusing up today, and researchers are developing theoretical models and performing sophisticated experimental procedures in order to better understand the real mechanism behind this effect. For example, geometric ferroelectricity is known to be induced by structural distortions, as is the case of the $YMnO_3$. A possible reason is that the MnO_5 bi-pyramids lean towards a greater packing of the lattice atoms causing an approximation of the oxygen ions to the Y cations, thus forming the electric dipoles and, therefore, the occurrence of ferroelectricity [21,26]. On the other hand, electronic ferroelectricity is a proposed theoretical model [27], where the non-symmetric charge ordering is the responsible for the induced the electric polarization. In this case, the ferroelectricity originates from strong electronic correlations, in which charge carriers become localized, forming a periodic structure (charge-ordered state) [21,23,26,28]. One well-known example of this material is the $LuFe_2O_4$, where the Fe^{2+} and Fe^{3+} ions coexist in the same quantity (and are located in the same crystallographic site) generating a charge frustration. It is believed that this frustration is the cause of the ordering of the different Fe ions, because the charge centers of both ions do not coincide in the unit-cell of the structure and, therefore, allowing the presence of electrical dipoles [27,28].

Finally, in the magnetic ferroelectrics, the ferroelectricity only exists when there is a certain magnetic ordering. Therefore, the ferroelectric phase transition is accompanied by a magnetic transition and the polarization may be induced by applying an electric field in a specifc crystallographic direction. For example, in the $TbMnO_3$ [29] a magnetic ordering emerges at $T \approx 41$ K, and at a lower temperature ($T \approx 28$ K) this magnetic phase goes through a structural change, being this magnetic structural distortion the responsible for the ferroelectricity to appears [30]. This class of materials are commonly called multiferroics, where the ferroelectric and magnetic properties are strongly coupled, and have become promising materials for the development of multifunctional devices [26,29]. Improper ferroelectrics differ significantly from the proper ones in many of their physical properties such as dielectric response and lattice vibration properties, where dielectric anomalies, phonon spectrum near the transition point, among other observed anomalies still remains unclear [25,26,31]. In this work, only the first type of the abovementioned ferroelectrics (the "proper" class) will be studied.

1.1.2 Physical properties

1.1.2.1 Ferroelectric Domains

When the dipoles are oriented in the same direction in a material, the electrostatic energy of the system is extremely large and the system becomes very unstable. Therefore,

the natural is that the system always tends to minimize its potential energy (or the dipole interaction energy) forming domains [32]. Ferroelectric domains are volume regions in the material grains of the material where all the electric dipoles (in each individual domain) are oriented in the same direction, so that it presents a uniform spontaneous polarization. The orientation of the polarization changes between the different individual domains [18] and, therefore, ferroelectric domains may have different polarization orientations. Figure 3 presents a schematic representation of the polarization direction for each domain, as a result of the uniform dipoles orientation.

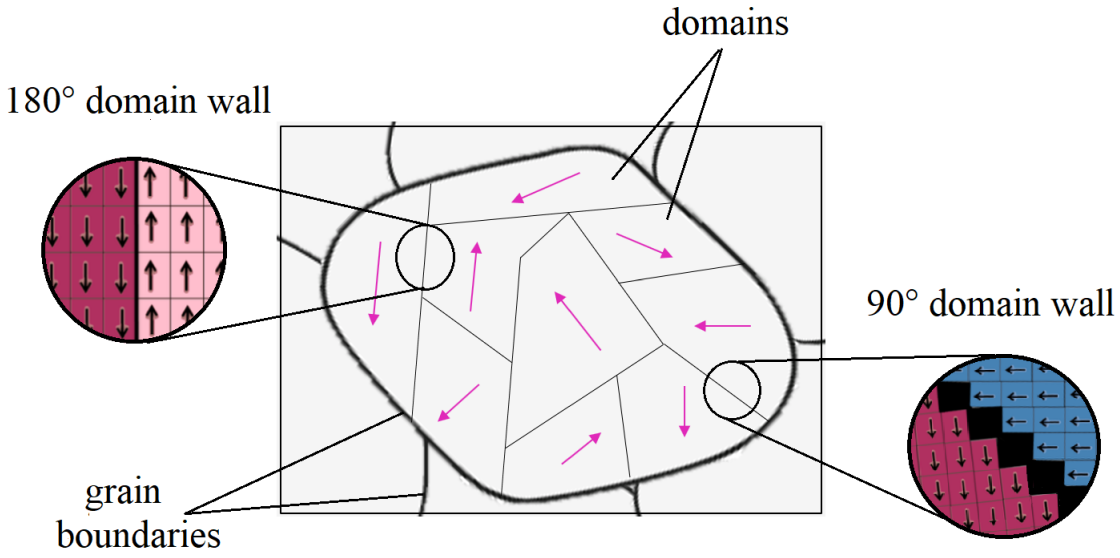

Figure 3 – Representation of domain orientations in a grain with a magnification in two characteristic domain walls separating lattices with anti-parallel (180°) and perpendicular (90°) polarizations. Source: adapted from [33].

These regions (domains) are separated by interfaces commonly called domain walls, where a gradual change in the dipoles orientation is observed, as can be seen in Figure 3 (represented by black regions in the magnified areas) [18, 33]. The types of domain walls that can occur depend on the symmetry of both non-ferroelectric and ferroelectric phases in the material, and figure 3 also shows the two most common to arise. Those domain walls which separate adjacent domains with opposite polarization orientation are called 180° domain walls (left side) and those which separate regions with spontaneous polarization whose orientation is perpendicular to each other are called 90° domain walls (right side). In order to reduce the elastic energy generated by the strain near the wall, the domain wall has the tendency to decrease its width. Therefore, a ferroelectric domain wall is very thin and its thickness is close to the size of few lattice unit-cells [18, 33].

1.1.2.2 Hysteresis Loop

Another important characteristic of ferroelectrics is the occurrence of the ferroelectric hysteresis loop, which is a consequence of the domain-wall switching [18]. Different to "conventional" dielectric materials, in which the polarization is a linear function of the applied electric field, ferroelectric materials are characterized by having a non-linear dependence between the polarization vector and the electric field and a non-linear behavior is observed in the hysteresis loop (P-E curve). In principle, the hysteresis loop is unique for each ferroelectric material, being the fingerprint and from which, the ferroelectricity can be directly identified [18,34]. Figure 4 shows the most common ferroelectric hysteresis loop observed in classic ferroelectric systems [34].

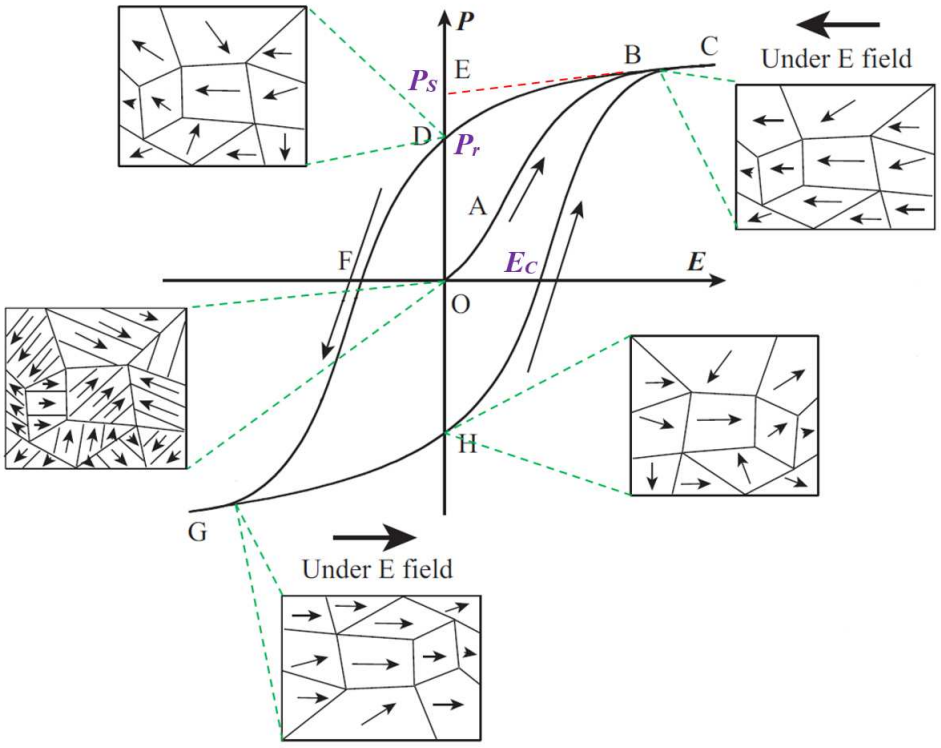

Figure 4 – Representation of the hysteresis loop typical of a ferroelectric material, given by the non-linear dependence of the polarization with the applied electric field. Source: adapted from [34].

In the initial state, without the application of the electric field ($\vec{E}$), the domains (or dipoles) are distributed in such a way that the polarization is randomly oriented; so that there is no macroscopic polarization (point O), leading to a virgin state of the material [3]. Applying small alternate electric field values with constant rate, the polarization increases

[3] Even the ferroelectric material already has spontaneous polarization without application of the electric field, initially, it is null, because adding all the directions of the polarization vectors, the macroscopic polarization becomes zero.

linearly with the electric field amplitude. This is because, in this region, the field is not strong enough to switch those domains that are in an unfavorable direction of polarization (region OA). As the electric field gradually increases, the polarization is induced and a portion of the domains (which have a polarization direction opposite to the direction of the electric field) starts to be oriented (segment AB) of nonlinear form until all the domains are totally aligned; i. e. when the material reaches a saturation state (segment BC) where the energy is enough to orientate all (or almost all) the dipoles in the direction of $\vec{E}$ (segment BC). Once all the domains are aligned (point C), in theory, the material is likely composed of a 'single domain'. As the electric field decreases, some domains will disorient back, decreasing the polarization but $\vec{P}$ does not return to zero.

If $\vec{E}$ is reduced to zero, most of the domains remain oriented leading the material to exhibit a remnant polarization P_r (point D). From the extrapolating of the saturation stretch to the polarization axis, the spontaneous polarization P_s (point E) can be obtained. In principle, for a perfect ferroelectric, the remnant and spontaneous polarization should have the same value, [4] ,but due to defects and impurities that are presented in the material this does not occur (P_r and P_s could be different). To reach a zero polarization state, i. e. $P_r = 0$, the electric field must be reversed and increased in the opposite direction to the previous one (point F) forcing the dipoles to change the direction. Such field strength is called the coercive field (E_c) and it represents the energy needed to depolarize the material. If the electric field continues to increase in the opposite direction, a similar alignment of the polarization will be observed in this direction (point G). Finally, by reversing the direction of the field once again, the ferroelectric hysteresis cycle is completed [18, 34].

Therefore, the characteristic parameters such as the spontaneous polarization (P_s), remnant polarization (P_r), and coercive field (E_c) parameters can be determined from the typical ferroelectric hysteresis loop. For an ideal ferroelectric material the observed hysteresis cycles should be symmetric, that is to say $+E_c = -E_c$ and $+P_r = -P_r$. However, in practice, these parameters appear to be different and the loop's shape may be affected by several factors such as the presence of charged defects, mechanical stresses, and others, most of which are closely related to the preparation conditions. Therefore, the hysteresis loop provides additional support for the comprehension of the structural and microstructural properties of the sample [34].

1.1.2.3 Phase Transition

Another important property that characterizes ferroelectric materials is the phase transition, which is related to a structural change of the material that occurs at a certain critical temperature known as the Curie point (T_c). At T_c, the material passes through a

[4] In polycrystalline materials, true spontaneous polarization equal to that of a single crystal can never be reached. This way, it is more correct to speak of saturated rather than of spontaneous polarization

transition from a high-temperature paraelectric order to a low-temperature order. While below the Curie temperature the material maintains a long-order dipolar interaction, above T_c it no longer exhibits the ferroelectricity phenomenon due to small distortions caused in the lattice, which change the structural symmetry. At the high-temperature paraelectric phase, a higher symmetry disordered structure is observed where the polarization vanishes to zero. In the ferroelectric phase, however, a more ordered and low low symmetry structure is observed [5]. It is noteworthy that Curie temperature only determines the temperature at which a paraelectric-ferroelectric phase transition occurs.

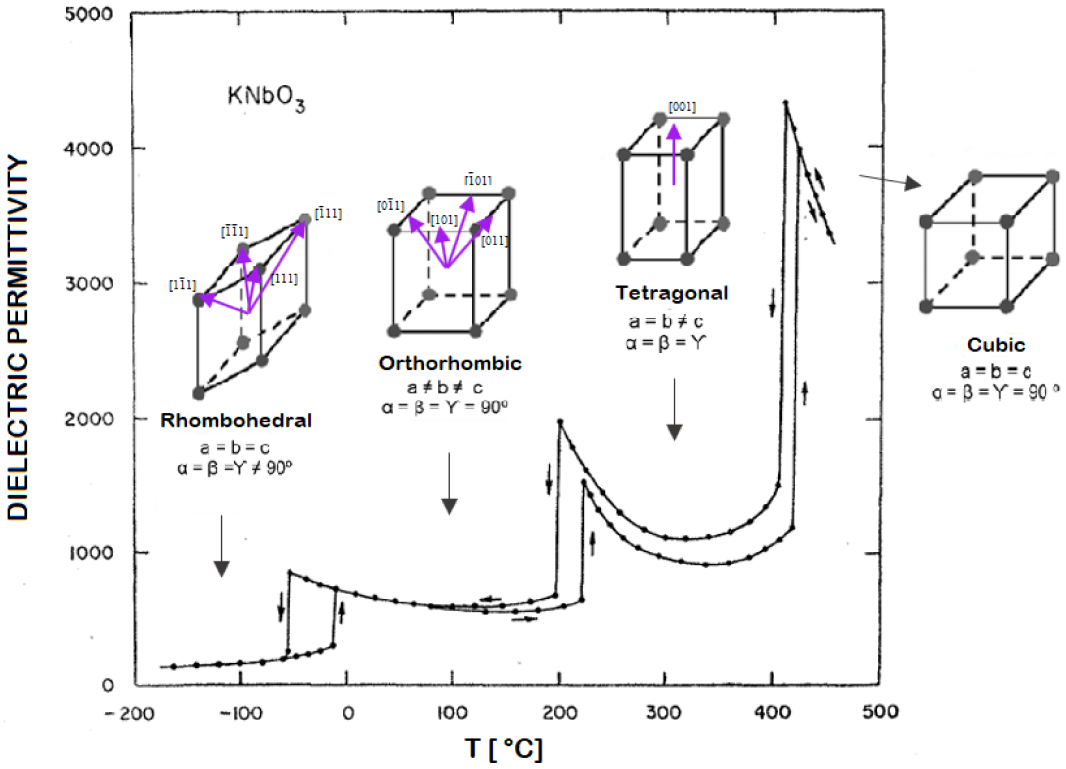

Figure 5 – Temperature dependence of the dielectric permittivity (ε) for the $KNbO_3$ system. The purple arrows represent the directions that the dipoles can assume to form the different structural symmetries of the unit-cell in the perovskite structure: cubic, tetragonal, orthorhombic and rhombohedral. Source: adapted from [35].

If there are two or more ferroelectric phases in the material, then the temperature of this transformation is always denominated as a transition temperature [18]. For example, the Curie point of the potassium niobate ($KNbO_3$) system is found to be around 435°C, at which the paraelectric-ferroelectric phase transition occurs. However, the $KNbO_3$

[5] Remark: some ferroelectric crystals, such as $LiH_3(Se0_3)_2$ (lithium trihydrogen selenite) and $BaCoF_4$ family, among others, do not have Curie temperatures because they maintain the ferroelectric state until their decomposition temperatures [18].

has three ferroelectric phases below this temperature [35]. The sequence of the phases transitions with increasing temperature is given by: Rhombohedral (below -10 °C), Orthorhombic (below 225 °C), Tetragonal (below 435 °C) and Cubic (above 435°), where the cubic-phase is paraelectric while the other ones are ferroelectrics [18, 35, 36]. Figure 5 shows the dielectric permittivity vs. temperature for the $KNbO_3$, where the three abovementioned transitions are clearly presented.

When the temperature of the ferroelectric material is close to T_c, the crystal structure undergoes changes, and such changes are characterized by a peak in the dielectric permittivity, which presents its maximum value close to the Curie point. This phenomenon is usually known as 'dielectric anomaly', when compared to the dielectric response of ferroelectrics with that for conventional dielectrics. This temperature dependence on the dielectric permittivity (or dielectric constant), in a "normal" ferroelectric, can be described by Curie-Weiss law [18]:

$$\varepsilon_r = \frac{\varepsilon_0 + C}{(T - T_0)} \tag{1.1}$$

where ε_0 is the vacuum dielectric permittivity in vacuum, C is the Curie-Weiss constant, T is the absolute temperature and T_0 represents the Curie-Weiss temperature (T_0 is different to T_c).

In the next section will be presented the KBNN system revealing its main physical characteristics, including some of the most important applications in the electronic industry.

1.2 KBNN System

Due to the current demand from the electro-electronic industry for the production of higher efficiency photovoltaic (PV) devices [37], there has been increasing interest of the scientific community on the new materials development with improved properties for application as photo-absorber in PV cells [38–40]. In particular, considering the new environmental protection rules imposed, e.g., by the European Union (EU) [41], and the worldwide efforts for using clean energy sources, ecofriendly (heavy metals-free) compounds appear as an alternative to substitute materials containing hazardous and high toxicity elements [42]. Over the last 10 years, a large amount of single-phase and composite solid solutions, made from low-cost and non-toxic elements, have been investigated [43]. Among them, materials based on the $KNbO_3$ (KNO) ferroelectric system have stood out thanks to their multifunctional properties, making them potential candidates for practical applications, mainly in photovoltaic devices [2–4].

Currently, besides of the already known physical properties of the ferroelectric materials like the piezoelectricity and pyroelectricity, other properties related to light absorption have been drawing attention [10]. Those that have optical properties and are called photoferroelectrics [44]. From the fundamental point of view, photoferroelectrics present a strong coupling between light absorption and other functional properties, which can provide a unique combination of semiconducting and ferroelectric properties. Therefore, the combination of these properties allows the creation of new multifunctional materials, thus expanding their applications and attracting the development of novel multifunctional devices such as multi-source energy harvesters and optoelectronic devices [45, 46].

The perovskite oxides better known as $BaTiO_3$, $SrTiO_3$ e $PbTiO_3$ have a wide bandgap (2,7 - 4 eV) in the ultraviolet (UV), which allows just a maximum use of 20% of the solar spectrum [10, 47, 48]. Thereby, studies have been done to modify the electronic structure of these materials to produce band ranges that may cover a larger percentage of the spectrum [10]. In particular, $(1-x)KNbO_3 - xBaNi_{1/2}Nb_{1/2}O_{3-\delta}$ (KBNN) solid solutions have been revealed as promising systems due to their excellent photophysical properties, including enhanced photocatalytic activity [10, 13]. The reason is that the system exhibits not only the expected intrinsic ferroelectric response, but also, a wide interval of direct bandgaps, ranging from 1.1 eV up to around 3.8 eV, depending on the considered stoichiometric ratio ($Ba/K = x/1-x$), making it a potential system for applications in solar cells, intended for photocatalysis, based on ferroelectric semiconductors [38, 44, 49, 50]. This is the key point behind the observation that KBNN-based materials absorb three to six times more solar energy than conventional ferroelectric systems [10], although the real mechanism still remains unclear.

The KBNN system is a ferroelectric oxide with a perovskite structure whose phase transition characteristics have been already reported [10, 11, 51, 52]. With increasing x in the nominal composition, the crystalline structure of KBNN is changed from rhombohedral to orthorhombic, from orthorhombic to tetragonal, and then from tetragonal to cubic structure [53]. Results reveal a weakly tetragonal structure at room temperature for $x = 0.1$ [10, 51, 54]. Figure 6 shows an illustration of a KBNN supercell, in which an oxygen vacancy (denominated as $Ni - V_o - Nb$) has been included [54].

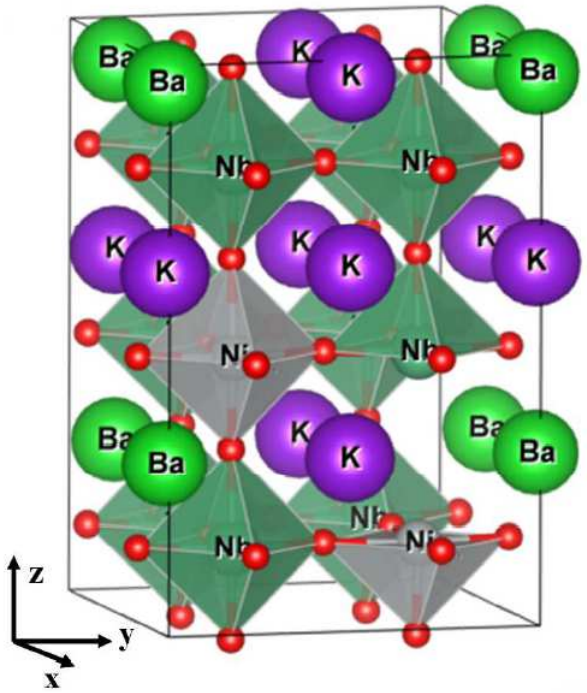

Figure 6 – Illustration a KBNN supercell, where the Ba, K, and oxygen ions are represented by green, purple and red spheres, and $Nb-O_6$ and $Ni-O_6$ are shown as green and gray octahedral, respectively. The oxygen vacancy is identified by $Ni-V_o-Nb$. Source: [54].

The remanent polarization value for the KBNNO system have been reported between 0.1 - 0.3 C/m^2 [10, 45, 51, 55]. When compared to other ferroelectrics, these polarization values reported for KBNNO are considered relatively low due to be limited by ferroelectric in sintered pellets. In spite of these values be low, it allows open-circuit voltages (V_{oc}) higher than the bandgap values observed of these materials, which is important to photo-carrier separation and photo-current across the bulk [10, 55]. Thus, the photovoltaic effect in ferroelectrics occurs in a different way to the conventional semiconductors p-n junction [54, 55]. Therefore, this type of ferroelectric perovskite could show a strong piezoelectric and/or pyroelectric response together with a considerable photovoltaic effect. Therefore, this characteristic opens the possibility for the creation of new multisource energy harvesters, or more useful multifunctional sensors, based on a single material, potentially leading to efficiencies that exceed those possible for traditional p-n junction cells [51, 54, 55].

However, from the application point of view, photovoltaic efficiency has been limited by the wide bandgaps values (2.7–4 eV) typical observed in ferroelectric oxides, which are capable of absorbing only 8–20 percent of the solar spectrum [10, 56]. This is undesirable for solar cells, where the optimum gap is about 1 eV, because it is well known that in

order to semiconductors absorb the visible light and ultraviolet ($<$ 700 nm wavelength) the E_g needs to be $>$ 1.77 eV than the photon energy [55, 57, 58]. Therefore, the fundamental challenge of the scientific community has been devoted to the decrease in the bandgap of ferroelectrics but remaining the ferroelectricity phenomenon, thus allowing higher solar light absorption and potentially better photovoltaic conversion efficiency to bring significant scientific and technological breakthroughs. Taking that into consideration, semiconductor materials are characterized by a full valence band and an empty conduction band at $T = 0K$, both separated by an energy gap of the order of $1 - 2$ eV, called the bandgap. Due to this small bandgap, the number of electrons in the conduction band is considerably high at room temperature, but it is smaller than the free electrons in metals (conductors), resulting in an intermediate conductivity between insulating and conductor materials. A completely full band does not contribute to a current flow as there is no free space for the particles to move around. If the conduction band is empty at a temperature around $0K$, the semiconductor material behaves like an insulating material. However, with a thermal excitation (at temperatures close to room temperature, for instance), the valence-shell electrons have enough energy to transfer from the valence band to the conduction band and become free electrons which lead to an observable conductivity [8, 59, 60]. A representation of the valence and conduction bands and the bandgap is represented in figure 7 for the KBNN system.

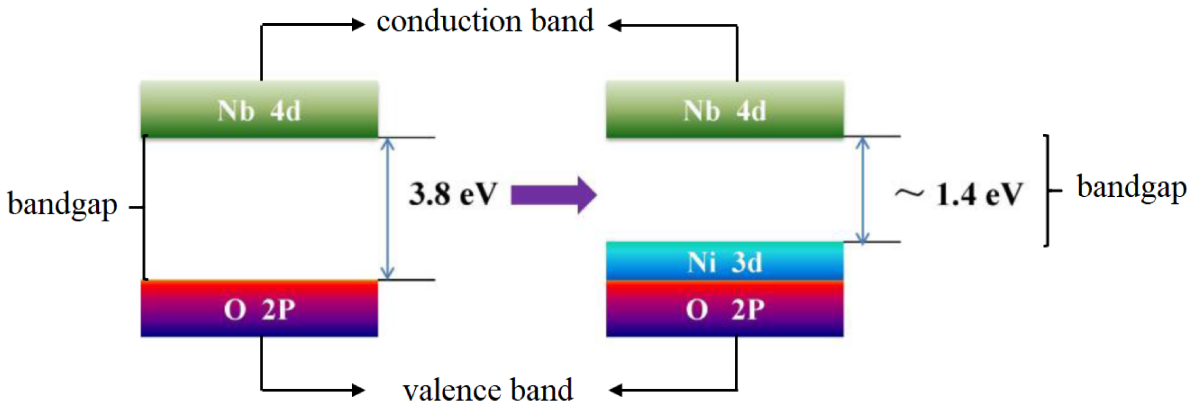

Figure 7 – The band diagram of the $KNbO_3$ (left) and one of the KBNN systems (right). Source: adapted from [8].

Therefore, the wide bandgap of the ferroelectric perovskites (ABO_3) is due to the characteristics of the A–O and B–O bonds, such as the large difference in electronegativity between the transition-metals and the oxygen ions. The excitation through the bandgap is caused by the transfer of charge from the oxygen (O) 2p-states at the valence band top to the transition-metal d-states at the conduction band bottom. For the $KNbO_3$,

the O 2p-states compose the valence band top, while Nb 4d-orbitals form the conduction band bottom, giving rise to a bandgap as high as 3.8 eV (figure 7). In the KBNN system, whose Ni element is introduced, the valence band top becomes the hybridized Ni 3d- and O 2p-states, while the conduction band bottom possesses the Nb 4d-states. Thus, the filled Ni 3d gap states lead to a greatly reduced bandgap of the KBNN material [10,61].

1.2.1 Applications

Ferroelectric materials are extensively used in a large range of applications, such as dielectric capacitors, mechanical and thermal sensors, actuators, transducers and energy harvesters [62–66], which have facilitated and brought innovation for the daily society. Initially, photo-ferroelectrics have been intended to be used as photovoltaic materials in solar cells [49,67,68], photodiodes [65] and optical readers of ferroelectric random-access memories [69]. Recently, however, these ferroelectric with semiconductor characteristics have attracted the scientific community as candidate materials with promising applications in photovoltaic and other multifunctional devices [65,70,71].

In terms of the photovoltaic (PV) application, photoferroelectrics such as KBNN have been revealed an interesting alternative to conventional semiconductor p-n junctions, because they exhibit bulk photovoltaic effect (BPVE) which allows an open-circuit voltage higher than the bandgap, because of their non-centrosymmetric microstructure that promotes the desired photo-excited carrier separation due to the intrinsic polarization. The PV effect is mainly characterized by two parameters: short-circuit current (I_{sc}) or photocurrent, and open-circuit voltage (V_{oc}). In bulk ferroelectric PV effect, the remnant polarization and the polarization-induced internal electric field exist over the whole bulk region of the material, and is due to this internal electric field that the photogenerated electron-hole pairs are separated. Therefore, the V_{oc} is not limited by the energy barrier (energy bandgap) of the material [50,72,73].

In the next section, will be presented the experimental procedure where the synthesis process and characterization techniques of the studied materials will be described.

2 EXPERIMENTAL PROCEDURE

Advanced materials commonly used in electronic, magnetic and optical devices are high-technology based systems whose properties and applications depend on the control of a lot of variables such as structure, precursors, dopants, crystallinity, particle size distribution, defects, and others [74,75]. Therefore, in order to optimize the desired property of such materials, several synthesis methods have been proposed, which include chemical, physical and biological methods. However, in most of the cases (as for example in the physical and biological ones), due to the high-cost to produce high quality materials (ceramics and thin films), the use of these techniques is not technologically (or economically) feasible [76]. Thus, the chemical methods have been probably the most used in the materials science and technology areas, and they can be divided into two categories: *i*- oxide precursors and *ii*- wet-chemistry methods. Table 1 summarizes the main and most commonly used techniques for the synthesis of materials, together with their respective category [77]. Because of the simplicity of solid-state reaction (SSR), this method is the most used one by the scientific community, and will also be employed in this work for obtaining the samples under study.

Table 1 – Main preparation techniques for solid materials (ceramics and thin films).

Precursor Oxides	**Wet Chemical**
Solid-state reaction	Sol-gel
	Pechini
Mechanical activation	Hydrothermal
Rapid liquid sintering	Co-Precipitation
	Combustion

The difference between the listed methods in table 1 is that the starting precursors in the solid-state reaction method are in powder form (commonly composed by oxides or carbonates) and are carefully mixed and milled before heat treatments. On the other hand, the precursor components in the wet chemical processes are mixed with nitric (or citric) acid in order to form a homogeneous solution, which is then dried before the heat treatments [77]. For a faster sample's preparation procedure, the sol-gel process is more appropriated than the solid-state method, which in fact takes up to several days for the sample to get ready. However, the complex procedure for the samples' production through the sol-gel method makes this process more difficult for the optimization of the involved synthesis parameters. Therefore, although the conventional solid-state reaction method

requires a higher energy consumption (during calcination and sintering), that is to say, it needs very high temperatures to allow the interdiffusion of the cations, this technique reveals to be simplest, relatively inexpensive, and it leads to the formation of highly dense ceramics [77]. In this context, in order to better understand the used method for the samples' preparation in this work, the state-solid reaction [1] will be described in details as follows:

- Solid State Reaction

It is well-known that an extensive group of ferroelectric systems that are commercially used are those obtained in the form of polycrystalline ceramics, for which the conventional solid-state reaction method is widely used. Table 2 summarizes the main steps involved in the SSR method, and are better describes as follows:

Table 2 – Conventional solid-state reaction method steps.

SSR method steps
Mixing
Milling
Calcination
Grinding
Pressing
Sintering

- **Mixing the powders:** For this process, it's necessary to know the precursor' reagents that need to be used, before proceeding with the stoichiometric calculations. Usually, and it's the case of the present work, oxides or carbonates compounds are used, where high purity reagents ($\approx 99,9\%$) are essential to avoid unwanted impurities or the formation of secondary phases and to obtain a good quality material with good reproducibility [78]. It's important to take into account that the reaction needs a high degree of solid-state reactivity. Some intrinsic characteristics of the materials can affect the kinetics of solid-state reactions such as particle sizes, crystal lattice irregularities, specific surface areas, crystallinities, and point defects.

[1] The state-solid reaction described forward follows the form that was used in this work, but it is important to mention that there are other forms to perform and different characteristics that can be used too. This manner is not as a rule.

Therefore, in order to improve the reaction efficiency during synthesis, these parameters need to be controlled to reduce the reaction temperature and to accelerate the sintering rate [78, 79].

- **Milling:** This process promotes the homogenization of the powders with a further decrease of particles size, which occurs by compression, impact, and friction between the contact of the balls with the particles [75, 80]. The milling of the power can be performed either manually, using an agate mortar and a pistil, or by using a ball-mill, which usually allows a considerable reduction in the milling time. The ball-mill, whose action is presented in figure 8, consists in a cylindrical object containing small balls, commonly made of alumina, zirconium or yttria-stabilised zirconia (YSZ), because the contamination range of the powders is smaller than other compositions. A milling fluid (acetone, isopropyl alcohol or deionized water) is added together with the oxide precursor powders in order to promote the breakup of agglomerates. The action of the mixing agents inside of the cylindrical container, in which the desired motion is that the balls fall onto the particles and not onto the mill bottom itself, is based on a cascade formation and creating both shearing and crushing actions on the powder. Normally, the grinding time is about a few hours. After the grinding process, the mixing is placed in an oven for drying [75, 78, 80, 81].

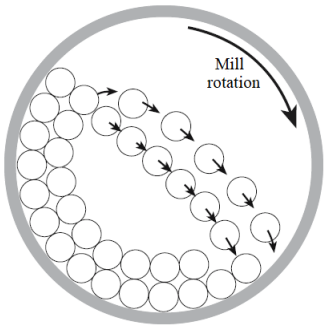

Figure 8 – Illustration of the cross section of a ball mill with components in motion. Source: [80].

- **Calcination:** In this stage, the desired crystallographic phase is commonly obtained through the chemical reaction of the constituent elements under high temperatures (above 600°C) conditions. For the calcination process to occur, the dried powders are placed into a carefully sealed high-purity alumina (or zirconia) crucible in order to avoid vaporization of some volatile elements and then placed in an oven. The material is heated at a temperature high enough to allow interdiffusion between cations and decompose any non-oxide precursors; in this way, the solid-state reaction between precursor powders is activated [78].

The chemical reaction occurs by solid-state diffusion of the ions and starts at the contact surfaces between the powders, where layers that increase with the reaction time by ionic interdiffusion are formed [77]. The initial kinetic of the reaction rate is very fast because of short diffusion paths, but as the particle sizes of the components increase the reaction rate decreases [75, 79]. Therefore, successive reactions at the interfaces of the reactant particles and the formed layers occur, and the interfaces move to the non-reacted particles until the powders were entirely reacted (figure 9). Some factors, such as types and concentrations of ions in the crystal lattice, temperature, vacancy concentration, mixing homogeneity, and others, can affect the diffusion process [75, 79, 82].

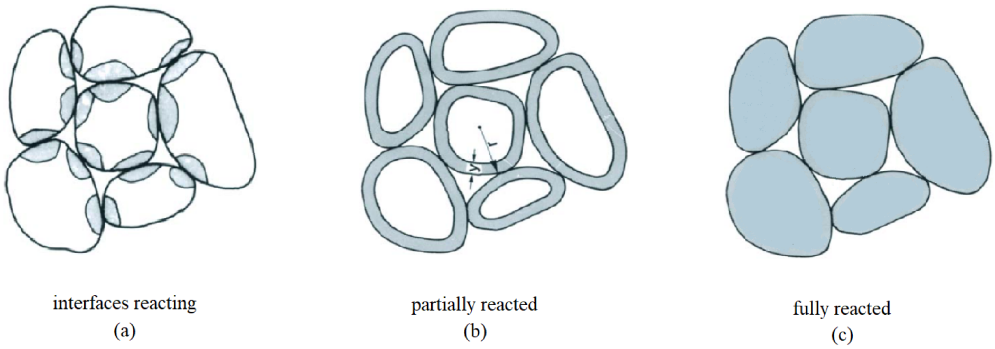

Figure 9 – Schematic representation of the solid-state reaction in mixed powders. (a) Reaction starts to occur at the interfaces of powders, (b) layers forming and partially reacted, and (c) particles fully reacted. Source: adapted from [75, 82, 83].

- **Grinding:** Following, the grinding process is performed and the calcinated powders are submitted to a similar crushing step to that previously done. The aim of this step is to break up hard agglomerates that could have been formed and reduce even more the particle size [78].
- **Pressing:** In this step, ceramic bodies are commonly obtained by pressing the calcined powders, thus forming ceramic pellets in different shapes (cylindrical, square or rectangular), which are named as "green" samples. It is important to point out that, for the samples to be pressed, few manual mills require additional cares, where organic binders and dispersants can be added to aid densification of the pastilles and prevent the flocculating of the powders, respectively, for forming ceramic bodies [78].

The powders can be pressed into two different pressing processes: *i*- uniaxial pressing, whose apparatus constitutes of a steel punch and a die-set that will form cylindrical, square or rectangular ceramics. In this process, it is important to ensure that the force is equally applied in the vertical direction, on both opposite (top and bottom) samples' faces; *ii*- isostatic pressing, which involves a hydrostatic pressure that promotes a uniform

distribution of the pressure (applied in all spatial directions) on the samples. In this case, the samples are placed in a vacuum-sealed rubber (or latex material) and then submerged inside an oil fluid-filled recipient. Finally, the samples are subjected to a high pressure condition. The applied pressure to the fluid is equally transmitted in all directions and acts over the internal parts of the ceramic body, thus ensuring a uniform pressing and breaking up internal agglomerates (air spaces) in order to produce dense green ceramics [75, 78].

- **Sintering:** The last stage of the solid-state reaction method is the sintering process, which is made for the samples' densification, and is usually performed in very high temperatures conditions (above 1000 °C). In this process, grain formation is achieved, allowing highly dense ceramics and undesired secondary phases, which could have been formed during calcination, are eliminated. Since the grain-size is known to command most of the physical properties of the material, it is important to control this parameter, which can be carried out by the optimization of both sintering temperature and time parameters [79, 83].

Some intrinsic (i.e., particle packing homogeneity, etc) and extrinsic (i.e., external pressures, etc) factors can affect the sintering of the samples [79, 83]. During sintering, for instance, the "green" bodies are heated into very high temperatures (closely about the melting point of the ceramic, in most of the cases), depending on the ceramic system. It is known that the heating rate strongly influences the final result. Therefore, this process has to be carefully controlled. Very high heating rates promotes highly porous samples, and even cracked ceramics, because most of the organic compound could not have been burned off [78, 83]. As the temperature increases, the pores between particles formed during pressing in the ceramic green bodies on pressing are filled by the own green pellets' material, thus forming the grains. Figure 10 illustrates how the densification and grain growth occur in the sample during sintering, suffering the sample significative changes. The particles and pores morphology (size and shape) change by the ions transfers of atoms and ions to reduce the total surface energies. The pores can be located at the inner part of a grain (bulk) and also at the grain boundaries (between adjacent grains). The reductions in porosity and particle surfaces lead to an increase in the density (densification) of the ceramics [79, 83].

In general, the sintering process occurs in three stages: initial, intermediate, and final stage. At the initial-stage sintering, the distance between particles shrinks by diffusion mechanisms and homogenization of segregated material, rounding the pores and forming grain boundaries. In addition, the neck formation and growth (contact areas between adjacent particles) show to occur, leading to a decrease in the porosity. In the intermediate stage, the intersection of grain boundaries takes place and the necks start to grow, thus promoting a slow grain growth. The porosity also decreases substantially leading to a

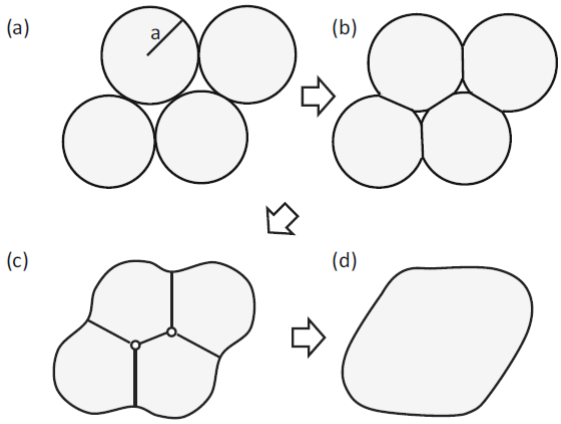

Figure 10 – Steps of the grain formation during sintering. (a) Particle packing, (b) formation of necks between the particles, (c) neck growth and shrinkage of pores, and (d) formed grain. Source: adapted from [79].

reduction in the open pores (or incorporating into large pores) and increasing the density of the ceramics. At the final sintering stage, some pores are closed and other pores decreases to a limiting size or disappear, the grains grow, and the desired final relative density of the ceramics becomes above 90% [75, 79, 82, 83].

Finishing the state-solid reaction method, the obtained samples are polished (over the opposite surfaces), in order to eliminate residual particles coming from the oven, as well as to guarantee flat and parallel opposite surfaces. Since most of the studied ferroelectric ceramics are used in electronic devices, such as capacitors, this poling procedure is essential for a good working of the final material properties [79, 81].

2.1 Synthesis and Samples Preparation

For the synthesis of the studied samples in the present work high-purity analytical grade reagents were used, as shown in Table 3, in which the chemical formulas, brands and purities, of the used compound are also presented.

$KNbO_3$-based lead-free ceramics were prepared with an intention to generate oxygen vacancies. For that, starting from the nominal formula $(1-x)KNbO_3 - xBaNi_{1/2}Nb_{1/2}O_{3-\delta}$ (KBNN), different concentrations of oxygen vacancy defects were considered, namely, δ = 0.025 (KBNN01), 0.05 (KBNN02) and 0.15 (KBNN03), while the Ba/K ratio was kept unchanged to 0.10/0.90. The samples were identified according to the nomenclatures indicated in Table 4. Stoichiometric calculations were performed and a high precision analytical scale (SHIMADZU/AUW320) was used to weigh the needed quantities needed of the precursor reagents, considering their purities, to obtain the samples.

Table 3 – List of precursor reagents used for the samples' preparation.

Reagents	**Chemical formula**	**Brand**	**Purity**
Potassium Carbonate	K_2CO_3	Dynamics	98%
Niobium(V) Oxide	Nb_2O_5	Aldrich	99.9%
Barium Carbonate	$BaCO_3$	Vetec	99%
Nickel Oxide	NiO	Aldrich	99.8%

Table 4 – Chemical formulas of the studied compositions together with their respective nomenclatures.

Compositions	**Nomenclature**
$(K_{0.90}Ba_{0.10})(Nb_{0.95}Ni_{0.05})O_{3-0.025}$	KBNN01
$(K_{0.90}Ba_{0.10})(Nb_{0.95}Ni_{0.025})O_{3-0.05}$	KBNN02
$(K_{0.90}Ba_{0.10})(Nb_{0.90}Ni_{0.05})O_{3-0.15}$	KBNN03

Figure 11 shows a diagram illustrating all the steps used for the synthesis of the samples. After weighing, the powders were mixed and ball-milled sing alumina ball together with isopropyl alcohol for 4 hours for homogenization. The mixed samples were then placed in an oven for drying at 150 °C during 4 hours. The mixed powders were then subjected to the calcination process.

Figure 12 shows the heating rates used for the calcination of the samples. The powders were placed into an alumina crucible and sealed with alumina powder to avoid potassium volatilization and, then, placed in an oven (MTI/KSL-1500X). The initial heating rate of 2 °C/min from room temperature up to until 75 °C ware carried out in order to eliminate additional residual solvent used during the milling process. A second heating rate of 5 °C/min was used from 75 °C up to 850 °C for the final calcination, remaining the samples at the maximum temperature over 2 hours, in order to promote the desired phase formation. The temperature was then returned back to room temperature with a cooling rate of 10 °C/min. The calcined powders were ball-milled again for 2 hours with isopropyl alcohol and placed in an oven for drying at 150 °C during 4 hours. Then, in order to verify the formation of the ferroelectric structural phase, a complementary X-ray diffraction measurement was performed.

In order to produce the pellets, the calcined powders were then mixed in an agate

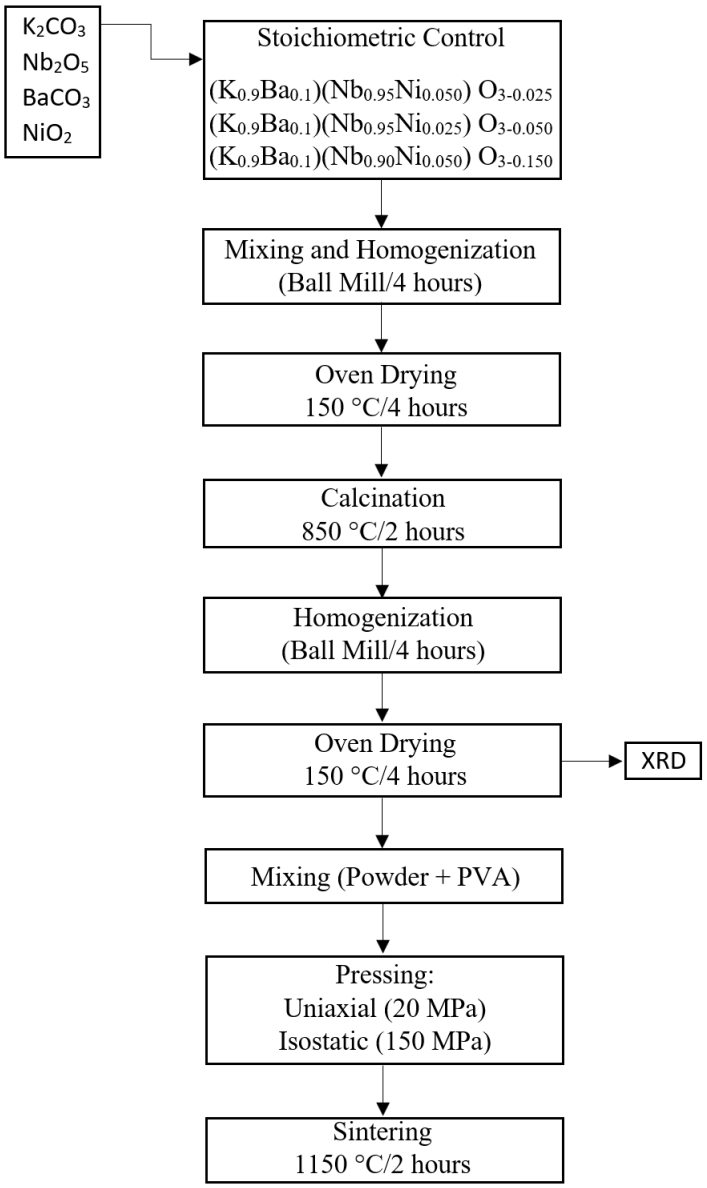

Figure 11 – Flowchart regarding the steps to obtain the samples used in this work.

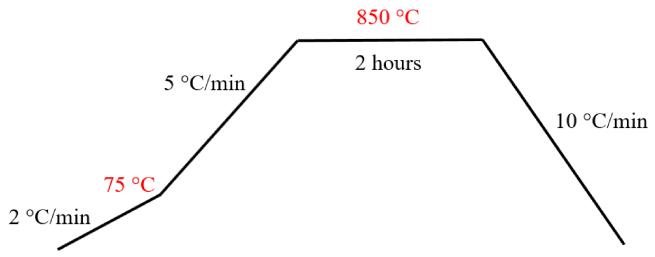

Figure 12 – Calcination diagram showing the thermal treatments steps.

mortar using polyvinyl alcohol (PVA) as a binding agent, in order to facilitate the powders compaction during pressing. The samples were then subjected to a first pressing process,

using a uniaxial press (MacFort/3 Ton) at 20 MPa during 7 minutes, obtaining disk-shaped samples. Then, the disks were previously uniaxially pressed tablets were placed in a flexible latex mold inside a camera with a viscous hydraulic fluid to ensure that the pressure is applied equally in all directions on the material faces. The samples were isostatic pressed (MTI/CIP-15) at 150 MPa during 15 minutes.

For the sintering of the samples, the cylindrical bodies were again placed inside sealed alumina crucibles, using the same oven (MTI/KSL-1500X) and air atmosphere. Similar condition rates to that for the calcination were now used for sintering, but with different maximum temperature (1150 °C during 2 hours). After sintering, all the obtained KBNN compositions were polished for further characterizations. In order to estimate the samples' density, the Archimede's method has been used, for which a hydrostatic support was coupled to the analytical scale (SHIMADZU/AUW320), and the equation 2.1 was used to obtain the apparent density (ρ_{ap}). The parameters m_a and m_l represents the masses of sample in air and in water, respectively, while ρ_l represents the liquid's density (water).

$$\rho_{ap} = \frac{m_a}{(m_a - m_l)}\rho_l \tag{2.1}$$

The final relative density (ρ_r) was estimated from the equation 2.2, after comparing the apparent density with the previously calculated theoretical density (ρ_t).

$$\rho_r = \frac{\rho_{ap}}{\rho_t} \times 100\% \tag{2.2}$$

In the next section will be presented and discussed the experimental techniques that were used in this work.

2.2 Experimental Techniques

In order to observe and understand the structural, microstructural, electrical and optical properties of the studied ceramics, some characterizations are essentials for these analyses. Therefore, for a better understanding, a brief approach to each technique and method used in this work will be described. They are: X-ray diffraction (XRD), Rietveld Refinement, Williamson-Hall Method, Raman Spectroscopy, Scanning Electron Microscopy (SEM), Impedance Spectroscopy, Dielectric Spectroscopy and Integrating Sphere Method.

2.2.1 X-Rays Diffraction

One of the main characterizations used for the study of the structural properties of materials is the X-ray diffraction technique. Through of the diffraction patterns characteristics, this technique is able to provide essential information, such as crystalline structure, formed phases, among others [84]. Figure 13 presents a schematic diagram with a summary of the structural parameters that can be known and calculated, by other methods, through of a powder diffractogram components. Moreover, the background also provides information about the sample's crystallinity [84, 85].

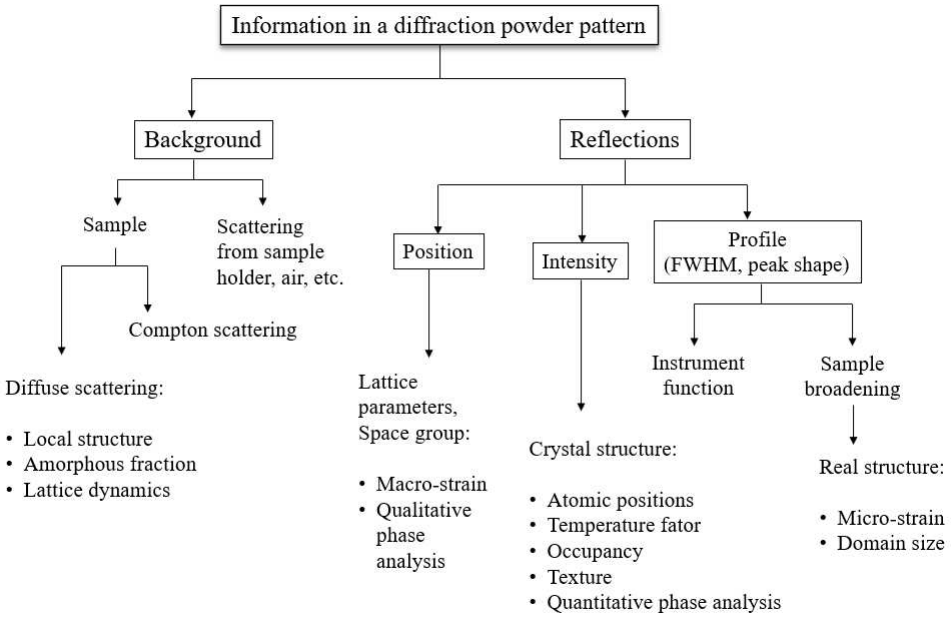

Figure 13 – General parameters that can be withdrawn as information of the items that constitute a typical powder diffraction pattern. Source: adapted from [84].

In few words, the X-rays are produced through a tube where electrons are accelerated by a high voltage source and collide with a metallic target, thus, emitting the X-rays [84, 86] [2]. For the diffraction phenomenon to occur in a crystal, the interatomic spaces need to be in the same order of magnitude as the characteristic wavelength of the incident radiation, i.e., Angstrom order (10^{-10} m or Å). Furthermore, since the atoms are periodically arranged on a lattice, the incidence of the X-rays upon the atoms causes a radiation scattering in all directions, which there are phase relations between the scattered waves. If they are not in phase, which occurs in most directions of scattering, there will be not diffraction and is named as destructive interference. On the other hand, if the waves are completely in phase, i. e., the difference in optical path lengths is zero (or an integer multiple of wavelength), the diffraction pattern of the material will be produced [84, 86, 87].

[2] For knowing more about the X-rays production and more information, see Ref. [86], chapter 1.

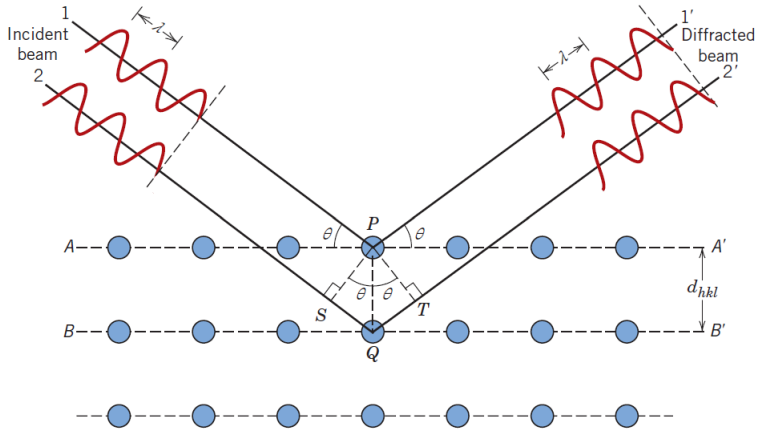

Figure 14 – Illustration of the Bragg's Law through of the diffraction of X-rays beams phenomenon on crystalline plans of a crystal. Source: [88].

For the study of the XRD, the Bragg's Law is the most important and familiar method used and, by the Figure 14, it is possible to understand how it works. Let a crystalline structure be with atoms arranged in an organized and periodic manner on a lattice, and suppose two parallel atomic plans AA' and BB', whose the h, k, l Miller' indexes (h,k,l) are the same and are separated by the interplanar distance d_{hkl}. When focusing a parallel, monochromatic, and in-phase X-rays beam on these two planes at a θ angle, two rays (labeled as 1 and 2) are scattered by atoms the P and Q atoms. As previously stated, if the difference of optical paths, i.e., 1-P-1' and 2-Q-2' (or $\overline{SQ} + \overline{QT}$), is equal to an integer number (n) of the wavelength, a constructive interference will be produced at a θ angle with respect to the planes.

Then, algebraically, for the diffraction occurs, the condition is the following [88]:

$$n\lambda = \overline{SQ} + \overline{QT} \tag{2.3}$$

Using the sine rule in a triangle in the equation 2.3:

$$n\lambda = d_{hkl}\sin\theta + d_{hkl}\sin\theta \tag{2.4}$$

Therefore,

$$n\lambda = 2d_{hkl}\sin\theta \tag{2.5}$$

The equation 2.5 is known as the Bragg's Law and for the diffraction to be detected it must be satisfied; the n parameter is an integer number (0,1,2,3...) and represents the order of reflection, which is the wavenumber for which the interference is constructive (0,1,2,3...), λ is the incident electromagnetic radiation wavelength, d_{hkl} is the distance between the adjacent planes, and θ represents the angle formed by the incident beam and the surface of the reflected planes [88].

In this work, the structural characterization of the samples was performed at Multi-user Laboratory of the Institute of Chemistry, of the Federal University of Uberlândia, using a SHIMADZU X-ray diffractometer (XDR-6000 model) with KαCu radiation and wavelength $\lambda = 1.5406$ Å. For both calcined and sintered powdered samples, the parameters used in the measurements were: interval of 2θ between 10° and 130°, the reading step being of 0,02° at a speed of 0,02°/min in continuous scan mode, whose purpose is to form and determine the presence of the desired phase of the analyzed compound. The ferroelectric phases presented were identified, subsequently, with the help of the database available on the CAPES Research Portal. Through the data obtained from the XRD measurement, many information can be calculated as will be shown forward.

2.2.2 Rietveld Refinement

As mentioned in the preview section, X-ray powder diffractograms contain structural information of the studied material that are necessary to analyze these data. Most current methods for powder diffraction data analysis includes a pattern modeling stage, because of the intrinsic nature of diffraction and one of the most used techniques for treating powder diffraction data is the Rietveld refinement method [89]. This method consists of a standard theoretical treatment of the diffraction data collected experimentally to make a final structural model and to determine the crystal structure by refining relevant parameters of individual atoms together with profile variables [84,85,90,91].

The Rietveld method [3] uses a mathematic model based on the least-squares theory to perform the refinement of the structure. These refinements are accomplished until obtaining the best fit between the observed powder diffraction pattern (experimental) and the calculated pattern (theoretical) based on the simultaneously refined models for the crystal structure(s), lattice parameters, diffraction optics effects, instrumental factors, and other desired characteristics of the samples [84,85,90,91].

A minimization by least-squares is used when the number of observations (in this case, powder profile points) is greater than the number of parameters, and will give estimated parameter of minimum variance in any linear combination, i. e., estimates the values of the adjustable parameters in a model. Then, using this principle to an approximation

[3] There are examples of Rietveld refinement of some materials in Ref. [85], chapter 7.

between the calculated and observed patterns, the minimized function is the residual and given by:

$$\Phi = \sum_{i=1}^{n} \omega_i (Y_i^{obs} - Y_i^{calc})^2 \tag{2.6}$$

where $\omega_i = [Y_i^{obs}]^{-1}$ (for a standard x-ray powder diffraction pattern); Y_i^{obs} and Y_i^{calc} are the observed and calculated intensity at the ith step, respectively, and the sum is over all points (n) of the diffraction pattern data [85].

A diffraction pattern of a crystalline material can be simulated from a structural model, where the calculated intensities, y_i^{cal}, is proportional to the square of the absolute value of the structure factor (i.e. $|F_K|^2$), plus the background [91]. Then, the equation that provides the intensity profile for each step (i) is of the type:

$$Y_i^{cal} = s \sum_K L_K |F_K|^2 \phi(2\theta_i - 2\theta_K) P_K A + Y_i^{bkg} \tag{2.7}$$

where:

s = is the scale factor;
K = represents the Miller indices, h k l, for a Bragg reflection;
L_K = contains the Lorentz, polarization and multiplicity factors;
ϕ = is the reflection profile function;
P_K = is the preferred orientation function;
A = is an absorption factor;
F_K = is the structure factor for the Kth Bragg reflection;
Y_i^{bkg} = is the background intensity at the ith step.

Through of the lattice parameters, spatial group and the Bragg's Law, the position for each reflection of the diffraction pattern can be obtained. Initially, the technique starts with approximated values of a set of free variables of the initial appropriated model that will be adjusted and, slowly, refined together with others additional parameters by the least-squares method. This refinement follows until all model parameters are adjusted to obtain the best fit. To accomplish good results of a refinement, firstly, in addition to a well quality of the experimental data of the diffraction pattern, is also necessary to know the software that will be used as well as information about the correct sequence of the parameters to be refined. Therefore, to know the successfulness of each refinement cycle, there are some indicators for this judgment, and the main are: R_p (profile R-factor),

R_{wp} (weighted profile R-factor), and χ^2 (mean squared deviation) [4]. They are commonly known as 'goodness-of-fit' parameters and are given by the following equations:

$$R_p = \frac{\sum_{i=1}^{n} \mid Y_i^{obs} - Y_i^{calc} \mid}{\sum_{i=1}^{n} Y_i^{obs}} \times 100\% \tag{2.8}$$

$$R_{wp} = \left[\frac{\sum_{i=1}^{n} \omega_i (Y_i^{obs} - Y_i^{calc})^2}{\sum_{i=1}^{n} \omega_i (Y_i^{obs})^2} \right]^{\frac{1}{2}} \times 100\% \tag{2.9}$$

$$\chi^2 = \frac{\sum_{i=1}^{n} \omega_i (Y_i^{obs} - Y_i^{calc})^2}{n - p} \tag{2.10}$$

where, n is the total number of measured points in the diffraction pattern, and p is the number of free least squares parameters, i. e., refined. If the refinement was done properly, then the value of reduced χ^2 will be somewhat greater than unity for an optimal refinement. On the other hand, if this value turns out to be significantly less than unity, then something was done wrong in the refinement procedure [5]. In some cases, might be necessary to proceed with many refinement cycles in order to obtain the best fit [85, 91]. Thus, following are described the main parameters that are simultaneously refined by Rietveld methods:

- *Background*: provides information about the crystallinity (i. e., amorphous phase and phase quantification) of the material. The data of the pattern need to be collected with the best possible resolution over a minimum background to obtain a highly precise diffraction pattern and it should never be subtracted prior to full pattern decomposition on Rietveld refinement. The background is approximated and corrected using various polynomial functions with coefficients and data of the diffractogram, which are refined along with other parameters. Thus, the calculated background is added to the intensity calculated as a function of the Bragg's angle.

- *Scale Factor*: corresponds to a proportionality multiplier that normalizes experimentally observed integrated intensities with calculated intensities. It is determined by number, spatial distribution, and states of the atoms in the unit cell. The refinement of this parameter is directly related to the quantitative phase analysis of the present phases.

[4] The normalised χ^2 function is the ratio of weighted profile to expected profile R-factors and is a good measure of how well the data are fitted. $R_{wp(exp)} = \frac{R_{wp}}{\sqrt{\chi^2}}$

[5] Remembering that also is important to observe the results of the other factors for a good refinement, and not only the χ^2.

- *Peak Shapes*: the shape of each Bragg peak is formed by the convolution of instrumental and sample functions, and can be modeled and corrected using functions like Gaussian, Lorentzian, Pseudo-Voigt and Pearson-VII, which are the most used, together with the function that corrects the asymmetry. The broadening of the peaks is associated with the crystallite (coherent domain) size and deformation of the unit-cell (microstrain) contributions.

- *Displacement*: is one of the errors that can be present in the measured Bragg angles, beyond the zero-shift and transparency effects. It can occur due to an incorrect positioning of the sample from the goniometer axis. The refinement of this parameter corrects the displacements of the diffraction maxima, and can be refined together with the lattice parameters.

- *Lattice Parameters*: the Bragg's peak positions are related to the lattice parameters, which are the unit-cell dimensions. Therefore, the Bragg's Law is used to correct these parameters. Knowing lattice parameters is essential to identify the correct crystal structure of the material.

- *Structure Factor*: (or the structure amplitude) is composed by details of the crystal structure that will be refined, i. e., coordinates and types of atoms, their distributions among different lattice sites (in the unit-cells), and site occupation number. The refinement of this parameter also analyses the different scattering abilities of the atoms.

- *Temperature Factors*: (or atomic displacement factor) describes the thermal motion of the atoms relative to their equilibrium position. Includes displacement parameters (isotropic and anisotropic approximation), deformation of the electron density around the atom due to chemical bonding, preferred orientation, improperly or unaccounted effects as absorption and porosity. These factors modify the diffracted intensity as a function of the Bragg angle.

- *Preferred Orientation*: it occurs when the crystallites of the sample don't have a random orientation, i. e., have a natural inclination to align in a particular crystallographic direction. Problems in the sample preparation generate this analysis, and it may cause considerable distortions in the intensity of the scattered beams.

The Rietveld refinement is made through of powerful computational programs, where the General Structure Analysis System (GSAS) and Fullprof are the two software most common used, the latter being the program used in the study of this work for data analysis.

2.2.3 Williamson-Hall Method

It is known that a perfect crystal doesn't exist due to its finite size, i. e., all the materials have defects in their structures[6]. These induced deformations on lattice and together with instrumental factors affect directly the broadening of the diffraction peaks, where the later has a smallest contribution. Therefore, the higher the number of defects in the crystalline structure, the greater the width of the peaks, and consequently, the material will have a greater microstrain. From these information, it is possible to determine the crystallite sizes (or coherent domain) and the lattice microstrains [84,86].

In 1918, Paul Scherrer discovered a relation that estimates a mean crystallite size from the X-rays diffraction pattern data. However, this method has a limitation, because it considers that the peak width is due only to the contribution of the crystallite size of the sample, and does not include the effects related to the lattice microstrains [86]. Scherrer's method is given by [84]:

$$D = \frac{K\lambda}{\beta_D \cos\theta_\beta} \tag{2.11}$$

where D represents the mean crystallite size (in nanometers, nm); K is the proportionality Scherrer's constant and it is related with the particle geometry; λ is the X-rays wavelength used (usually, CuK_α); β_D is the broadening of the diffraction line measured at the full-width at half maximum (FWHM) of the peak; and θ_β is the Bragg's angle of the peak related to plane with the respective Miller's indexes for a given diffraction. Usually, for a better approximation, it is assumed that the crystallites have spherical symmetry, whose particle geometry value is used as $K = 0,89$ [86].

As stated earlier, the Bragg's peak width is given by a combination of the sample and instrument effects, because errors can emerge if the equipment is not properly calibrated. Therefore, it is very important to introduce a correction in the peak broadening with the instrumental broadening contribution. In this context, the corrected FWHM is given by the following equation:

$$\beta_D = \sqrt{\beta_{exp}^2 - \beta_{inst}^2} \tag{2.12}$$

where β_{exp} and β_{inst} are the full-width at half maximum of the experimental diffraction

[6] These imperfections can identify as punctual defects (vacancies, interstitial sites, and impurities), linear defects (a dislocation one-dimensional around which some of the atoms are misaligned in a defined direction), and planar or interfacial defects (external surfaces, grain boundaries, phase boundaries, twin boundaries, and stacking faults). In addition, there are more defects descendant of processing and fabrication steps that include pores, cracks, among others [88].

peaks of the analyzed material and the full-width at half maximum of the instrumental diffraction peaks of a standard sample used as the reference material (NITS pattern) [92]. The standard material employed was the silicon (Si), which has a value of 0,001 for the equipment used in this work.

In 1953, Williamson and Hall made a correction to the Scherrer's model and proposed a method in which assumes that both crystallite size and induced lattice microstrain are additive and contribute to the diffraction peak broadening. Thus, the Williamson-Hall (W-H) method assumes that the convolution of these effects is a sum of the coherent domain size (β_D) and strain (β_η) contributions. Therefore, the total peak width is obtained by the following equation [93]:

$$\beta_{hkl} = \beta_D + \beta_\eta \tag{2.13}$$

$$\beta_{hkl} = \frac{K\lambda}{D\cos\theta_\beta} + 4\eta\tan\theta_\beta \tag{2.14}$$

Rearranging equation 2.13 gives:

$$\beta_{hkl}\cos\theta_\beta = \frac{K\lambda}{D} + 4\eta\sin\theta_\beta \tag{2.15}$$

Equation 2.15 is known as Williamson-Hall equation [7], where θ_β is Bragg angle referring to Miller's indexes (hkl); and η is the lattice microstrain. From this equation, the crystallite size and microstrain are determined through the linear fit of the extracted data of the graphic of β_{hkl} in function of $\sin\theta$ with the equation 2.15, where D and η are obtained by the linear and angular coefficients, respectively.

2.2.4 Raman Spectroscopy

Raman spectroscopy is a technique based on the inelastic scattering of light that was developed by Raman and Krishnan in 1928 [95]. The objective was to obtain quantitative and qualitative chemical information and morphological analysis of the object in study through of vibrational modes for the determination of the structure. This technique has been widely used over several decades in many scientific and industrial sectors, such as biochemical, medical, environmental and other applications [96].

When light is focused on the matter, there are two modes of interaction: the photons may be absorbed (or scattered), or yet may pass straight through the material and not

[7] There are other approaches about the Williamson-Hall equation that can be seen in Ref. [94].

interact with it. In Raman spectroscopy (RS), the sample is irradiated by laser beams of a single frequency (UV-visible region), and the scattered radiation with vibrational energy different from the incident beam is detected [96,97].

According to classical theory, the Raman effect can be explained as follow: Let the electric field strength (E) be of the laser beam (electromagnetic wave) that propagates with time (t) given by [96]:

$$E = E_0 \cos\{2\pi\nu_0 t\} \tag{2.16}$$

Where E_0 is the vibrational amplitude and ν_0 is the frequency of the laser. If the light interacts with the molecule, at this instant, the energy present in the light wave energy is transferred to the molecule, and an electric dipole moment P (equation 2.17) is induced; that is to say, the molecule polarizes distorting the electrons cloud around the nucleus and, thus, creates a kind of short-life "virtual state".

$$P = \alpha E = \alpha E_0 \cos\{2\pi\nu_0 t\} \tag{2.17}$$

The proportionality constant α is the polarizability. In the "virtual state", electrons are in a higher energy state, so that it results in a high energy form of the molecule with a different electron geometry to that found in the static molecule. Therefore, the nuclei need to adapt to the distorted electronic arrangement [8] with a new equilibrium geometry, but they do not have time for this and, consequently, the photon is quickly re-radiated as scattered radiation [96,97].

In vibrational spectroscopy, the detected energy changes are those required to cause nuclear motion. Thus, let ν_n be the vibrational frequency of the molecule, then the nuclear displacement (q) is given by:

$$q = q_0 \cos\{2\pi\nu_n t\} \tag{2.18}$$

where q_0 is the vibrational amplitude. For too small vibration amplitudes, α is a linear function of q. Therefore, it is possible to expand the polarizability in a Taylor's serie, according to the following equation:

[8] The shape of the distorted electron arrangement will depend on how much energy is transferred to the molecule, i. e., depends on the frequency of the laser used. Thus, the laser defines the energy of the virtual state and the extent of the distortion.

$$\alpha = \alpha_0 + \left(\frac{\partial \alpha}{\partial q}\right)_0 q_0 + ... \tag{2.19}$$

Here, α_0 is the polarizability at the equilibrium position, and $(\partial\alpha \setminus \partial q)_0$ is the rate of variation of α with respect to q at the equilibrium position. For the Raman-active mode to occurs, it is necessary that the rate of change of polarizability with the vibration must be non-zero, i.e. $(\partial\alpha \setminus \partial q)_0 \neq 0$.

Thus, relating the equations 2.17, 2.18 and 2.19 the polarization could be expressed by:

$$P = \alpha_0 E_0 \cos\{2\pi\nu_0 t\} + \frac{\partial \alpha}{\partial q}_0 q_0 E_0 \cos\{2\pi\nu_0 t\} \cos\{2\pi\nu_n t\} \tag{2.20}$$

and using a trigonometric relation, it can be obtained:

$$P = \alpha_0 E_0 \cos\{2\pi\nu_0 t\} + \frac{1}{2}\left(\frac{\partial \alpha}{\partial q}\right)_0 q_0 E_0 [\cos\{2\pi(\nu_0 + \nu_n)t\} + \cos\{2\pi(\nu_0 - \nu_n)t\}] \tag{2.21}$$

By the classical theory, the first term of the equation 2.21 is related to the Rayleigh scattering, which represents the oscillation of a dipole emitting light with a ν_0 frequency. The second and third terms is related to the two types of Raman scattering denominated as Stokes and anti-Stokes, whose frequencies are $\nu_0 - \nu_n$ and $\nu_0 + \nu_n$, respectively [96]. Therefore, the light scattering is identified of two forms: *i*- by the elastic process, when the scattered beam has the same frequency as the incident beam (known as Rayleigh Scattering), and there is only an electron cloud distortion without a nuclear motion. This is the dominant effect; *ii*- by inelastic light scattering (called Raman Scattering), where the vibrational frequency (ν_n) is measured as a shift from the incident beam frequency (ν_0) and cm^{-1} is often used as a unit by Raman spectroscopists. The Raman effect occurs because of the nuclei motion at the same time when the light interacts with the electrons [80, 96, 97].

Figure 15 illustrates, through a simple diagram, the Rayleigh and Raman scatterings. At room temperature, most of the molecules are in the ground electronic state (where has the lowest energy vibrational levels). The first mechanism (left) shows the Rayleigh scattering, where the molecule is excited by the incident photon to a virtual energy state, but since it does not involve energy change, the photon is scattered with the same energy ($E_0 = h\nu_0$) than the incident energy, and the molecule returns to the ground state (ν_0).

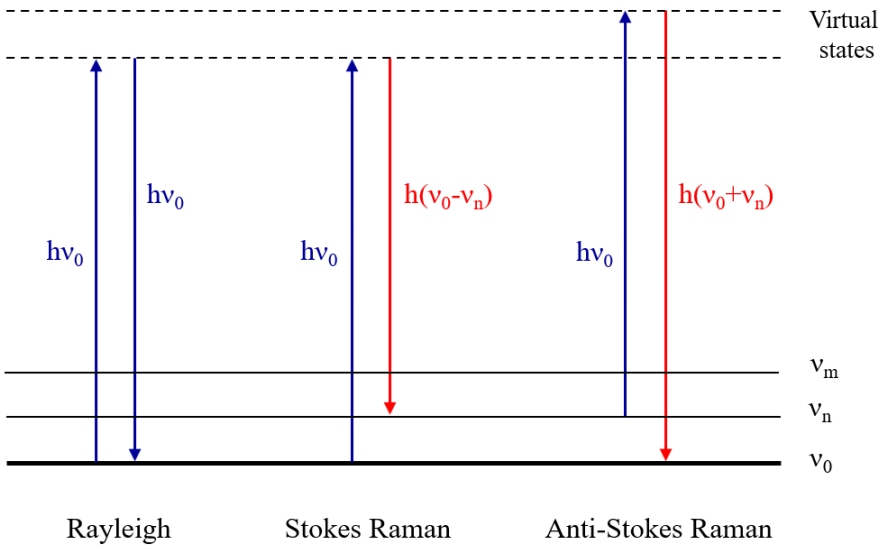

Figure 15 – Diagram of the transitions that occur in the Rayleigh and Raman scattering process. Source: based on [80].

The second effect (center) shows the Stokes scattering. Here, the molecule is in the ground state (ν_0) and absorbs the energy of the incident photon; therefore, when leaving the virtual state, it is promoted to a higher energy excited vibrational state (ν_n) causing a decrease in the frequency of the scattered light. In the third effect (Anti-Stokes), the molecule is already in a higher energy state (ν_n), due to thermal energy. Then, it transfers energy to the scattered photon decaying to the ground state (ν_0), which causes an increase in the frequency [80, 96, 97].

In crystalline systems, the Raman effect causes some different effects than in molecules. When the radiation interacts with the material, vibrations are produced and propagated through of the whole lattice. For instance, the oscillatory motions of each atom influence the motions of the neighbors' atoms, producing the lattice vibrations due to periodic arrange. These lattice vibrations are also known as phonons. If the displacement of the phonons is along the propagation direction of the wave, they are named as longitudinal waves (or L modes); but, if it is perpendicular to the propagation direction, then, they are known as transverse waves (or T modes). These modes will just occur if the phonons wavelength is long and in the same order of magnitude of the electromagnetic radiation (in the visible region: 5×10^3 Å). Therefore, they are called optical modes and can be represented as LO and TO, for longitudinal and transverse optical modes, respectively [9] [97, 98].

[9] The optical modes are of the higher energy type and there are some rules, named selection rules, that determine what phonons are Raman-active, which depend of the symmetry group of the material. Group Theory can help to understand more about it.

Raman spectroscopy provides a fingerprint of the materials, which allows obtaining its electronic and structural information, such as atomic and electronic structure, defects, charge transfers, among others. The Raman bandwidth varies depending on the material and the angular variation of the scattering gives information about the symmetry of the lattice vibration. The intensity of the bands (scattered radiation) depends in general on the directions of observation relative to the principal axes of the crystal [97]. In ferroelectric materials with perovskite structure, for instance, the phonons are related to the distortions of the crystal lattice caused by motions of the BO_6 octahedra around different crystallographic axes, which correspond to the rotational soft-modes ("pure rotations"), and the displacements of the A and B cations, which correspond to the polar soft-modes [99].

In this work, the Raman spectra were colleted by using a LabRam HR Evolution spectrometer using a 532×10^{-9} m excitation line from an Argon laser.

2.2.5 Scanning Electron Microscopy

The Scanning Electronic Microscopy (SEM) is a powerful technique used to characterize materials and surfaces, providing images at relatively high resolution that contain topographic and compositional information of both qualitative and quantitative nature. The working principle of the SEM consists, basically, in the focused electron beam emission [10] irradiating the sample's area to be analyzed that will be interacting and produce electrons and photons, which will be collected and converted to form the images [100].

The SEM is formed by basic components: the electron gun, lens system, electron collector, visual and recording cathode ray tubes (CRT's), and the electronics associated with them. In the electron gun, the electrons are obtained through the thermionic emission, in which a certain percentage of the electrons, in the cathode material, become sufficiently energetic to escape the source to the anode, because of the sufficiently high temperatures involved in the process [11]. The electron beam travels down the optical axis formed by electromagnetic lenses that control the angular spread and desmagnify the beam, and determine the final spot size of the electron beam that will impinge on the sample [100].

The cathode ray tube (CRT) is scanned in synchronized with the specimen; therefore, for each beam position on the specimen that is scanned, there is a unique position on the CRT. For low atomic number samples, most of the electrons penetrate deeply into the sample and are, hence, absorbed. However, in high atomic number samples occurs a considerable scattering of the electrons close to the surface. The large depth of focus of the SEM makes possible the three-dimensional appearance of the objects. A large

[10] This beam may be static, or sweeps the sample surface.

[11] Most instruments use a tungsten filament as electron source (cathode) that works in an acceleration potential range of 1-50 kV between the cathode and anode.

number of effects of the interaction occur when the focused electron beam impinges on a specimen surface: high-energy back scattered electrons, low-energy secondary electrons, x-rays, Auger electrons, and radiation in the ultraviolet, visible, and infrared regions [100].

The secondary electrons yield arrives at detectors that form signals which are amplified to control the brightness of the CRT. Some properties of the specimen may affect the beam-specimen interaction, such as topography, composition, crystallinity, magnetic or electric character, and others. This interaction is not the same for all the sample, since it varies from point to point on the samples, consequently, the signals that are produced by the detectors also will vary, therefore, and the points in the CRT will have different values of brightness [100].

It is important to note that the image formation process in the SEM is not equal to the image formation process in an optical or transmission electron microscope. In the SEM, no ray paths exist between the SEM image and the object, as occurs in those others systems. The image does not exist, in fact. It is an abstract construction; or simply a map [100].

For the study of the microstructural properties of the samples of this work, the scanning electron microscopy was performed by using a JEOL JSM-840 Microscope, and the micrographs were taken on fracture surfaces of the samples.

2.2.6 Impedance Spectroscopy

Impedance Spectroscopy (IS) is a powerful technique, which allows to study electrical properties of electrochemical systems and solid-state devices, as well as their interfaces with electronically conducting electrodes. This method is used to investigate the electrical characteristics, such as electrical inhomogeneities, positive temperature coefficient of resistance behavior (PTCR), atmospheric environment (oxidation or reduction reactions), the dynamics of bound (or mobile charges) in the bulk (or interfacial) regions of the material (solid or liquid): ionic, semiconducting, simultaneous electronic-ionic conductivity, and even insulators. Therefore, impedance is defined as the opposition that the circuit offers to the flow of alternating current at a particular frequency. The impedance can be considered a generalization of the relation $R = V/I$, in which when R is a constant value, is then named as the Ohm's Law [74, 101–103].

IS is usually composed by resistive and reactive components (capacitive/inductive) which are determined after the measurement, which is performed in a very wide frequency range ($10^{-2} - 10^{7}$ Hz) [74]. One of the ways to achieve the impedance is by applying an alternating voltage (V_{ac}) across the sample and measuring the current response (I_{ac}), whose signal are both sinusoidal functions and expressed by the following equations [102,

104]:

$$V(t) = V_o \sin(\omega t) = V_o e^{i\omega t} \tag{2.22}$$

$$I(t) = I_o \sin(\omega t - \phi) = I_o e^{(i\omega t - \phi)} \tag{2.23}$$

where V_o and I_o are the amplitude of the voltage and current signals, respectively, ω is the angular frequency ($\omega = 2\pi f$), $\phi = \omega t$ is the phase difference between the voltage and current [12], and t is the time. Thus, the impedance $Z(t)$ is given by:

$$Z(t) = \frac{V(t)}{I(t)} = \frac{V_o e^{i\omega t}}{I_o e^{(i\omega t - \phi)}} = |Z| e^{+i\phi} \tag{2.24}$$

where $|Z| = V_o/I_o$ and represents the magnitude of impedance (absolute value). The values of $|Z|$ and ϕ are obtained directly from equipment meter. Thus:

$$Z' = |Z| \cos\phi, \tag{2.25}$$

$$Z'' = |Z| \sin\phi, \tag{2.26}$$

$$\phi = \tan^{-1}(Z''/Z'). \tag{2.27}$$

In the complex plane, Z is expressed as:

$$Z = Z' - iZ'' \tag{2.28}$$

Here, Z' and Z'' are the real ($\phi = 0°$) and imaginary ($\phi = 90°$) components of Z, respectively, and the magnitude of Z is calculated by $Z = \sqrt{Z'^2 + Z''^2}$. From the Physics point of view, Z' is the resistance or resistive component R (defined by the Ohm's law as the resistance of a sample to current flow), and Z'' is the reactance or reactive component, frequently symbolized as X. The impedance can be characterized in terms of electrical circuit elements: R for a resistance (in a resistor), i.e. the impedance of a resistor is real; $1/i\omega C$ for a capacitance (in a capacitor); and $i\omega L$ for an inductance (in an inductor) [13] [14]. Different regions of a sample are characterized by a resistance and a capacitance, usually placed in a parallel circuit. In order to complement the knowledge, the two basic circuits, series and parallel, will be described.

[12] ϕ is zero when the behavior is purely resistive.
[13] These elements can be connected by applying Ohm's and Kirchhoff's laws.
[14] For each circuit element, a different unit is used: Ω , F, H [V.s/A], respectively.

The series R-C circuit corresponds to a resistor and a capacitor connected in series (see figure 16a). The total impedance is given by the sum of the component impedances of each circuit element, and is expressed as:

$$Z = Z_R + Z_C = R + \frac{1}{i\omega C} \tag{2.29}$$

where Z_R and Z_C are the component impedances of the resistor and capacitor, respectively, and C is the capacitance. In plane and parallel faces dielectric, the capacitance is expressed by:

$$C = \varepsilon_r \varepsilon_o \frac{A}{h} \tag{2.30}$$

where ε', is the relative permittivity ($\varepsilon_r = \varepsilon/\varepsilon_0$), ε_o is the permittivity of free space (8.85×10^{-12} F/m) and A and h are the cross-sectional area and thickness of the samples, respectively [74,102]. Other way to obtain the C value is through the graphic method, by applying the equation 2.31 to the frequency at the maximum of the impedance semicircle [15] in a complex plane (Z'' vs. Z'), and the R values are obtained the intercepts on the Z' axis. The loss factor (ε'' - the imaginary part of permittivity) and conductivity $\sigma(\omega)$ may be calculated from R and C [102]:

$$\omega_{max} = \frac{1}{RC} \tag{2.31}$$

The most common impedance plot used is Z'' versus Z', and the figure 16b shows an example of an impedance plot for series R-C circuit, where the real impedance is the resistance of the material for all frequencies, and the imaginary part follows the similar trend of the ideal capacitor. This representation of the impedance spectrum is commonly referred as the Nyquist's plot [104].

[15] For maximum frequency: $Z' = Z''$.

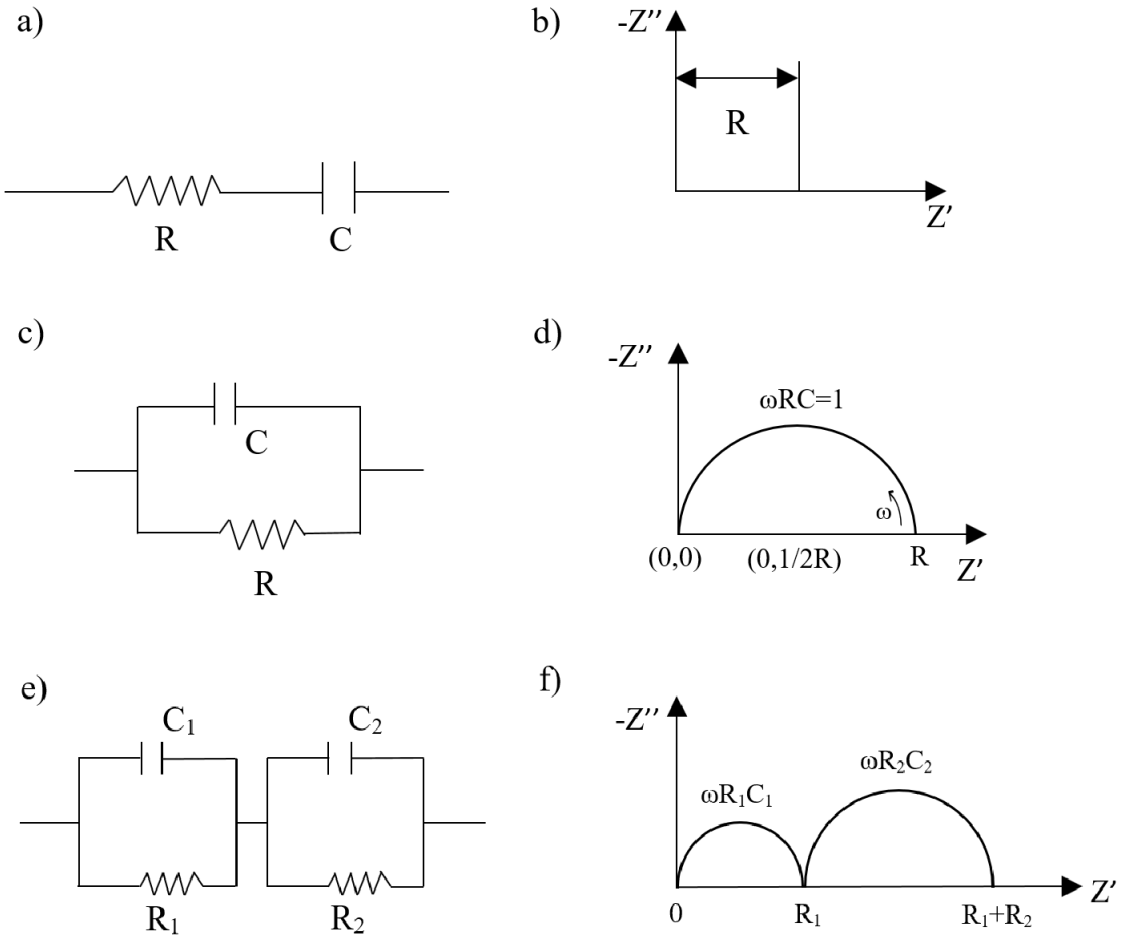

Figure 16 – Representation of the R-C circuits : a)series circuit; c)parallel circuit; e)two parallel RC circuits connected in series; with its respective complex impedance plots b), d) and f). Source: adapted of [102].

On the other hand, the parallel R-C circuit consists in a parallel combination of a resistor and a capacitance, as shown in Figure 16c. The total impedance of a parallel circuit is given by following relations:

$$\frac{1}{Z} = \frac{1}{Z_R} + \frac{1}{Z_C} \tag{2.32}$$

$$Z = \frac{Z_R Z_C}{Z_C + Z_R} \tag{2.33}$$

It is convenient to rewrite the Eq. 2.33 in order to to separate the real and imaginary components of the impedance parts. For this, it is necessary to perform the following step:

$$Z = \frac{Z_R Z_C}{Z_C + Z_R} \cdot \left(\frac{Z_R - Z_C}{Z_R - Z_C} \right) = \frac{Z_R^2 Z_C - Z_R Z_C^2}{Z_R^2 - Z_C^2} \tag{2.34}$$

Substituting Z_R and Z_C by their respective values:

$$Z = \frac{R^2\left(- i\frac{1}{\omega C}\right) - R\left(- i\frac{1}{\omega C}\right)^2}{R^2 - \left(- i\frac{1}{\omega C}\right)^2} \tag{2.35}$$

$$Z = \frac{-i\frac{R^2}{\omega C} + \frac{R}{(\omega C)^2}}{R^2 + \frac{1}{(\omega C)^2}} = \frac{\frac{R}{(\omega C)^2} - i\frac{R^2}{\omega C}}{\frac{(R\omega C)^2+1}{(\omega C)^2}} \tag{2.36}$$

$$Z = \frac{R - i\omega R^2 C}{(\omega RC)^2 + 1} \tag{2.37}$$

Therefore, separating the Z' and Z'' components:

$$Z = \frac{R}{1 + (\omega\tau)^2} - i\frac{R\omega\tau}{1 + (\omega\tau)^2} \tag{2.38}$$

where the first and second terms are the real (Z') and imaginary (Z'') parts of the impedance, respectively, $\tau = RC$ is the relaxation time of the RC circuit, which corresponds to the charging/discharging time of the capacitor [104]. Now, using the relation:

$$\frac{Z''}{Z'} = \frac{-\omega R^2 C}{1 + (\omega RC)^2} \cdot \frac{1 + (\omega RC)^2}{R} = -\omega\tau \tag{2.39}$$

and substituting the Eq. 2.39 in Z'' (Eq. 2.38):

$$Z'' = \frac{R\frac{Z''}{Z'}}{1 + (\frac{Z''}{Z'})^2} = \frac{Z'' R Z'}{Z'^2 + Z''^2} \tag{2.40}$$

Reorganizing, the Eq. 2.40, it can be written in the form of a circle [16]:

$$Z'^2 - RZ' + Z''^2 = 0 \tag{2.41}$$

Now, adding the $R^2/4$ term to both sides of the Eq. 2.41::

[16] Circle equation: $(x - x_o)^2 + (y - y_o)^2 = R^2$

$$Z'^2 - RZ' + Z''^2 + \frac{R^2}{4} = \frac{R^2}{4} \tag{2.42}$$

Reorganizing,

$$\left(Z' - \frac{R}{2}\right)^2 + Z''^2 = \left(\frac{R}{2}\right)^2 \tag{2.43}$$

The Z-plane plot the Eq. 2.43 shows that it forms a semicircle in the first quadrant, where the circle center is obtained at $Z'_o = R/2$ and $Z''_o = 0$, and with a radius 1/2R. It can be seen that the diameter of the semicircle is equal to the resistance (see figure 16d). Each parallel RC elements gives rises to a semicircle from which the R and C values may be extracted. Figure 16e depict a representation of two parallel R-C circuits (R_1C_1 and R_2C_2) connected in series, where $C_1 << C_2$ and $R_2 >> R_1$. From the physical the point of view, the minor semicircle (Figure 16f), which originates in (0,0) point, is related with the relatively high conduction volume of the sample, while the greater semicircle located in (0,R_1) corresponds to a barrier with a weak conducting and a high capacitance [102] [17]. From the impedance spectrum, it is possible to identify different RC elements and associate them to appropriate regions of the sample. Table 5 shows the orders of magnitude of the characteristic capacitances for each region [74].

Table 5 – Capacitance values and their possible interpretation phenomena.

Capacitance [F]	**Phenomenal Responsible**
10^{-12}	bulk
10^{-11}	minor, second phase
$10^{-11} - 10^{-8}$	grain boundary
$10^{-10} - 10^{-9}$	bulk ferroelectric
$10^{-9} - 10^{-7}$	surface layer
$10^{-7} - 10^{-5}$	sample-electrode interface
10^{-4}	elecrochemical reactions

During the IS experiments, the dielectric data of the materials can also be extracted in terms of the frequency dependence of Y^* (the reciprocal of impedance), referred to as complex admittance and is given by $Y^* = Y' + iY''$, where the real part is the conductance (Y') and the imaginary part is the susceptance (Y''). This is generally used because of the direct relation between admittance and complex permittivity, since the dielectric measurements are usually performed to analyze the behavior of permittivity with the

[17] One important information that may obtain from the interface between sample and electrode is whether conducting within the ceramic is ionic or electronic [74].

temperature and frequency of the electric field. For parallel circuits, this direct relation can be expressed by the following equation [103]:

$$Y^* = Y' - iY'' = \frac{1}{R} + i\omega C^* \tag{2.44}$$

where C is mostly associated with pure capacitive behavior and the inverse of R is associated with the losses [18]. Thus, relating the Equation 2.44 with the complex capacitance of the equation 2.30, the real (ε') and imaginary (ε'') components of the permittivity can be obtained, as expressed by:

$$\varepsilon' = \frac{Y''h}{\omega A} \tag{2.45}$$

$$\varepsilon'' = \frac{Y'h}{\omega A} \tag{2.46}$$

Therefore, the complex capacitance C^* offers additional insights about the polarization mechanisms in the dielectric media, since this magnitude is directly connected to the storage properties (related with C') and losses (associated with C'') of electric field energy during the polarization processes [59].

In this work, in order to perform the electrical measurements in the studied KBNN samples were subjected to electrical measurements, for which silver paint electrodes were applied on the major parallel faces by heat treatment at 590 °C. The electrical measurements were carried out at room temperature in an HP4194A Impedance Analyzer towards the frequency range of 100 to 1×10^6 Hz. The results were calculated from the series and parallel circuit models and obtained from fitting process of the experimental data by using the ZView software, which is currently licensed by the IFSC, University of São Paulo.

2.2.7 Dielectric Spectroscopy

Similar to the Impedance Spectroscopy, the Dielectric Spectroscopy (DS) technique is widely used to measure and analyze the (di)electrical properties of the materials, mainly, dielectrics. Therefore, the DS is correlated with the dielectric permittivity of the samples. Permittivity is a material parameter that depends on temperature and frequency of the external alternating electric field, which is varying in time, but not depends on the intensity [102–104] and reduces to the dielectric constant when refers to a static case. Different from the case of an ideal dielectric (stores electrical energy), where the dielectric permittivity is frequency independent, in practice, for a real dielectric (which dissipates electrical energy), the dielectric permittivity is strongly frequency-dependent,

[18] Pure dielectric losses or conductive losses for either series or parallel circuits, respectively

decreasing linearly in most cases with increasing frequency. This technique is used for lower frequencies and allows to study the dipolar rearrangement and lattice polarization mechanisms [101, 104, 105].

Figure 17 shows a representation of the experimental apparatus used in the DS technique, which is compounded by a temperature-controllable furnace, where the sample is placed with a thermocouple to verify the temperature, and connected with the measuring system that is coupled to a computer and an appropriate interface for the data automation. The sample's electrical data are collected, in the case of time-domain DS experiments, by a multimeter or measuring method allowing high-precision current or resistance measurements. For the frequency-domain DS case, the frequency response is collected by using impedance analyzers, or high-precision inductance–capacitance–resistance meters. The electrical data extracted from the DS experiment are most commonly expressed in terms of the frequency dependence of the complex dielectric permittivity ε^*. The DS data representation can also be expressed in other forms since the data presentation can be used for analyzing the dielectric response [103], as is the case of the complex-plane representation (imaginary part ε'' versus real part ε'), similar to the impedance form as seen in the previous subsection [19].

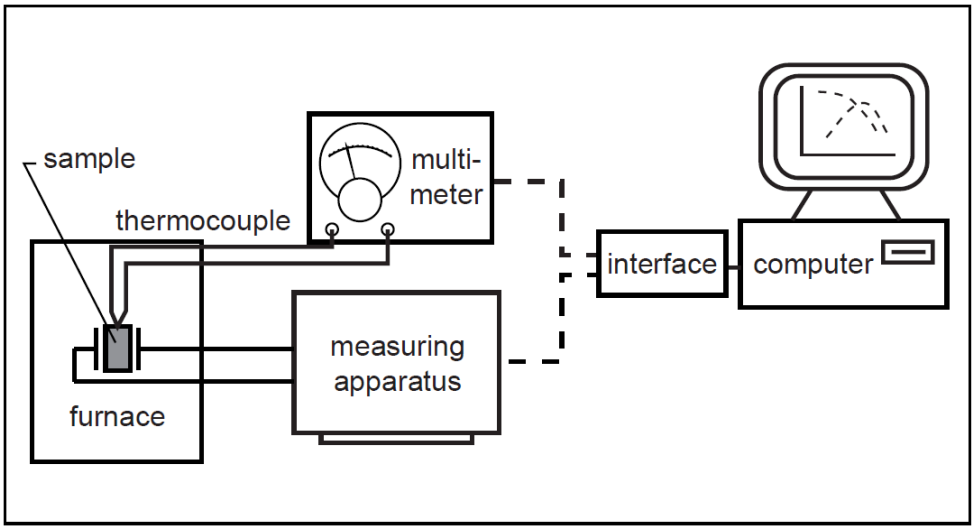

Figure 17 – A simplified diagram of an experimental system for DS. Source: [103].

Peter Debye was the pioneer in describing the theoretical basis of DS [106]. He described the behavior of the material's polarization when subjected to an external electric field, once this electrical field has been removed. In his classical model, Debye considered non-interacting dipoles fluctuating in a continuous medium having the macroscopic

[19] In Ref. [104] there is a table contains all the relationships between the dielectric parameters which the electrical data can be expressed.

viscosity that led to a time dependence of the whole dielectric polarization. Therefore, the variation of the dielectric permittivity with frequency during the dielectric (dipolar) relaxation is described by Debye by the form of the equation 2.47, which takes into account of the complex dielectric permittivity ($\varepsilon^* = \varepsilon' - i\varepsilon''$). The ε_0 and ε_∞ parameters represent, respectively, the low (static) and high-frequency dielectric permittivity, ω is the angular frequency ($\omega = 2\pi f$, where f is the measurement frequency), τ represents the mean relaxation time distribution function and describes the spectrum shape [106]:

$$\varepsilon^*(\omega) = \varepsilon_\infty + \frac{(\varepsilon_0 - \varepsilon_\infty)}{1 + i\omega\tau} \tag{2.47}$$

The Debye's model is capable to describe the behavior of the dielectric response of some materials but, in practice, it disagrees with the response found in most real dielectric materials. This occurs because his model considers not only the absence of interaction between the dipoles but also predicts all the dipoles that compound the material to have only one relaxation time. In fact, according to the Debye's model the dipoles respond all in the same way, and this is not what happens in real materials [103]. In this context, others proposed models emerged in order to incorporate these interactions and processes with more than one relaxation time, consequently achieving better agreement with the dielectric responses found in the experimental data. It can cite some frequently used models such as those proposed by Cole-Cole [107], Dissado-Hill [108], Havriliak–Negami [109], and Jonscher [110–112], which derived their empirical expressions using the Debye's model as the reference equation. Between them, special attention has been paid to the Cole-Cole's model, because it can easily describe the dielectric response in such systems that show very low deviation from the Debye's model. The Cole-Cole's model is commonly represented by the equation 2.48 [107], where α is the exponent parameter, which is related to the relaxation time distribution function and describes the spectrum shape; therefore, its value is shown to be within the $0 \leq \alpha < 1$ interval, in order to obtain the better fit of the experimental data. Note that for α=0, the Debye model is recovered. This parameter has been introduced assuming that each dipole will has a different response with the applied external field and, thus considers different (distribution) relaxation times [107]:

$$\varepsilon^*(\omega) = \varepsilon_\infty + \frac{(\varepsilon_0 - \varepsilon_\infty)}{1 + (i\omega\tau)^{1-\alpha}} \tag{2.48}$$

The dielectric measurements were also carried out at room temperature using the HP4194A Impedance Analyzer in the 100 to 1×10^6 Hz frequency range.

2.2.8 Integrating Sphere Method

In the materials science and technology areas, when referring to those materials commonly used for the development of photovoltaic devices, it is important to study their optical properties, in particular to proceed with the estimation of their optical bandgaps. Integrating Sphere is a fairly used technique to determine these properties, which uses the reflectance spectroscopy to measure the light reflected, transmitted and absorbed by the sample [113,114]. Measurements in the ultraviolet-visible region are usually performed, in which the ultraviolet (UV) and visible (Vis) regions covers approximately the $10-380$ nm and $380-750$ nm range of the electromagnetic spectrum, respectively [113]. In general, UV-Vis spectroscopy offers the fastest and most direct method of estimating the optical bulk bandgap.

From the experimental point of view, the integrating sphere technique is commonly used to measure diffuse reflectance configurations which occurs when the incident beams penetrate the sample, a part of its photons is absorbed and the other part is reflected in all directions. Thus, a typical integrating sphere structure is composed by a resonating spherical chamber whose internal surface is coated with a highly reflective material (usually either MgO or $BaSO_4$), in which this reflective surface causes multiple light reflections inside the sphere, thus minimizing the absorption of the diffuse reflectance [114, 115]. In the spherical chamber there are two (or more) ports where the input port is connected to the light source, the output port is connected to a signal meter system that collects the diffusely reflected light, and an aperture can be necessary to place the samples [116, 117]. Figure 18 presents a scheme for the reflectance and transmittance configurations of an integrating sphere, where the sample is placed at the entrance slit of the integrating sphere to measure the transmittance and placed at the exit slit to measure the reflectance of the sample.

In a UV-Vis spectroscopy measurement, the light absorption is given as function of wavelength (or wavenumber), and provides information about the transitions between electronic energy levels;i.e, from the absorbance spectrum is possible to determine the bandgap energies in the UV-Vis region of the material [117]. Lambert [118] and Beer [119] developed, independently, a relation that correlates the fraction of light measured after the interaction with the sample (I) and the incident intensity (I_0), with the path length of light through the sample (l). This relation is given by equation 2.49 and is shown as the Lambert-Beer's Law, where I, is the measured intensity (usually as transmittance or reflectance) of the light, σ is the absorption cross section of the sample's transition, and the difference in the population of the initial (N_1) and final (N_2) are the initial states:

$$\frac{I}{I_0} = e^{-\sigma(N_1-N_2)l} \tag{2.49}$$

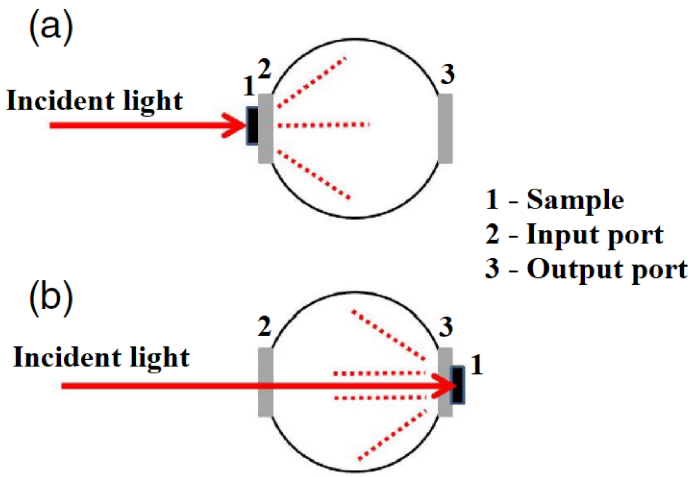

Figure 18 – Representation of an integrating sphere for determining the optical properties of the material. (a) Transmittance mode. (b) Reflectance mode. Source: adapted from [114].

The equation 2.49 is often simplified and represented as the Beer's Law, by the equation 2.50, where A, is the absorbance, ε is the molar absorpitivity coefficient of the material, and c is the concentration of the absorbing samples:

$$A = \varepsilon cl = -\log_{10}\left(\frac{I}{I_0}\right) \tag{2.50}$$

Normalizing the absorbance (equation 2.50) with respect to l, it is possible to obtain the absorption coefficient, which is given by the equation 2.51:

$$\alpha(cm^{-1}) = \frac{\ln(10) \times A}{l(cm)} = \ln(10)\varepsilon c \tag{2.51}$$

In order to facilitate the determination of the bandgaps, the conversion between wavelength (in nm) and bandgap energy (in eV) units is carried out, since the spectra are reported in wavelength of light units, and is given by [117]:

$$h\nu(eV) = \frac{hc}{\lambda} = \frac{1239.8(eV \times nm)}{\lambda(nm)} \tag{2.52}$$

where h is the Planck's constant ($6.62 \times 10^{-34} Js$), ν is the photon energy (light frequency), c is the light velocity in vacuum ($2.99 \times 10^8 m/s$) and λ is the wavelength. To obtain the absorption coefficient from the measured intensity, the instrument software will usually

use the equation 2.51 and performs the necessary fits, taking into account the reflectance and scattering effects as well. For those cases where $\alpha > 10^4 cm^{-1}$ often obey the relation presented by Tauc [120] and supplied by Davis and Mott [121], as expressed by the equation 2.53, where E_g , is the ground state energy, n can take on values of 1/2, 3/2, 2, or 3, which correspond to direct (allowed), direct (forbidden), indirect (allowed), and indirect (forbidden) transitions, respectively [122]. Thus, the plots of $(\alpha h\nu)^n$ vs. $h\nu$ are called as Tauc plots:

$$\alpha h\nu \propto (h\nu - E_g)^n \tag{2.53}$$

The bandgap in the absorption spectrum is determined by drawing a tangent line to the curve and extrapolating to the baseline in the Tauc's plot. The bandgap value will be then the intercept with the energy axis. In other words, the bandgap corresponds to the point at which absorption begins to increase from the baseline. This point indicates the minimum energy that a photon must have to excite an electron from the valence band to the conduction band and, thus, be absorbed in the semiconductor material [117].

For determining the optical properties in this work for the KBNN samples in the UV-Vis region, a 2 inches, four-port integrating sphere from Thorlabs 15200-4 Inc, and a halogen lamp were used, which allowed to obtain the absorbance spectra from the collected data of diffuse reflectance plus diffuse and collimated transmittances. The data were simultaneously processed with a mathematical model for estimating the optical parameters of interest [123].

3 RESULTS AND DISCUSSION

3.1 Structural Properties

3.1.1 X-Rays Diffraction (XRD)

For the study of the structural properties of the KBNN samples, after calcination, the XRD measurement was performed, in order to identify the formed phases. Figure 19 shows the XRD patterns from the calcined KBNN samples, as measured at room temperature. For all the studied compositions the obtained patterns were successfully indexed according to the ICSD-9535 collection code, which corresponds to a weak-tetragonal perovskite structure with a P4mm space group [124], in agreement with data reported in recent works [10, 51]. Results reveal that the ferroelectric phase was successfully formed in all compositions. On the other hand, a secondary phase also was observed in the KBNN01 and KBNN03 samples with very small impurity peaks, and identified by the ICSD-9866 collection code, which correspond to the non-ferroelectric NiO phase with centrosymmetric F$m\bar{3}m$ space group, as indicated with an asterisk (*) in the same figure [125].

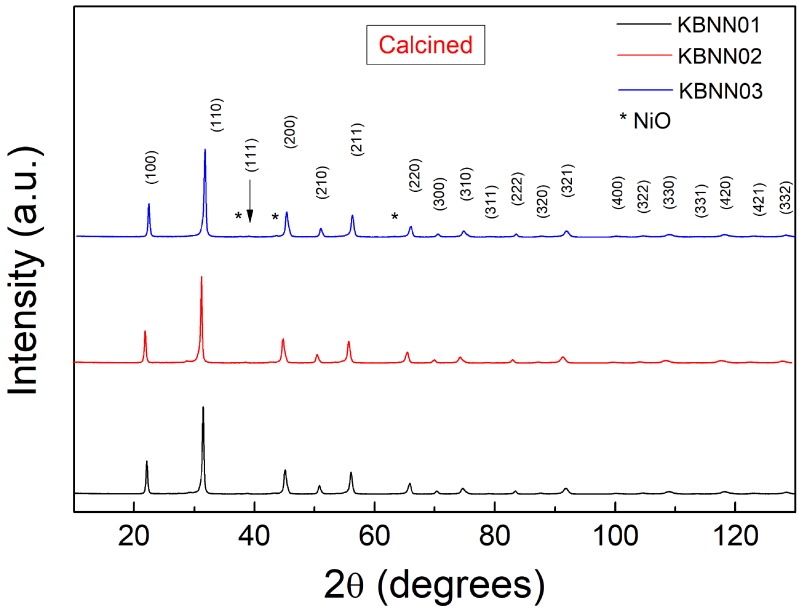

Figure 19 – X-rays diffraction patterns of the studied calcined KBNN samples, collected at room temperature, with the peaks properly identified by the respective Miller's indices.

Figure 20 shows the XRD patterns from the powdered KBNN ceramics, now after the

sintering process. It can observe that the secondary NiO phase was not totally eliminated, even under very high temperatures. However, the contribution of this secondary phase is negligible with respect to the desired ferroelectric phase already formed. Therefore, in principle, it will not influence the main physical properties.

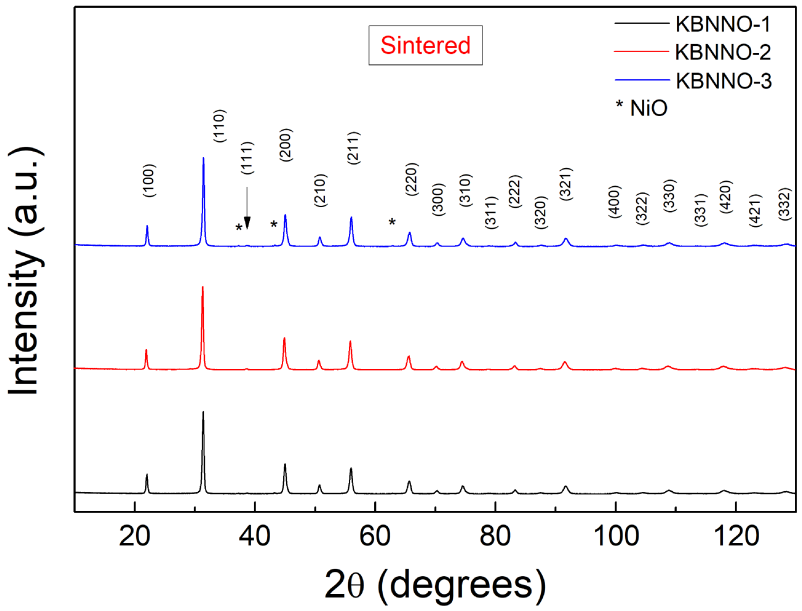

Figure 20 – X-rays diffraction patterns of the sintered powdered KBNN ceramics, collected at room temperature.

A detailed investigation on the structural characteristics of these materials was carried out by a refinement analysis of the above XRD patterns (figure 20) through the Rietveld method, using the Fullprof Suite Package software [126], the results of which are shown in Figure 21. The experimental (observed) and theoretical (calculated profiles) data are represented by open circles (in red) and solid lines (in black), respectively. The vertical marks, below the patterns, correspond to the calculated Bragg's reflections. The differences between the experimental and theoretical data are identified by the bottom green lines. As for the KBNN01 and KBNN03 compositions, traces of NiO were observed, then two different initial structural models were considered for the calculation of the diffraction patterns: (i) a non-centrosymmetric P4mm space group (ICSD-9535) for the tetragonal ferroelectric KBNN phase [124] and (ii) a centrosymmetric F$m\bar{3}m$ space group (ICSD-9866) for the cubic non-ferroelectric NiO phase [125], as previously commented. The starting structural data for refinement were taken from the "Inorganic Crystal Structure Database" (ICSD) [127], and the resulting parameters are all illustrated in table 6. The values obtained for the goodness-of-fit parameters (R_p, R_{wp} and χ^2) are indicative of a high-quality data refinement, evidencing a good agreement between the experimental (ob-

served) and theoretical (calculated) results, which indicates that the KBNN system has a weak tetragonal phase at room temperature.

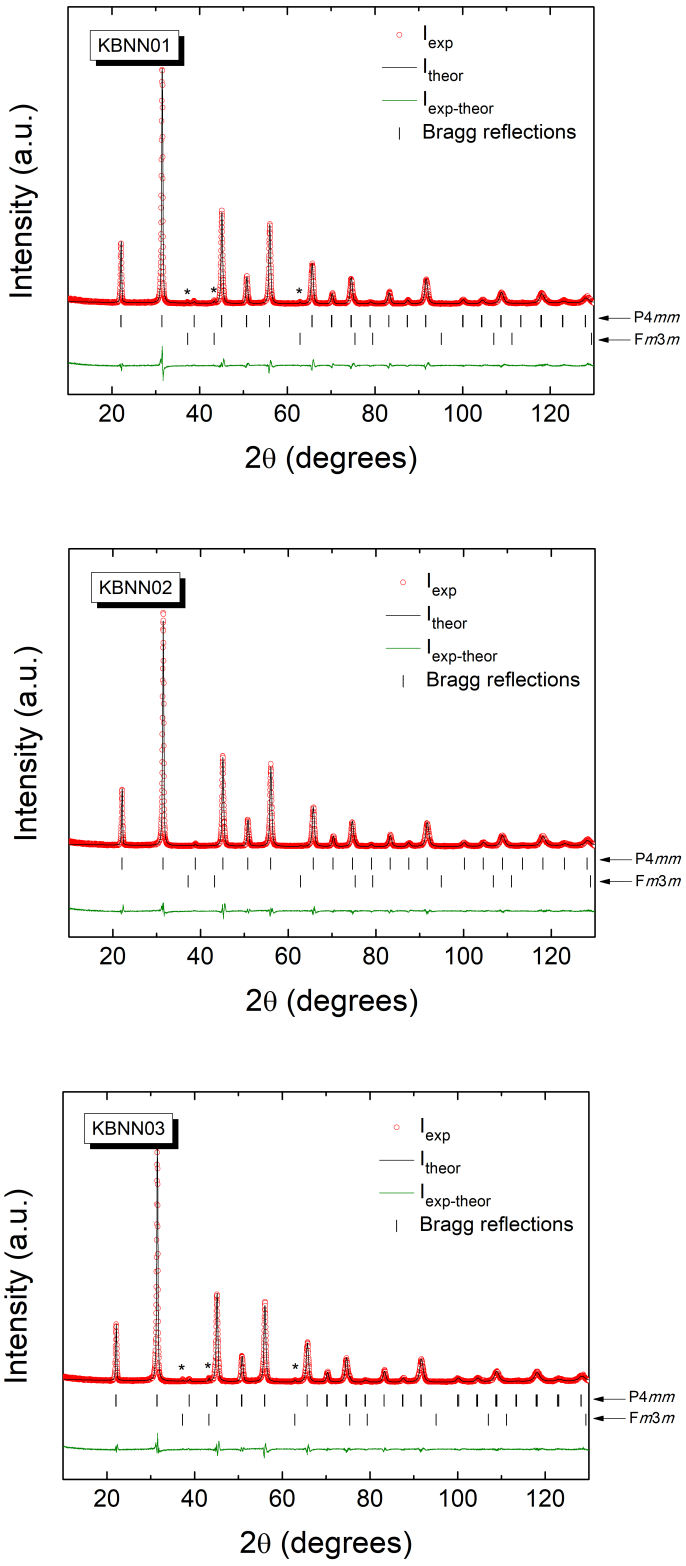

Figure 21 – Rietveld refinement of the X-ray diffraction patterns for the studied KBNN compositions.

Table 6 – Unit-cell (a, b y c), volume (V) and goodness-of-fit (R_p, R_{wp} and χ^2) parameters obtained after the refinement process, resulting in a weak-tetragonal ferroelectric phase with P4mm spatial group for all the compositions. Data for the resulting theoretical density (ρ_{theo}) of the materials are also included.

	KBNN01	**KBNN02**	**KBNN03**
a=b (Å)	4.014(1)	4.015(4)	4.017(8)
c (Å)	4.021(1)	4.021(1)	4.021(6)
V (Å^3)	64.79(2)	64.83(4)	64.92(0)
R_p(%)	9.3	9.5	10.5
R_{wp}(%)	12.9	13.5	14.1
χ^2	3.1	3.3	3.6
$\rho_{theo}(kg/m^3)$	4825.8	4770.4	4647.0

It is timely pointing out that the apparent densities of these materials after sintering (calculated by the equation 2.1) were found to be around 4365.0, 4353.0 and 4352.0 kg/m^3, meaning to be dealing with basically dense samples with relative density values (calculated by the equation 2.2) of 90, 91 and 93 % for KBNN01, KBNN02 and KBNN03, respectively (the theoretical density value, ρ_{theo}, for each KBNN composition has been listed in table 6).

For the sake of comparison, figure 22 depicts a magnification of the XRD data towards the $2\theta \approx 45°$ region. The (200) reflection peak is there noted to move towards lower angles values as the oxygen vacancy (δ) content increases when going from KBNN01 to KBNN03. This is consistent with a weak tetragonal ferroelectric phase [10] and also is a indicative of a unit-cell expansion with increasing δ, in agreement with results reported for perovskite-type (ABO_3) oxides [128], and it is in correspondence with the obtained theoretical unit-cell volume (V) reported in Table 6, which changes from 64.79 Å^3 to 64.92 Å^3 when going from KBNN01 to KBNN03. This increase in the unit-cell volume can be ascribed to the increase in lattice parameters due to an increase in the Ni^{2+} content into the perovskite structure, whose ionic radius is larger (0,69 Å) than the Nb^{5+} (0.64 Å) ion [10]. Furthermore, the fact that the nickel cation has 2+ valence, leads it to occupy B-site because of the chemical affinity. The ionic radius of the Ba^{+2} (1.35 Å) ion is slightly lower than the ionic radius of the K^{+1} (1.38 Å) ion. However, the barium ion incorporation into the KBNN structure revealed to have a lower significant effect on the lattice volume change, which could be due to the smaller difference of the ionic radii between both ions at the dodecahedral site [54]. Therefore, the inclusion of a larger ion at the B-site in the crystal structure favors an increase in the unit-cell volume.

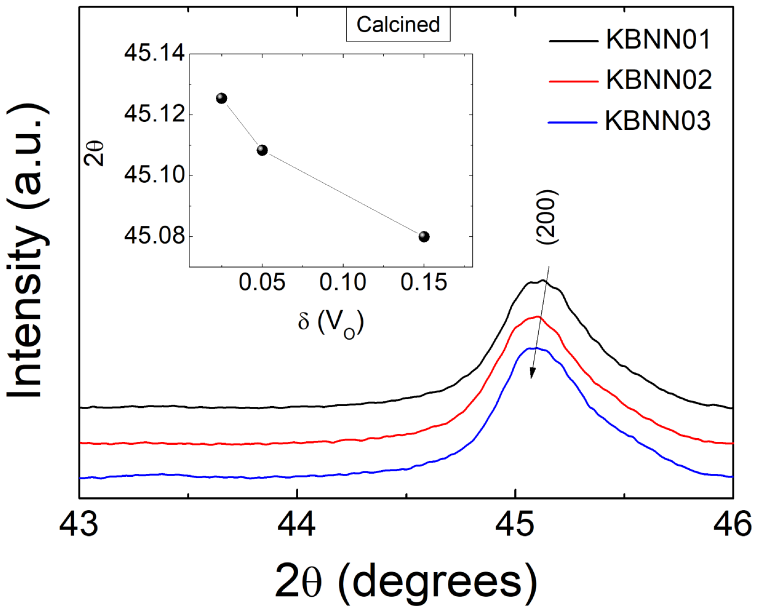

Figure 22 – X-ray diffraction patterns of the studied KBNN powdered ceramics, collected at room temperature, rescaled in the 2θ range of 43–46°.

First principles calculations have in fact revealed that the lattice volume expansion in such materials originates from the repulsion force between the cations and positively-charged oxygen vacancy defects, promoting a decrease in the covalence of the B–O bonding [128]. It is known that the presence of oxygen vacancies causes a domain wall pinning effect, that is, the domain wall motion is suppressed because of defect dipoles of acceptor ions and oxygen vacancy. This result seems to be not favorable for such applications where ferroelectric systems are excellent candidates, as is the case of transducers and infrared sensors, in which the piezoelectric and/or pyroelectric coefficients, respectively, have to be strong. However, from another perspective, which is in accordance with the aim of the present work, the simultaneous combinations of Ni^{2+} ions and oxygen vacancies reveals to be a very important mechanism to elevate electronic states and consequently, decrease the material's bandgap [51].

3.1.2 Raman Spectroscopy

Raman spectroscopy is very sensitive to changes in lattice vibration and it was also used to analyze the local structural properties and phase evolution of the KBNN compositions and used to investigate the effects of Ni^{2+} and Ba^{2+} doping on the hosting matrix ($KNbO_3$). The Raman data are shown in figure 23, in which the spectral signature for the KBNN solid solution is confirmed, where seven modes were identified and are labeled from M_1 to M_7 in the spectra.

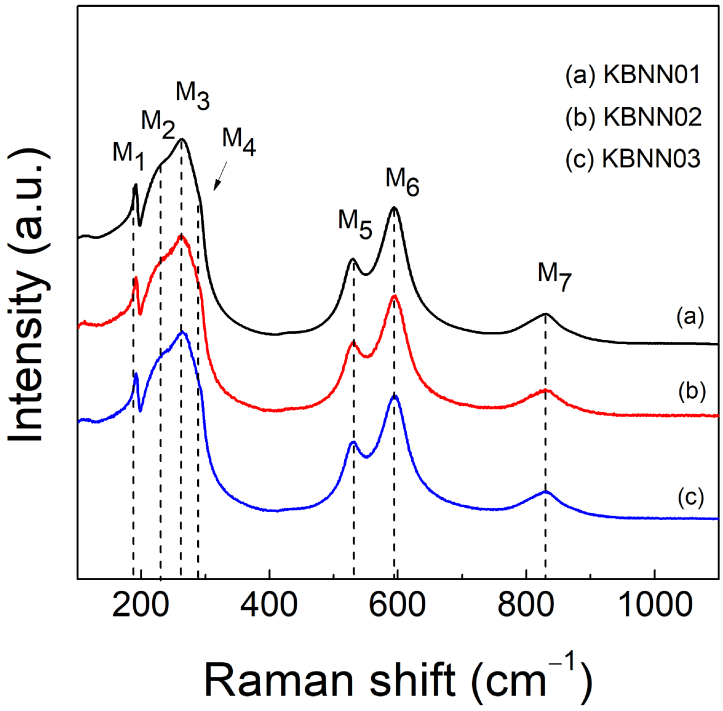

Figure 23 – Raman spectra for the studied KBNN compositions, performed at room temperature.

In order to find the number of vibration modes that appear in the Raman spectra, as well as their positions (frequency values), a mathematical procedure proposed by Buixaderas et al [129] was used which consists of locating the points called CMCD points, i.e., Raman spectral regions where the maxima curvature in concave-down, using the analysis of its frequency derivatives. Therefore, through the deconvolution of the peaks, these points can be found when only those positions where the third derivative of the fitted curve is equal to zero, $d_3(\omega) = 0$, and the second derivative has a negative minimum, that is, $d_2(\omega) < 0$. Thereby, the fittings were initially made considering a greater number of peaks (considering the number of visible modes) to obtain the fitted curve closest to the experimental spectrum, using the Origin 8 pro software. Subsequently, the second (d_2) and the third derivative (d_3) of the fitted curve were obtained to locate the CMCD points, which are found using the above cited conditions stated previously. Figure 24 shows the fitting spectra using the Buixaderas' method for all the samples, where the CMCD points are indicated by arrows and the frequency value for each mode was determined from the negative minimum of the second derivative. For all the compositions, the seven modes labeled previously as M_1 to M_7 were found and their respective frequency values are identified in table 7. Furthermore, in table 8 are also presented the modes reported for other $KNbO_3$-based systems that were used to support the identification and comparison of the modes found for the studied KBNN samples in this work. It is possible to observe that

the values of the frequencies of the found modes are too close to those reported in the literature [36, 52].

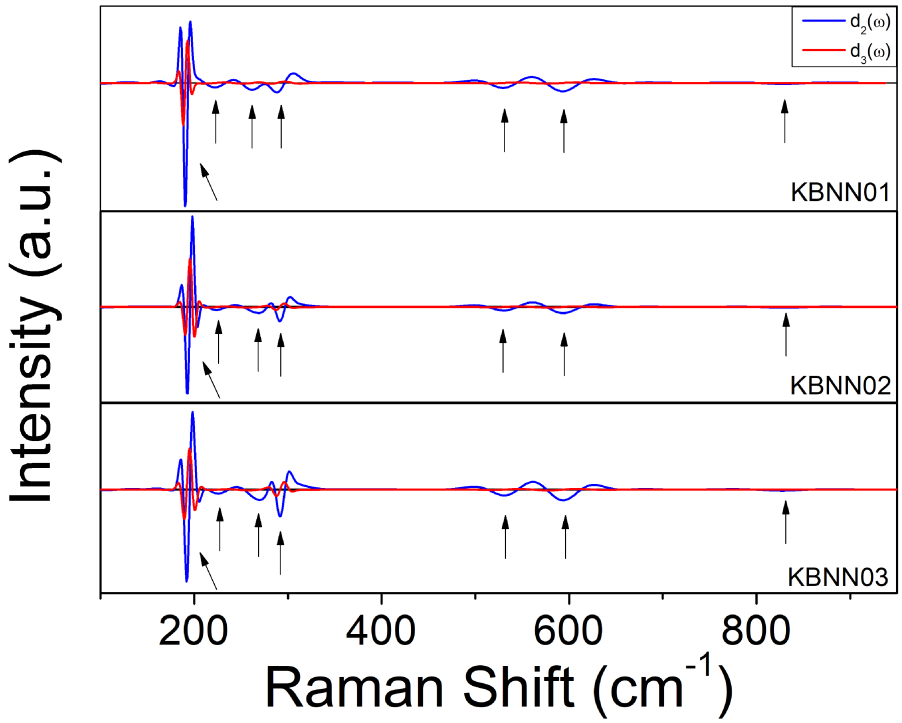

Figure 24 – Maxima curvature in concave-down analyses of the Raman spectra for the KBNNO samples. The arrows indicate the CMCD points founded using the $d_2 < 0$ and $d_3 = 0$ conditions.

Table 7 – Wavenumber and the assigned vibrational modes for the studied KBNN.

Modes	**Wavenumber** (cm^{-1})			**Modes assignment**
	KBNN01	**KBNN02**	**KBNN03**	
$(B_1, B_2)(TO_2)$	190	193	191	long-range polar order [130]
$B_1(TO_1)$	221	224	225	O-Nb-O bending vibration [53]
$A_1(TO_1)$	261	268	270	bending of $BO_6 octahedral$ [130]
$A_1(TO_4, LO_4)$	288	291	291	long-range polar order [130]
$(B_1 + B_2)(TO_3)$	529	530	531	O-Nb-O stretching [13]
$A_1(TO_3)$	593	593	594	O-Nb-O stretching [13]
$A_1(LO_3)$	829	829	827	stretching of BO_6 octahedral [13]

Table 8 – Fundamental wavenumber with their symmetry modes reported at room temperature for other $KNbO_3$-based systems.

Modes	Wavenumber (cm^{-1})	
	$KNbO_3$ [52]	$0.80KNbO_3-0.20BaNi_{0.5}Nb_{0.5}O_{3-\delta}$ [36]
$(B_1, B_2)(TO_2)$	189	193
$B_1(TO_1)$	230	220
$A_1(TO_1)$	267	268
$A_1(TO_4, LO_4)$	289	290
$(B_1 + B_2)(TO_3)$	530	528
$A_1(TO_3)$	596	594
$A_1(LO_3)$	835	832

After the fitting process, all the decomposed peaks have been represented together with the experimental and theoretical results, as shown in figure 25, from which spectral signature of the ferroelectric response in the KBNN system can also be confirmed for all the compositions [13]. The observed band below 170 cm^{-1} is associated with translational modes related to the A–O vibrations [130], being the characteristic for the occurrence of nano-sized clusters rich in K^+ (or Ba^{2+}) cations. The $A_1(TO_1)$ mode observed around 270 cm^{-1} is assigned to BO_6 bending vibrations (represents a triply degenerate symmetric O–Nb–O bending vibration), whereas the two sharp $(B_1B_2)(TO_2)$ modes and the $A_1(TO_4)$ mode, observed around 192 cm^{-1} and 290 cm^{-1}, respectively, have been postulated to be a fingerprint for the occurrence of long-range polar order (that is, the signature of ferroelectricity) in KNO-based systems [52, 131]. Towards the higher wavenumber region ($>$500 cm^{-1}), the observed modes are characteristic of the oxygen octahedral vibrations [11]. Therefore, the modes observed around 530, 593, and 830 cm^{-1} are related with the stretching of the BO_6 octahedra due to the presence of Ni^{2+} in the structure [11, 13, 132].

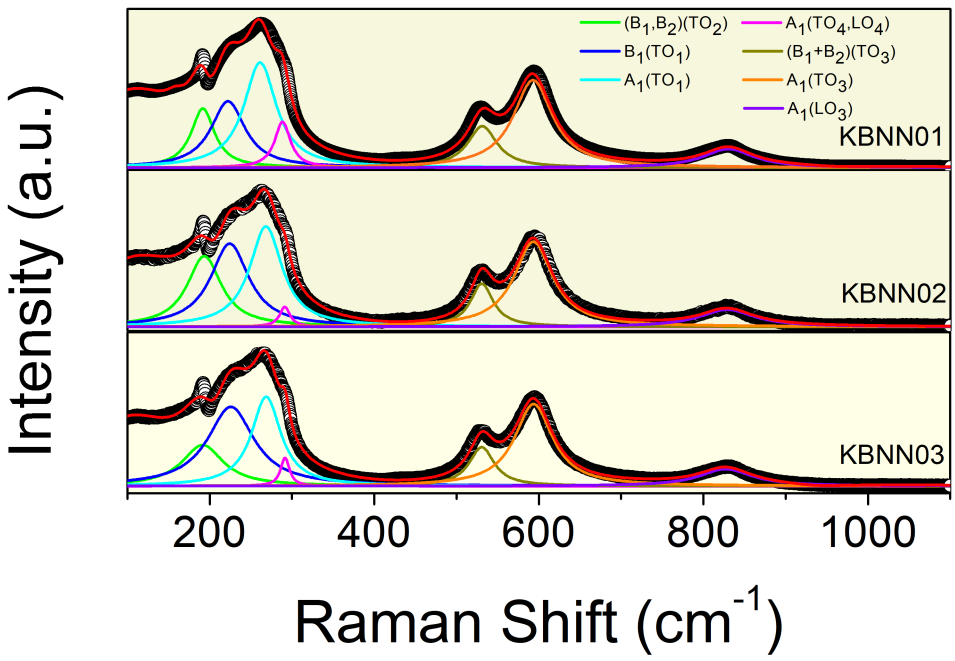

Figure 25 – Raman spectra for the studied KBNN compositions, showing the experimental and theoretical spectra as black symbol and red line, respectively. Deconvolution of the peaks are shown as colored lines, according to the obtained different vibrational mode Buixaderas method.

In addition, it is noticed that the most considerable change that has taken place in the Raman spectra has been in the M_3 mode, which is the only one that shows a relevant increase in the values of the Raman frequency (or wavenumber – 9 $cm^{-1} \pm 1$) as the concentration of oxygen vacancies increases (see table 7). This mode was identified as $A_1(TO_1)$ and, as already mentioned, it is related with the BO_6 bending vibrations. This result suggests that the B-O bonds distances are decreasing, and consequently, the bond strength between the O-B-O ions are increasing with the increase of the oxygen vacancies. Therefore, this frequency behavior is expected (since $\omega = \sqrt{\frac{k}{m}}$) because if there is a smaller number of oxygen ions in the octahedral, consequently the effective mass decreases, which favors to a higher vibrational frequency. On the other hand, an additional fact that contributes it is that as the Ni ion is being introducing into the Nb-site, and the Ni cation is less heavy than the Nb ion. As can be observed, still regarding figure 25, a slight decrease in the relative intensity of the $A_1(TO_1)$ and $A_1(TO_4, LO_4)$ modes, as well as in the intensity of the sharp $B_1(TO_2)$ mode, is noted when going from KBNN01 to KBNN03. This result could be an indicative of a decrease in the long-range polarization in the ferroelectric material caused by an increase in the oxygen vacancies concentration.

Since the intensity of the modes are related with the polarizability, this decrease in the relative intensity also indicates a decrease in the polarizability in these modes.

For a better understanding and "visualization" of the phonons, there are some explanations on how the transverse optical (TO) modes occur. The TO_1 mode is especially indicative of polarization in the material due to the parallel alignment of the polarization vector and the Nb-O bond; that is to say, the central B-site ions oscillating against the oxygen octahedra. The TO_2 mode corresponds to the A-site atoms vibrating in opposite direction to all the BO_6 octahedral structures. Some authors have related this mode with the signature of ferroelectricity in KNO-based solid solutions [26, 53, 133]. The TO_3 mode is associated with the B-site ions and the oxygen ions oxygen from the top and bottom faces moving parallel along the polarization vector, and anti-parallel to the equatorial oxygen atoms, while the A-site ions remain stationary. Finally, the TO_4 mode corresponds to the equatorial oxygen ions moving anti-parallel to their nearest equatorial oxygen neighbors, and vibrating out of phase along the polarization direction, while the A and B-site ions and apical O ions are fixed [53].

Moreover, when adding the Ni^{2+} ion at B-site of the structure, besides the induction of local strains, as mentioned previously, it also promotes the interruption in the Nb–O covalent bonding, which is responsible for the long-range ordered displacement of Nb^{5+}. Thus, the lattice disturbance caused by this doping affects the balance between long-range dipolar Coulombic forces and short-range repulsion forces. Therefore, this result could be an indicative of a decrease in long-range polarization in the ferroelectric material caused by an increase in the oxygen vacancies concentration [11].

3.2 Microstructural Properties

3.2.1 Microstrain and crystallite size analyzes

For the study of the microstructural properties the individual contributions from the average crystallite size (D) and lattice microstrain (η) to the broadening of the reflection peaks were analyzed by applying the Williamson-Hall (W-H) method, as expressed by the equation 2.15. Figure 26 shows the oxygen vacancy concentration (δ) dependence of D and η for the three studied compositions. While D kept at the nanoscale, slightly decreasing with raising δ, an increase of η is rather registered.

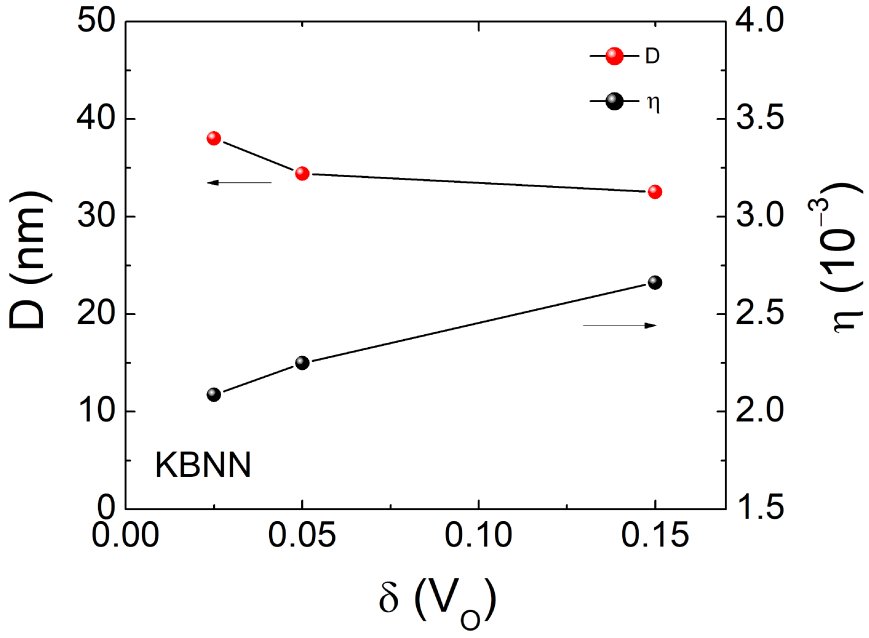

Figure 26 – Crystallite size (D) and lattice microstrain (η) as a function of the oxygen vacancy concentration (δ) obtained from the Williamson-Hall method, according to equation 2.11.

From the fundamental viewpoint, as already discussed in the previous section, the aforementioned Williamson-Hall is a generalization of the so-called Scherrer's formula [86], allowing to predict not only the average crystallite size from XRD experimental data (as in the Scherrer's equation), but also additional contributions to the peaks profile, including instrumental effects and induced microstrain into the crystalline lattice. As also noted in the previous section, it is known that the main contribution to the width of diffraction peaks arises from lattice microstrains, which are strongly affected by structural defects [93, 134]. Accordingly, the higher the defects concentration the higher the lattice microstrain, leading to an increased width of the diffraction peaks profile, as observed in the present work (Figure 22), driven here by the oxygen vacancy defects. Therefore, the increase in η from KBNN01 to KBNN03 is expected due to a large concentration of induced defects in the lattice. Moreover, all samples were observed to be nanocrystalline powders. It is worth emphasizing that, since the XRD patterns were collected on powdered sintered samples, the isotropic approximation is guaranteed [93], in which case the crystallites are considered to have spherical morphology as well as an isotropic distribution of the microstrain, ensuring the applicability of the Williamson-Hall model.

3.2.2 Microstructure analysis from SEM

The SEM micrographs of fracture surfaces obtained in all the studied KBNN ceramics are shown in figure 27. The results reveal microstructures consisting of agglomerated particles with interconnected structures, and grain-size uniformly distributed over the surfaces showing dense structures with only few pores recognized, complementing the results previously calculated for the density of the ceramics. From these images, the average grain-size values (ϕ) were calculated using the ImageJ software and the obtained results are presented in table 9 (in meters - m), the values of which showed a slight increase from KBNN01 to KBNN03. Similar results, showing agglomerated particles with interconnected structures have been reported for KBNN based ceramics [13, 51].

Table 9 – The average grain sizes (ϕ) from the studied KBNN ceramics.

Material	ϕ **[μm]**
KBNN01	0.32
KBNN02	0.43
KBNN03	0.51

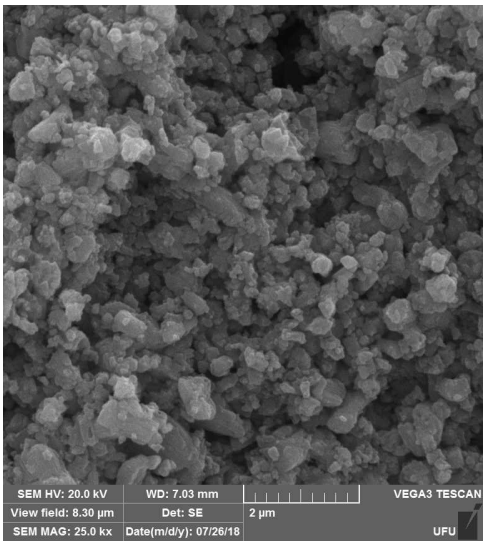

(a) KBNN01

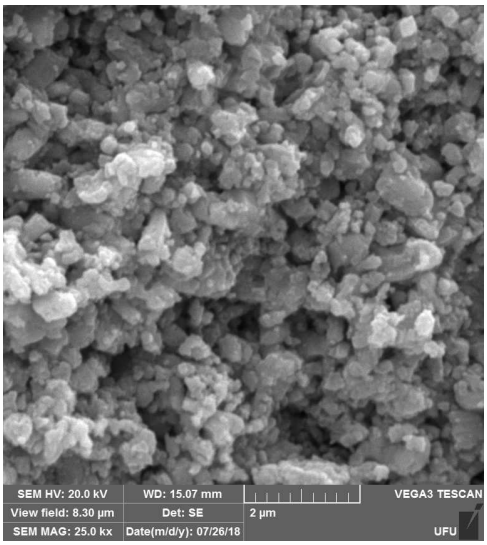

(b) KBNN02

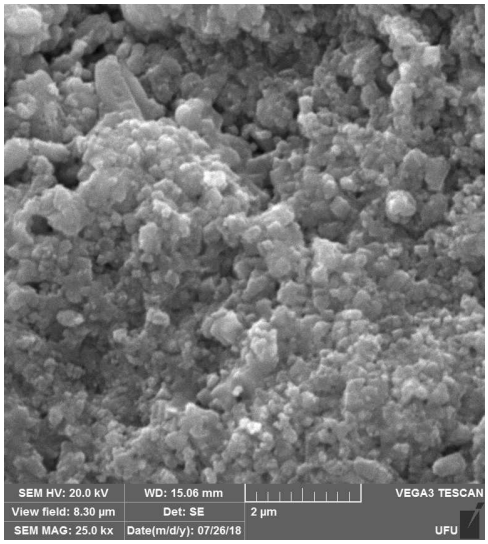

(c) KBNN03

Figure 27 – SEM micrographs of fracture surfaces obtained in the all compositions.

In addition, the observed behavior exhibiting an average grain-size increase in perovskite-structured systems, while raising the oxygen vacancy defects, have been reported for other lead-free ceramic compounds [135, 136]. This effect is likely linked to a charge decompensation during charge diffusion for achieving the end structure, noting that a grain-size increasing trend is also conceivable because the presence of oxygen vacancies presence should be expected to enhances mass transport and, hence, grain-boundary mobility during sintering.

3.3 Electrical Properties

3.3.1 Dielectric Dispersion

In order to analyze the influence of the oxygen vacancy defects in the dielectric response, the frequency dependence of the real and imaginary components of the dielectric permittivity (ε' and ε'', respectively) has been performed, as shown in figure 28 for the KBNN01, KBNN02 and KBNN03 compositions. It can be seen that the dielectric dispersions show a decrease in both ε' and ε'' with the increase of the oxygen vacancies.

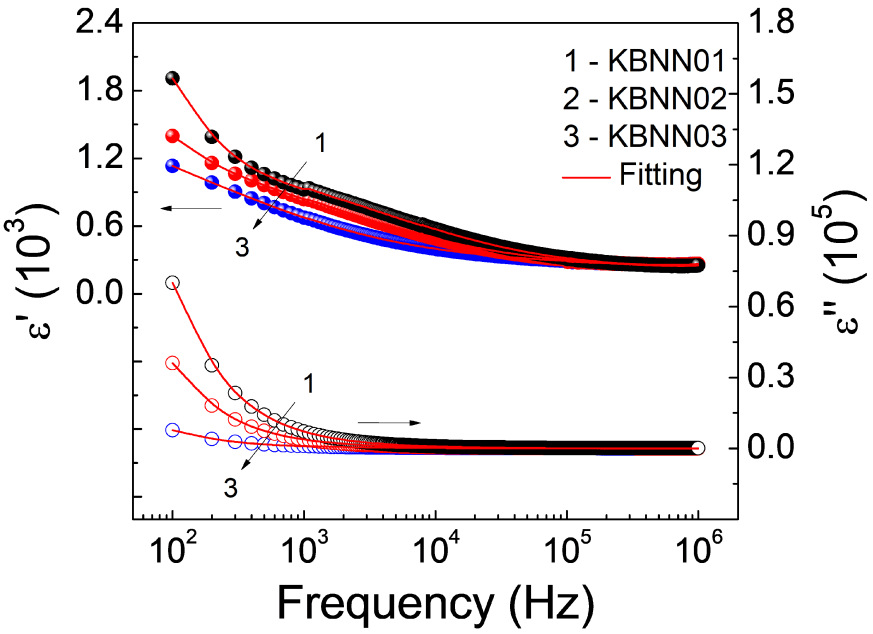

Figure 28 – Frequency dependence of the real (ε') and imaginary (ε'') dielectric permittivity, obtained at room temperature, for the studied compositions, where the red line is the fit of the results.

From the fundamental point of view, as above mentioned, it is known that in ferroelectrics, structural defects (such as oxygen vacancies) promote the well-known domain-wall pinning effect, where the suppression of the domain-wall motion could be caused by dipolar defects that involve cations-oxygen vacancy pairs. These defect mechanisms promote a shrinkage in some physical properties such as dielectric permittivity, dielectric losses and electromechanical response [137, 138]. Similar behavior has been reported by Hoshina *et al.* [128], revealing a decrease of the intrinsic dielectric permittivity in the presence of oxygen vacancies, which has been ascribed to the hardened of the Slater-type phonons (soft mode) in perovskite structure materials; that is to say, the results induce a weakening in the covalency of the B-O bonding. It is also known that the decrease in the effective ion mass is also considered as a reason for the hardened of the Slater mode

(increase of frequency) [128]. Thus, the addition of the Ni^{2+} ion, with a lower mass (58.693 u) than Nb^{5+} (92,906 u) [139], consequently, suggests a contribution to decrease the dielectric permittivity.

In order to better investigate the dielectric relaxation as well as the influence of the vacancy defects, the experimental results were fitted by considering the semi-empirical Cole-Cole model, using the equation 2.45. As can be seen in the same figure 28, a good agreement between the experimental data (symbols) and the theoretical fitting (solid-lines) was observed for all the analyzed compositions. The obtained values for α were found by fitting the curves of the dielectric pertmittivity vs. frequency and are in the range of around 0.4–0.6, which reveals the deviation from the ideal Debye's dielectric relaxation [106, 140]. Results also revealed very low dielectric losses at high frequencies (≈ 0.001), which is a fundamental characteristic for applications in electronic devices.

It is known that when a polarization mechanism finishes to function, there is an abrupt drop in the dielectric permittivity (as can be seen in Figure 28), otherwise, ε continues virtually frequency independent [88]. Therefore, the obtained result in Figure 28 confirms the strong influence of the structural defects in the dielectric response of the studied materials, which might affect the real dipolar mechanism by promoting unexpected conduction processes [59], thus indicating that some electrons are being excited to energies within the conduction band. The high value of dielectric permittivity at a low-frequency region is attributed to space-charges (thermal charges) polarization, which is induced because of lattice defects. Such effect can be associated with the charge distribution of hopping carriers on defects, and is determined by the quantity of these thermal charges, porosity, defects, and minor phases present in the studied material [141, 142].

3.3.2 Resistivity Analysis

As Impedance Spectroscopy is an important complement for the understanding of the microstructure through the transport properties of the samples, it is required to analyze the impedance measurements. Therefore, the impedance results have been presented in this work in terms of the complex resistivity ρ (Ωcm) for a better understanding of the data, since the conduction contribution will be analyzed. In this context, considering the geometrical factor of the samples: $L(\equiv A/h) \approx 6 \times 10^{-2}$ m, where A is the electrode's area and h is the sample thickness, and using the criterion of magnitude order of capacitance [143–145], the impedance data (given in terms of resistivity in the frequency domain) measured at room temperature on the prepared KBNN ceramic samples are shown in figure 29.

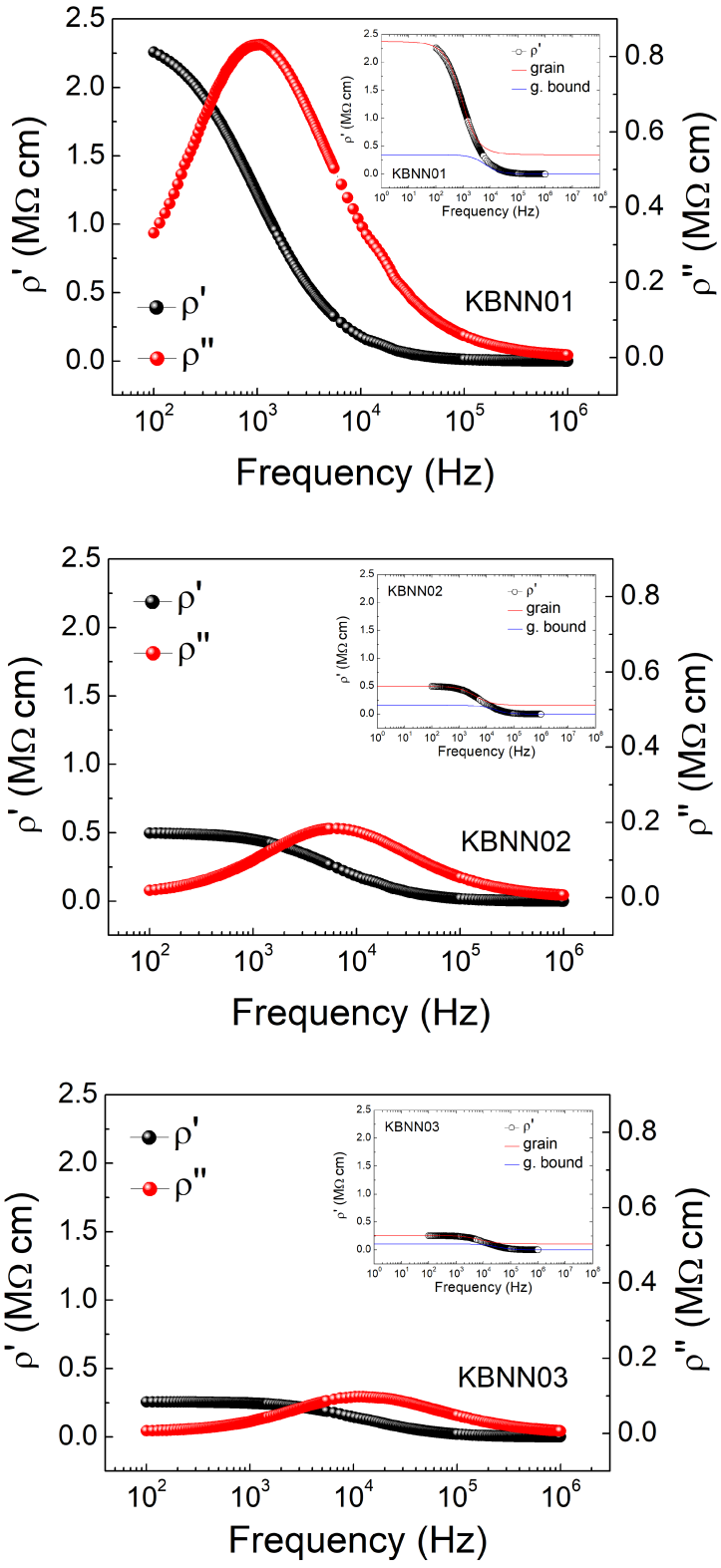

Figure 29 – Frequency dependence of the real (ρ') and imaginary (ρ'') parts of resistivity for the KBNN samples. Figures insets show the fitting of ρ' considering both grain and grain-boundary contributions (solid-lines).

It is known that for a simple hopping conductivity process, in the absence of long-range interactions, the conductivity is expected to be independent of frequency, the physical mechanism is dominated by hopping backward and forward process of a single particle in double well, where the low-frequency conductivity is zero, and a Debye-like transition region is followed by a constant high-frequency conductivity [101].

Impedance data (given in terms of imaginary versus real parts of resistivity) measured at room temperature on the prepared KBNN ceramic samples are presented in the Figure 30. Each spectrum consisted of two semicircles that could be fitted by using two parallel resistance-capacitance (R-C) networks, both connected in series. Through the equation 2.31 and according to the table 5, the two dielectric responses (referent to the semicircles) in each figure were calculated and attributed to contributions arising from the grain boundaries (10^{-9}F) towards low frequencies and from the grains (10^{-10}F) towards high frequencies. Just noting that typical capacitance values from grains use to lie in the $10^{-11} - 10^{-12}$F range; the corresponding values found in the present work are sensibly higher, in line with the fact to be here dealing with a bulk contribution of ferroelectric type [144, 145].

The resistivity (ρ) and permittivity (ε) values estimated from the fitting of the impedance data are summarized in Table 10. From KBNN01 to KBNN03, on the on hand, values of both grain and grain-boundary resistivity decrease. This result is to be expected considering that the density of charge carriers (oxygen vacancies) increases, which traduces into enhanced defects-leaded electrical transport processes, noting that conductivity obeys the $\sigma = Nq\mu$ relation, where N refers to the density of charge carriers, while q and μ stand for their charge value and mobility, respectively. Furthermore, the behavior of permmittivity differs from grains to grain boundaries. For the former, no relevant changes were detected, indicating that oxygen vacancies have no influence on the bulk polarization process. While a similar trend might be supposed for the grain boundaries, this is contrasted with the observation of a clear increasing trend of permittivity when going from KBNN01 to KBNN03. In order to understand this result, it should be noted that the electrical parameters listed in Table 10 refer to their macroscopic values. The analysis below helps to get further insights into these data.

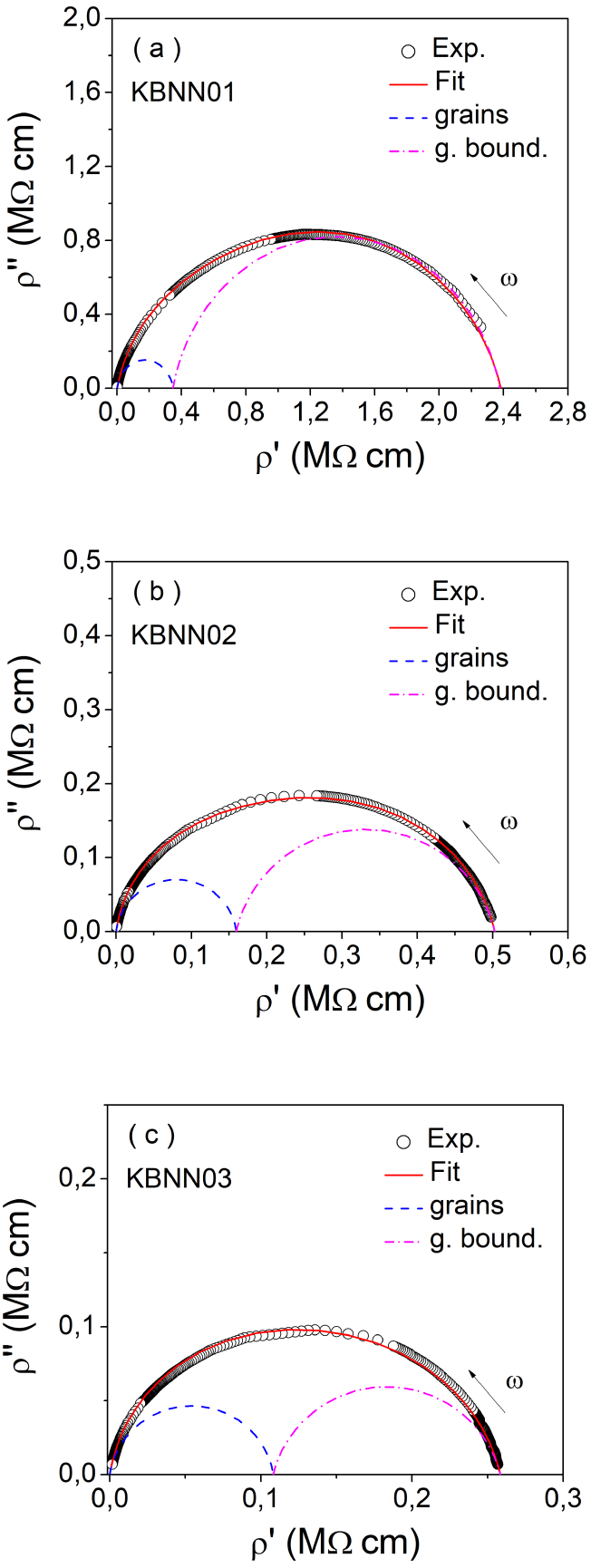

Figure 30 – Imaginary (ρ'') versus real parts (ρ') of resistivity measured at room temperature on the three KBNN-ceramic materials.

Table 10 – Values of macroscopic resistivity (ρ) and permittivity (ε) for grains (g) and grain boundaries (gb) measured at room temperature on the prepared ceramic samples.

Material	$\rho_g^{mac}(10^4\Omega \cdot m)$	$\varepsilon_g^{mac} \times 10^3$	$\rho_{gb}^{mac}(10^4\Omega \cdot m)$	$\varepsilon_{gb}^{mac} \times 10^3$
KBNN01	0.35	1.8	2.03	3.3
KBNN02	0.16	1.4	0.34	5.4
KBNN03	0.11	1.6	0.15	7.9

Considering the series-layer model applying between grains and grain boundaries, this is what the impedance data in figure 30 presuppose (because of occurrence of two semicircles), the connection between macroscopic and microscopic properties in such electroceramics can be demonstrated to obey: $\rho_g^{mac} \cong \rho_g^{mic}$ and $\varepsilon_g^{mac} \cong \varepsilon_g^{mic}$, while $\rho_{gb}^{mac} \cong \rho_{gb}^{mic}\phi/d$ and $\varepsilon_{gb}^{mac} \cong \varepsilon_{gb}^{mic}d/\phi$, where d and ϕ are, respectively, the average grain size and grain-to-grain contact thickness (with $d >> \phi$) [143]. In other words, macroscopic and microscopic dielectric properties from grains are expected to basically coincide, except for the influence of oxygen vacancy density on resistivity, as was discussed above. Meanwhile, ρ_{gb}^{mac} and ε_{gb}^{mac} are predicted to be grain size functions, in good agreement with the data trend, observed in Table 10: a decrease of the former and an increase of the latter with increasing grain-size from 0.32×10^{-6} m in KBNN01 to 0.51×10^{-6} m in KBNN03.

3.4 Optical Properties

In order to evaluate the potentiality of the materials for application in photovoltaic devices, since the main action in the photovoltaic conversion is the absorbance of light received, UV-Vis spectroscopy measurements were performed and the absorbance data were processed. Figure 31 shows the absorption spectra for the three samples. These results reveal a noticeable light absorption in the visible wavelength range (400–700 nm), with KBNN01 showing the higher light absorption. The occurrence of this absorption band has been associated to the fundamental characteristics of the metal-oxygen (A–O and B–O) bonds [146–148]. As aforementioned in the section 1.2, the excitation across the bandgap involves a charge transfer from the oxygen O-2p states, at the top of the valence band, to the transition-metal d states, at the bottom of the conduction band, thus leading the band-to-band transition from hybridized Ni-3d and O-2p to the Nb-4d states.

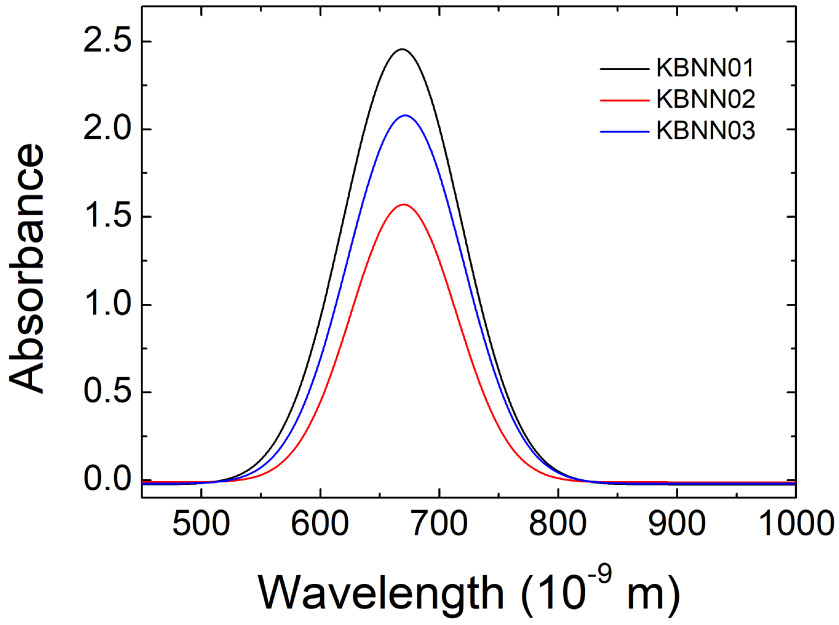

Figure 31 – UV-Vis absorption spectra of the studied KBNN samples.

Next, the optical bandgaps corresponding to these materials were here estimated from the Tauc's plot, $(\alpha h\nu)^2$ vs. $h\nu$, which is shown in figure 32. This data analysis approach applies for an allowed direct bandgap, the procedure of which yielded values scaling around (1.65 ± 0.02) eV for these KBNN materials, similar to the photon energy of visible light [10]. This value is considerably lower than the optical bandgap reported for pure $KNbO_3$ (KNO) [149] and other lead-free systems [38, 56, 150, 151] whose potentialities for photovoltaic applications have been explored. The lower bandgap value observed here in KBNN can be ascribed to the role played by the filled Ni-3d states [11], providing great potential for applications of this material as photocatalyst as well as in photovoltaic devices operating under visible light wavelength.

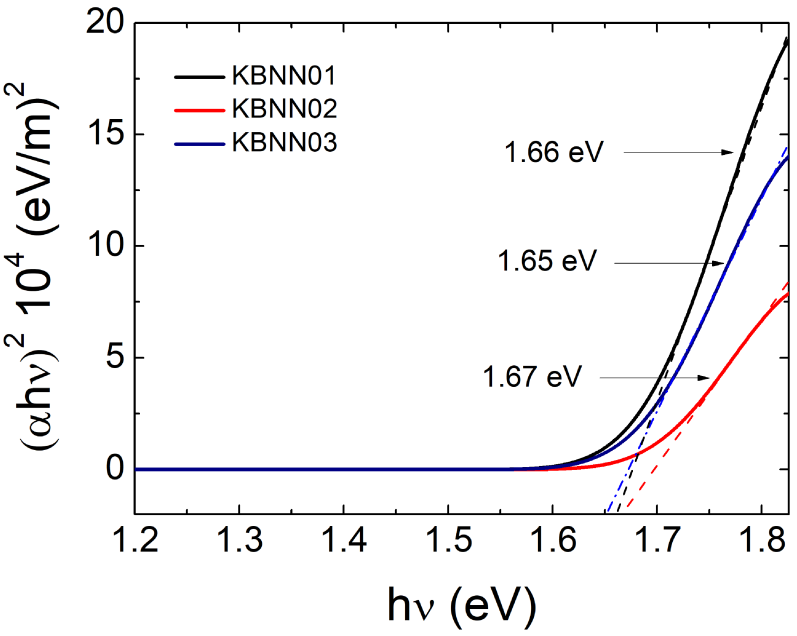

Figure 32 – The Tauc's plot of $(\alpha h\nu)^2$ vs. $h\nu$ for the absorption spectra of the studied KBNN samples.

Overall, the obtained results have shown that the studied materials reveal not only ferroelectric but also excellent photophysical properties, including enhanced photocatalytic activity. Indeed, the research presented here has been devoted to advanced understanding of the relationship between (micro)structural characteristics and electrical response in lead-free $KNbO_3$-based systems, mediated by oxygen-vacancy structural defects, which indeed has been scarcely reported in the current literature. Such analyses reveal to be crucial for getting further insights into the optimal photophysical properties of this material.

4 CONCLUSIONS

In summary, a systematic study on the photophysical properties have been carried out in lead-free KBNN-ceramics.

- A particular attention has been paid to the influence of the oxygen vacancy on the structural, microstructural, electrical as well as optical properties, including evaluation of the effect from grain-size, which in fact have not been previously reported in the literature for this system. This is the case of the unit-cell volume, lattice microstrain and Raman spectra evolution (long-range interaction included), where the defects-modulated (micro)structural characteristics were found to play a substantial inlfluence.

- In addition, the impedance spectroscopy analysis revealed a strong impact of these oxygen vacancy-related defects, as well as grain size, on the electrical response involved polarization mechanisms and charge transport strength promoting conduction processes from bulk and grain boundaries.

- Results revealed that the oxygen vacancies concentration have an important contribution on the dielectric response of these materials, and could be the main responsible mechanism for the dielectric relaxation processes observed for temperatures below the ferroelectric-paraelectric transition temperature in most of the studied ferroelectric systems.

- Finally, these KBNN-materials showed relatively-low optical bandgaps, lying in the visible light spectrum, which are considerably lower than those reported for pure $KNbO_3$ (KNO) and other commonly studied lead-free systems, making them promising candidates for applications in solar energy devices.

5 FUTURE PERSPECTIVES

As future perspectives, the analysis of dielectric properties as a function of the temperature has been proposed as a fundamental study, in order to investigate the phase transition characteristics as well as the influence of the oxygen vacancies on the polarization mechanisms, which govern the dielectric response. On the other hand, additional measurements of the Raman spectroscopy, but now with temperature, could also open the possibility to better investigate the vibrational properties, in particular the soft-mode contribution, as a function of the oxygen vacancy defects. Moreover, the investigation of the electronic properties, such as an analysis of the KBNN band structure through first-principles calculations, also reveals as a fundamental point for a better understanding of the electronic states and the conduction process of this material.

REFERENCES

[1] M. A. Green and A. Ho-Baillie, "Perovskite solar cells: the birth of a new era in photovoltaics," *ACS Energy Letters*, vol. 2, no. 4, pp. 822–830, 2017. https://doi.org/10.1021/acsenergylett.7b00137.

[2] J. Rödel, W. Jo, K. T. Seifert, E.-M. Anton, T. Granzow, and D. Damjanovic, "Perspective on the development of lead-free piezoceramics," *Journal of the American Ceramic Society*, vol. 92, no. 6, pp. 1153–1177, 2009. https://doi.org/10.1111/j.1551-2916.2009.03061.x.

[3] B. Zhang, J. Wu, X. Cheng, X. Wang, D. Xiao, J. Zhu, X. Wang, and X. Lou, "Lead-free piezoelectrics based on potassium–sodium niobate with giant d 33," *ACS applied materials & interfaces*, vol. 5, no. 16, pp. 7718–7725, 2013. https://doi.org/10.1021/am402548x.

[4] Z. Liu, W. Ren, P. Peng, S. Guo, T. Lu, Y. Liu, X. Dong, and G. Wang, "High performance $Bi_{0.5}Na_{0.5}Tio_3 - BiAlO_3 - K_{0.5}Na_{0.5}Nbo_3$ lead-free pyroelectric ceramics for thermal detectors," *Applied Physics Letters*, vol. 112, no. 14, p. 142903, 2018. https://doi.org/10.1063/1.5020424.

[5] S. Wemple, "Polarization fluctuations and the optical-absorption edge in $BaTiO_3$," *Physical Review B*, vol. 2, no. 7, p. 2679, 1970. https://doi.org/10.1103/PhysRevB.2.2679.

[6] V. Železnỳ, D. Chvostová, D. Šimek, F. Máca, J. Mašek, N. Setter, and Y. H. Huang, "The variation of $PbTiO_3$ bandgap at ferroelectric phase transition," *Journal of Physics: Condensed Matter*, vol. 28, no. 2, p. 025501, 2016. https://doi.org/10.1088/0953-8984/28/2/025501.

[7] A. Dhar and A. Mansingh, "Optical properties of reduced lithium niobate single crystals," *Journal of applied physics*, vol. 68, no. 11, pp. 5804–5809, 1990. https://doi.org/10.1063/1.346951.

[8] Q. Zhang, F. Xu, M. Xu, L. Li, Y. Lu, M. Li, P. Li, M. Li, G. Chang, and Y. He, "Lead-free perovskite ferroelectric thin films with narrow direct band gap suitable for solar cell applications," *Materials Research Bulletin*, vol. 95, pp. 56–60, 2017.https://doi.org/10.1016/j.materresbull.2017.07.020.

[9] C.-M. Hung, C.-S. Tu, W. Yen, L. Jou, M.-D. Jiang, and V. H. Schmidt, "Photovoltaic phenomena in $BiFeO_3$ multiferroic ceramics," *Journal of Applied Physics*, vol. 111, no. 7, p. 07D912, 2012. https://doi.org/10.1063/1.3675984.

[10] I. Grinberg, D. V. West, M. Torres, G. Gou, D. M. Stein, L. Wu, G. Chen, E. M. Gallo, A. R. Akbashev, P. K. Davies, *et al.*, "Perovskite oxides for visible-light-absorbing ferroelectric and photovoltaic materials," *Nature*, vol. 503, no. 7477, pp. 509–512, 2013. https://doi.org/10.1038/nature12622.

[11] W. Zhou, H. Deng, P. Yang, and J. Chu, "Structural phase transition, narrow band gap, and room-temperature ferromagnetism in $[KNbO_3]1-x[BaNi_{1/2}Nb_{1/2}O_{3-\delta}]x$ ferroelectrics," *Applied Physics Letters*, vol. 105, no. 11, p. 111904, 2014. https://doi.org/10.1063/1.4896317.

[12] F. Wang and A. M. Rappe, "First-principles calculation of the bulk photovoltaic effect in $KNbO_3$ and $(K,Ba)(Ni,Nb)O_{3-\delta}$," *Physical Review B*, vol. 91, no. 16, p. 165124, 2015. https://doi.org/10.1103/PhysRevB.91.165124.

[13] P. Wu, G. Wang, R. Chen, Y. Guo, X. Ma, and D. Jiang, "Enhanced visible light absorption and photocatalytic activity of $[KNbO_3]1-x[BaNi_{0.5}Nb_{0.5}O_{3-\delta}]$ x synthesized by sol–gel based pechini method," *RSC Advances*, vol. 6, no. 85, pp. 82409–82416, 2016. https://doi.org/10.1039/C6RA15288K.

[14] L. Yu, J. Jia, G. Yi, Y. Shan, and M. Han, "Bandgap tuning of $[KNbO_3]1-x[BaCO_{1/2}Nb_{1/2}O_{3-\delta}]x$ ferroelectrics," *Materials Letters*, vol. 184, pp. 166–168, 2016. https://doi.org/10.1016/j.matlet.2016.08.044.

[15] D. Nie, J. Zhang, W.-j. Deng, X. Chen, Z.-q. Mao, and L.-y. Tang, "Narrow band gap and room-temperature ferromagnetism in $KNb_{1-x}Fe_xO_{3-\delta}$," *Chinese Journal of Chemical Physics*, vol. 30, no. 1, pp. 97–102, 2017. https://doi.org/10.1063/1674-0068/30/cjcp1608154.

[16] L. Yu, H. Deng, W. Zhou, P. Yang, and J. Chu, "Band gap engineering and magnetic switching in a novel perovskite $(1-x)KNbO_3-xBaNb_{1/2}Fe_{1/2}O_3$," *Materials Letters*, vol. 202, pp. 39–43, 2017. https://doi.org/10.1016/j.matlet.2017.05.077.

[17] J. Valasek, "Piezo-electric and allied phenomena in rochelle salt," *Physical review*, vol. 17, no. 4, p. 475, 1921. https://doi.org/10.1103/PhysRev.17.475.

[18] Y. Xu, *Ferroelectric materials and their applications*. Elsevier, 2013.

[19] M. M. V. Petrovic and J. D. Bobic, "Perovskite and aurivillius: types of ferroelectric metal oxides," in *Magnetic, ferroelectric, and multiferroic metal oxides*, pp. 35–49, Elsevier, 2018. https://doi.org/10.1016/B978-0-12-811180-2.00002-5.

[20] F. Yang, G. Hu, B. Xu, W. Wu, C. Yang, and H. Wu, "Statistical mechanical origin of hysteresis in ferroelectrics," *Journal of Applied Physics*, vol. 112, no. 3, p. 034113, 2012. https://doi.org/10.1063/1.4745054.

[21] S.-W. Cheong and M. Mostovoy, "Multiferroics: a magnetic twist for ferroelectricity," *Nature materials*, vol. 6, no. 1, pp. 13–20, 2007. https://doi.org/10.1038/nmat1804.

[22] D. Khomskii, "Trend: Classifying multiferroics: Mechanisms and effects," *Physics*, vol. 2, p. 20, 2009. https://doi.org/10.1103/physics.2.20.

[23] N. A. Hill, "Why are there so few magnetic ferroelectrics?," *The journal of physical chemistry B*, vol. 104, no. 29, pp. 6694–6709, 2000. https://doi.org/10.1021/jp000114x.

[24] R. Seshadri and N. A. Hill, "Visualizing the role of Bi 6s "lone pairs" in the off-center distortion in ferromagnetic $BiMnO_3$," *Chemistry of materials*, vol. 13, no. 9, pp. 2892–2899, 2001. https://doi.org/10.1021/cm010090m.

[25] A. Levanyuk and D. G. Sannikov, "Improper ferroelectrics," *Soviet Physics Uspekhi*, vol. 17, no. 2, p. 199, 1974. https://doi.org/10.1070/pu1974v017n02abeh004336.

[26] K. Wang, J.-M. Liu, and Z. Ren, "Multiferroicity: the coupling between magnetic and polarization orders," *Advances in Physics*, vol. 58, no. 4, pp. 321–448, 2009. https://doi.org/10.1080/00018730902920554.

[27] N. Ikeda, H. Ohsumi, K. Ohwada, K. Ishii, T. Inami, K. Kakurai, Y. Murakami, K. Yoshii, S. Mori, Y. Horibe, *et al.*, "Ferroelectricity from iron valence ordering in the charge-frustrated system $LuFe_2O_4$," *Nature*, vol. 436, no. 7054, pp. 1136–1138, 2005. https://doi.org/10.1038/nature04039.

[28] J. Van Den Brink and D. I. Khomskii, "Multiferroicity due to charge ordering," *Journal of Physics: Condensed Matter*, vol. 20, no. 43, p. 434217, 2008. https://doi.org/10.1088/0953-8984/20/43/434217.

[29] M. Kenzelmann, A. B. Harris, S. Jonas, C. Broholm, J. Schefer, S. Kim, C. Zhang, S.-W. Cheong, O. P. Vajk, and J. W. Lynn, "Magnetic inversion symmetry breaking and ferroelectricity in $TbMnO_3$," *Physical review letters*, vol. 95, no. 8, p. 087206, 2005. https://doi.org/10.1103/PhysRevLett.95.087206.

[30] T. Kimura, T. Goto, H. Shintani, K. Ishizaka, T.-h. Arima, and Y. Tokura, "Magnetic control of ferroelectric polarization," *nature*, vol. 426, no. 6962, pp. 55–58, 2003. https://doi.org/10.1038/nature02018.

[31] N. Iwata and K. Kohn, "Dielectric anomalies at magnetic transitions of hexagonal rare earth manganese oxides $RmNO_3$," *Journal of the Physical Society of Japan*, vol. 67, no. 9, pp. 3318–3319, 1998. https://doi.org/10.1143/jpsj.67.3318.

[32] K. C. Kao, *Dielectric phenomena in solids*. Elsevier, 2004. https://doi.org/10.1016/B978-0-12-396561-5.X5010-5.

[33] P. R. Potnis, N.-T. Tsou, and J. E. Huber, "A review of domain modelling and domain imaging techniques in ferroelectric crystals," *Materials*, vol. 4, no. 2, pp. 417–447, 2011. https://doi.org/10.3390/ma4020417.

[34] L. Jin, F. Li, and S. Zhang, "Decoding the fingerprint of ferroelectric loops: comprehension of the material properties and structures," in *Progress in Advanced Dielectrics*, pp. 21–104, World Scientific, 2020. https://doi.org/10.1142/9789811210433_0002.

[35] G. Shirane, H. Danner, A. Pavlovic, and R. Pepinsky, "Phase transitions in ferroelectric $KNbO_3$," *Physical Review*, vol. 93, no. 4, p. 672, 1954. https://doi.org/10.1103/PhysRev.93.672.

[36] I. Golovina, V. Bryksa, V. Strelchuk, I. Geifman, and A. Andriiko, "Size effects in the temperatures of phase transitions in $KNbO_3$ nanopowder," *Journal of Applied Physics*, vol. 113, no. 14, p. 144103, 2013. https://doi.org/10.1063/1.4801794.

[37] S. Chatterjee and A. J. Pal, "Influence of metal substitution on hybrid halide perovskites: towards lead-free perovskite solar cells," *Journal of Materials Chemistry A*, vol. 6, no. 9, pp. 3793–3823, 2018. https://doi.org/10.1039/C7TA09943F.

[38] W. S. Choi, M. F. Chisholm, D. J. Singh, T. Choi, G. E. Jellison, and H. N. Lee, "Wide bandgap tunability in complex transition metal oxides by site-specific substitution," *Nature communications*, vol. 3, no. 1, pp. 1–6, 2012. https://doi.org/10.1038/ncomms1690.

[39] G. Zhang, H. Wu, G. Li, Q. Huang, C. Yang, F. Huang, F. Liao, and J. Lin, "New high t c multiferroics $KBiFe_2O_5$ with narrow band gap and promising photovoltaic effect," *Scientific reports*, vol. 3, no. 1, pp. 1–9, 2013. https://doi.org/10.1038/srep01265.

[40] S. Sharma, M. Tomar, A. Kumar, N. K. Puri, and V. Gupta, "Enhanced ferroelectric photovoltaic response of $BiFeO_3/BaTiO_3$ multilayered structure," *Journal of Applied Physics*, vol. 118, no. 7, p. 074103, 2015. https://doi.org/10.1063/1.4928964.

[41] E. Directive *et al.*, "Restriction of the use of certain hazardous substances in electrical and electronic equipment (RoHS)," *Off. J. Eur. Communities*, vol. 46, pp. 19–23, 2013.

[42] Y. Saito, H. Takao, T. Tani, T. Nonoyama, K. Takatori, T. Homma, T. Nagaya, and M. Nakamura, "Lead-free piezoceramics," *Nature*, vol. 432, no. 7013, pp. 84–87, 2004. https://doi.org/10.1038/nature03028.

[43] P. Kumari, R. Rai, S. Sharma, M. Shandilya, and A. Tiwari, "State-of-the-art of lead free ferroelectrics: A critical review," *Adv. Mater. Lett*, vol. 6, no. 6, pp. 453–484, 2015. https://doi.org/10.5185/amlett.2015.4086.

[44] V. M. Fridkin, *Photoferroelectrics*, vol. 9. Springer Science & Business Media, 2012.

[45] Y. Bai, H. Jantunen, and J. Juuti, "Energy harvesting research: the road from single source to multisource," *Advanced materials*, vol. 30, no. 34, p. 1707271, 2018. https://doi.org/10.1002/adma.201707271.

[46] Y. Bai, G. Vats, J. Seidel, H. Jantunen, and J. Juuti, "Boosting photovoltaic output of ferroelectric ceramics by optoelectric control of domains," *Advanced Materials*, vol. 30, no. 43, p. 1803821, 2018. https://doi.org/10.1002/adma.201803821.

[47] D. Bao, X. Yao, N. Wakiya, K. Shinozaki, and N. Mizutani, "Band-gap energies of sol-gel-derived $SrTiO_3$ thin films," *Applied Physics Letters*, vol. 79, no. 23, pp. 3767–3769, 2001. https://doi.org/10.1063/1.1423788.

[48] T. Qi, I. Grinberg, and A. M. Rappe, "Band-gap engineering via local environment in complex oxides," *Physical Review B*, vol. 83, no. 22, p. 224108, 2011. https://doi.org/10.1103/PhysRevB.83.224108.

[49] S. Yang, J. Seidel, S. Byrnes, P. Shafer, C.-H. Yang, M. Rossell, P. Yu, Y.-H. Chu, J. Scott, J. Ager, *et al.*, "Above-bandgap voltages from ferroelectric photovoltaic devices," *Nature nanotechnology*, vol. 5, no. 2, pp. 143–147, 2010. https://doi.org/10.1038/nnano.2009.451.

[50] S. M. Young and A. M. Rappe, "First principles calculation of the shift current photovoltaic effect in ferroelectrics," *Physical review letters*, vol. 109, no. 11, p. 116601, 2012. https://doi.org/10.1103/PhysRevLett.109.116601.

[51] Y. Bai, T. Siponkoski, J. Peräntie, H. Jantunen, and J. Juuti, "Ferroelectric, pyroelectric, and piezoelectric properties of a photovoltaic perovskite oxide," *Applied Physics Letters*, vol. 110, no. 6, p. 063903, 2017. https://doi.org/10.1063/1.4974735.

[52] C. Li, F. Wang, Y. Sun, K. Jiang, S. Gong, Z. Hu, Z. Zhou, X. Dong, J. Chu, *et al.*, "Lattice dynamics, phase transition, and tunable fundamental band gap of photovoltaic $(K, Ba)(Ni, Nb)O_{3-\delta}$ ceramics from spectral measurements and first-principles calculations," *Physical Review B*, vol. 97, no. 9, p. 094109, 2018. https://doi.org/10.1103/PhysRevB.97.094109.

[53] C. J. Hawley, L. Wu, G. Xiao, I. Grinberg, A. M. Rappe, P. K. Davies, and J. E. Spanier, "Structural and ferroelectric phase evolution in $[KNbO_3]1 - x[BaNi_{1/2}Nb_{1/2}O_{3-\delta}]x(x = 0, 0.1)$," *Physical Review B*, vol. 96, no. 5, p. 054117, 2017. https://doi.org/10.1103/PhysRevB.96.054117.

[54] B. Song, X. Wang, C. Xin, L. Zhang, B. Song, Y. Zhang, Y. Wang, J. Wang, Z. Liu, Y. Sui, *et al.*, "Multiferroic properties of Ba/Ni co-doped $KNbO_3$ with narrow band-gap," *Journal of Alloys and Compounds*, vol. 703, pp. 67–72, 2017. https://doi.org/10.1016/j.jallcom.2017.01.180.

[55] F. K. Rezaie, D. Panjwani, J. Nath, C. J. Fredricksen, I. O. Oladeji, and R. E. Peale, "Junctionless thin-film ferroelectric oxides for photovoltaic energy production," in *Energy Harvesting and Storage: Materials, Devices, and Applications V*, vol. 9115, p. 91150Q, International Society for Optics and Photonics, 2014. https://doi.org/10.1117/12.2050707.

[56] S. Basu, L. Martin, Y. Chu, M. Gajek, R. Ramesh, R. Rai, X. Xu, and J. Musfeldt, "Photoconductivity in $BiFeO_3$ thin films," *Applied Physics Letters*, vol. 92, no. 9, p. 091905, 2008. https://doi.org/10.1063/1.2887908.

[57] G. K. Singh, "Solar power generation by pv (photovoltaic) technology: A review," *Energy*, vol. 53, pp. 1–13, 2013. https://doi.org/10.1016/j.energy.2013.02.057.

[58] A. Polman, M. Knight, E. C. Garnett, B. Ehrler, and W. C. Sinke, "Photovoltaic materials: Present efficiencies and future challenges," *Science*, vol. 352, no. 6283, 2016. https://doi.org/10.1126/science.aad4424.

[59] C. Kittel, *Introduction to Solid State Physics*, vol. 8. John Willey & Sons, 2005.

[60] N. W. Ashcroft, N. D. Mermin, et al., *Solid state physics*, Holt, Rinehart and Winston, New York London, 1976.

[61] R. C. Gennari, R. Lang, J. A. Eiras, and M. H. Lente, "Effects of sintering process on the structural, dielectric, and optical absorption properties of $KNbO_3$-based ceramics," *Journal of the American Ceramic Society*, vol. 102, no. 7, pp. 3923–3931, 2019. https://doi.org/10.1111/jace.16267.

[62] G. H. Haertling, "Ferroelectric ceramics: history and technology," *Journal of the American Ceramic Society*, vol. 82, no. 4, pp. 797–818, 1999. https://doi.org/10.1111/j.1151-2916.1999.tb01840.x.

[63] K. Uchino, *Ferroelectric Devices*, vol. 321, Marcell Dekker Inc, New York, 2000.

[64] B. Jaffe, W. Cook, and H. Jaffe, *Piezoelectric Ceramics*, Elsevier, 1971.

[65] T. Choi, S. Lee, Y. Choi, V. Kiryukhin, and S.-W. Cheong, "Switchable ferroelectric diode and photovoltaic effect in $BiFeO_3$," *Science*, vol. 324, no. 5923, pp. 63–66, 2009. https://doi.org/10.1126/science.1168636.

[66] A. Zenkevich, Y. Matveyev, K. Maksimova, R. Gaynutdinov, A. Tolstikhina, and V. Fridkin, "Giant bulk photovoltaic effect in thin ferroelectric $BaTiO_3$ films," *Physical Review B*, vol. 90, no. 16, p. 161409, 2014. https://doi.org/10.1103/PhysRevB.90.161409.

[67] J. E. Spanier, V. M. Fridkin, A. M. Rappe, A. R. Akbashev, A. Polemi, Y. Qi, Z. Gu, S. M. Young, C. J. Hawley, D. Imbrenda, *et al.*, "Erratum: Power conversion efficiency exceeding the shockley–queisser limit in a ferroelectric insulator," *Nature Photonics*, vol. 10, no. 10, pp. 688–688, 2016. https://doi.org/10.1038/nphoton.2016.188.

[68] R. Nechache, C. Harnagea, S. Li, L. Cardenas, W. Huang, J. Chakrabartty, and F. Rosei, "Bandgap tuning of multiferroic oxide solar cells," *Nature Photonics*, vol. 9, no. 1, pp. 61–67, 2015. https://doi.org/10.1038/nphoton.2014.255.

[69] S. Thakoor and A. P. Thakoor, "Thin film ferroelectric electro-optic memory," Apr. 27 1993. US Patent 5,206,829.

[70] M. J. Pitcher, P. Mandal, M. S. Dyer, J. Alaria, P. Borisov, H. Niu, J. B. Claridge, and M. J. Rosseinsky, "Tilt engineering of spontaneous polarization and magnetization above 300 K in a bulk layered perovskite," *Science*, vol. 347, no. 6220, pp. 420–424, 2015. https://doi.org/10.1126/science.1262118.

[71] S. Yang, L. Martin, S. Byrnes, T. Conry, S. Basu, D. Paran, L. Reichertz, J. Ihlefeld, C. Adamo, A. Melville, *et al.*, "Photovoltaic effects in $BiFeO_3$," *Applied Physics Letters*, vol. 95, no. 6, p. 062909, 2009. https://doi.org/10.1063/1.3204695.

[72] H. Huang, "Ferroelectric photovoltaics," *Nature photonics*, vol. 4, no. 3, pp. 134–135, 2010. https://doi.org/10.1038/nphoton.2010.15.

[73] V. Fridkin, "Bulk photovoltaic effect in noncentrosymmetric crystals," *Crystallography Reports*, vol. 46, no. 4, pp. 654–658, 2001. https://doi.org/10.1134/1.1387133.

[74] J. T. Irvine, D. C. Sinclair, and A. R. West, "Electroceramics: characterization by impedance spectroscopy," *Advanced materials*, vol. 2, no. 3, pp. 132–138, 1990. https://doi.org/10.1002/adma.19900020304.

[75] M. N. Rahaman, *Ceramic processing*. CRC press, 2017. https://doi.org/10.1201/9781315157160.

[76] Y. Garbovskiy, O. Zribi, and A. Glushchenko, "Emerging applications of ferroelectric nanoparticles in materials technologies, biology and medicine," *Advances in Ferroelectrics*, pp. 475–498, 2012. https://doi.org/10.5772/52516.

[77] S. Ivanov, "Multiferroic complex metal oxides: Main features of preparation, structure, and properties," in *Science and Technology of Atomic, Molecular, Condensed Matter & Biological Systems*, vol. 2, pp. 163–238, Elsevier, 2012. https://doi.org/10.1016/B978-0-44-453681-5.00007-8.

[78] S. Kasap and P. Capper, *Springer handbook of electronic and photonic materials*. Springer, 2017. https://doi.org/10.1007/978-3-319-48933-9.

[79] J. Hojo, *Materials Chemistry of Ceramics*. Springer, 2019.

[80] C. B. Carter, M. G. Norton, *et al.*, *Ceramic materials: science and engineering*, vol. 716. Springer, 2007.

[81] A. C. d. Silva, "Síntese de cerâmicas ferroelétricas de PLZT–análise composicional e mecanismos de vacâncias.," 2013. Dissertação de Mestrado, Universidade Estadual Paulista, Departamento de Física e Química, Programa de Pós-Graduação em Ciência dos Materiais. http://hdl.handle.net/11449/111104.

[82] W. D. Kingery, H. K. Bowen, and D. R. Uhlmann, *Introduction to ceramics*, vol. 17. John wiley & sons, 1976.

[83] T. A. Ring, *Fundamentals of ceramic powder processing and synthesis*. Elsevier, 1996.

[84] A. Le Bail, L. M. Cranswick, I. Madsen, A. Fitch, R. Allmann, C. Giacovazzo, A. Altomare, J. K. Cockcroft, R. Caliandro, P. Norby, *et al.*, *Powder diffraction: theory and practice. Edited by RE Dinnebier and SJL Billinge*. Royal society of chemistry, 2008.

[85] V. Pecharsky and P. Zavalij, *Fundamentals of powder diffraction and structural characterization of materials*. Springer Science & Business Media, 2005.

[86] B. D. Cullity, *Elements of X-ray Diffraction*. Addison-Wesley Publishing, 1956.

[87] Y. Waseda, E. Matsubara, and K. Shinoda, *X-ray diffraction crystallography: introduction, examples and solved problems*. Springer Science & Business Media, 2011. https://doi.org/10.1007/978-3-642-16635-8.

[88] W. D. Callister and D. G. Rethwisch, *Materials science and engineering: an introduction*, vol. 10. Wiley New York, 2018.

[89] H. M. Rietveld, *The Structures of p-diphenylbenzene, diphenyl and cadmium n-butyl xanthate*. PhD thesis, University of Western Australia, 1963.

[90] E. J. Mittemeijer and P. Scardi, *Diffraction analysis of the microstructure of materials*, vol. 68. Springer Science & Business Media, 2013. https://doi.org/10.1007/978-3-662-06723-9.

[91] R. A. Young, *The Rietveld Method*, vol. 5. Oxford University Press, 1995.

[92] Y. T. Prabhu, K. V. Rao, V. S. S. Kumar, and B. S. Kumari, "X-ray analysis by williamson-hall and size-strain plot methods of ZnO nanoparticles with fuel variation," *World Journal of Nano Science and Engineering*, vol. 2014, 2014. https://doi.org/10.4236/wjnse.2014.41004.

[93] G. Williamson and W. Hall, "X-ray line broadening from filed aluminium and wolfram," *Acta metallurgica*, vol. 1, no. 1, pp. 22–31, 1953. https://doi.org/10.1016/0001-6160(53)90006-6.

[94] A. K. Zak, W. A. Majid, M. E. Abrishami, and R. Yousefi, "X-ray analysis of zno nanoparticles by williamson–hall and size–strain plot methods," *Solid State Sciences*, vol. 13, no. 1, pp. 251–256, 2011. https://doi.org/10.1016/j.solidstatesciences.2010.11.024.

[95] C. V. Raman and K. S. Krishnan, "A new type of secondary radiation," *Nature*, vol. 121, no. 3048, pp. 501–502, 1928. https://doi.org/10.1038/121501c0.

[96] J. R. Ferraro, *Introductory Raman Spectroscopy*. Elsevier, 2003.

[97] E. Smith and G. Dent, "Modern raman spectroscopy: a practical approach," 2005.

[98] R. Loudon, "The raman effect in crystals," *Advances in Physics*, vol. 13, no. 52, pp. 423–482, 1964. https://doi.org/10.1080/00018736400101051.

[99] Y. I. Yuzyuk, "Raman scattering spectra of ceramics, films, and superlattices of ferroelectric perovskites: A review," *Physics of the Solid State*, vol. 54, no. 5, pp. 1026–1059, 2012. https://doi.org/10.1134/s1063783412050502.

[100] J. Goldstein, *Practical scanning electron microscopy: electron and ion microprobe analysis*. Springer Science & Business Media, 2012. https://doi.org/10.1007/978-1-4613-4422-3.

[101] J. R. Macdonald and W. B. Johnson, "Fundamentals of impedance spectroscopy," *Impedance spectroscopy: theory, experiment, and applications*, pp. 1–20, 2018. https://doi.org/10.1002/9781119381860.ch1.

[102] M. Aljarrah and F. Salman, "A simple analysis of impedance spectroscopy," *Journal of The Institution of Engineers (India): Series D*, pp. 1–6, 2021. https://doi.org/10.1007/s40033-021-00252-7.

[103] A. Delgado, M. F. García-Sánchez, J.-C. M'Peko, A. R. Ruiz-Salvador, G. Rodríguez-Gattorno, Y. Echevarría, and F. Fernández-Gutierrez, "An elementary picture of dielectric spectroscopy in solids: physical basis," *Journal of chemical education*, vol. 80, no. 9, p. 1062, 2003. https://doi.org/10.1021/ed080p1062.

[104] E. Von Hauff, "Impedance spectroscopy for emerging photovoltaics," *The Journal of Physical Chemistry C*, vol. 123, no. 18, pp. 11329–11346, 2019. https://doi.org/10.1021/acs.jpcc.9b00892.

[105] A. Shaheen, M. Maghrabi, F. Salman, and Z. Khattari, "Effects of temperature and frequency on the dielectric properties of $AgPO_3$ glass," *Applied Physics A*, vol. 124, no. 1, p. 54, 2018. https://doi.org/10.1007/s00339-017-1484-2.

[106] P. Debye, *Polar Molecules*. Dover Publications: New York, 1945.

[107] K. S. Cole and R. H. Cole, "Dispersion and absorption in dielectrics i. alternating current characteristics," *The Journal of chemical physics*, vol. 9, no. 4, pp. 341–351, 1941. https://doi.org/10.1063/1.1750906.

[108] L. Dissado and R. Hill, "Dielectric behaviour of materials undergoing dipole alignment transitions," *Philosophical Magazine B*, vol. 41, no. 6, pp. 625–642, 1980. https://doi.org/10.1080/13642818008245413.

[109] S. Havriliak and S. Negami, "A complex plane analysis of α-dispersions in some polymer systems," in *Journal of Polymer Science Part C: Polymer Symposia*, vol. 14, pp. 99–117, Wiley Online Library, 1966. https://doi.org/10.1002/polc.5070140111.

[110] A. K. Jonscher, "The 'universal'dielectric response," *nature*, vol. 267, no. 5613, pp. 673–679, 1977. https://doi.org/10.1038/267673a0.

[111] A. Jonscher, "A new understanding of the dielectric relaxation of solids," *Journal of Materials Science*, vol. 16, no. 8, pp. 2037–2060, 1981. https://doi.org/10.1007/bf00542364.

[112] A. K. Jonscher, "Dielectric relaxation in solids," *Journal of Physics D: Applied Physics*, vol. 32, no. 14, p. R57, 1999. https://doi.org/10.1088/0022-3727/32/14/201.

[113] M. Picollo, M. Aceto, and T. Vitorino, "Uv-vis spectroscopy," *Physical sciences reviews*, vol. 4, no. 4, 2019. https://doi.org/10.1515/psr-2018-0008.

[114] A. Monte, A. Reis, L. C. Junior, and A. Antunes, "Preparation and quantitative characterization of polydimethylsiloxane optical phantoms with zinc-phthalocyanine dye absorbers," *Applied optics*, vol. 57, no. 20, pp. 5865–5871, 2018. https://doi.org/10.1364/AO.57.005865.

[115] H. G. Brittain, *Spectroscopy of pharmaceutical solids*. CRC Press, 2006. https://doi.org/10.1201/9780849361333.

[116] C. Tang, M. Meyer, B. L. Darby, B. Auguié, and E. C. Le Ru, "Realistic ports in integrating spheres: reflectance, transmittance, and angular redirection," *Applied optics*, vol. 57, no. 7, pp. 1581–1588, 2018. https://doi.org/10.1364/AO.57.001581.

[117] Z. Chen, H. N. Dinh, E. Miller, *et al.*, *Photoelectrochemical water splitting*, vol. 344. Springer, 2013.

[118] J.-H. Lambert, *JH Lambert,... Photometria, sive de Mensura et gradibus luminis, colorum et umbrae*. sumptibus viduae E. Klett, 1760.

[119] A. Beer, "Bestimmung der absorption des rothen lichts in farbigen flussigkeiten," *Ann. Physik*, vol. 162, pp. 78–88, 1852. https://doi.org/10.1002/andp.18521620505.

[120] D. Wood and J. Tauc, "Weak absorption tails in amorphous semiconductors," *Physical review B*, vol. 5, no. 8, p. 3144, 1972. https://doi.org/10.1103/PhysRevB.5.3144.

[121] E. Davis and N. Mott, "Conduction in non-crystalline systems v. conductivity, optical absorption and photoconductivity in amorphous semiconductors," *Philosophical magazine*, vol. 22, no. 179, pp. 0903–0922, 1970. https://doi.org/10.1080/14786437008221061.

[122] F.-P. Koffyberg, K. Dwight, and A. Wold, "Interband transitions of semiconducting oxides determined from photoelectrolysis spectra," *Solid State Communications*, vol. 30, no. 7, pp. 433–437, 1979. https://doi.org/10.1016/0038-1098(79)91182-7.

[123] S. Chugunov and C. Li, "Parallel implementation of inverse adding-doubling and monte carlo multi-layered programs for high performance computing systems with shared and distributed memory," *Computer Physics Communications*, vol. 194, pp. 64–75, 2015. https://doi.org/10.1016/j.cpc.2015.02.029.

[124] A. Hewat, "Soft modes and the structure, spontaneous polarization and curie constants of perovskite ferroelectrics: tetragonal potassium niobate," *Journal of Physics C: Solid State Physics*, vol. 6, no. 6, p. 1074, 1973. https://doi.org/10.1088/0022-3719/6/6/020.

[125] S. Sasaki, K. Fujino, and Y. Takéuchi, "X-ray determination of electron-density distributions in oxides, MgO, MnO, CoO, and NiO, and atomic scattering factors of their constituent atoms," *Proceedings of the Japan Academy, Series B*, vol. 55, no. 2, pp. 43–48, 1979. https://doi.org/10.2183/pjab.55.43.

[126] J. Rodríguez-Carvajal, "Recent advances in magnetic structure determination by neutron powder diffraction," *Physica B: Condensed Matter*, vol. 192, no. 1-2, pp. 55–69, 1993. https://doi.org/10.1016/0921-4526(93)90108-I.

[127] F. Karlsruhe, "Inorganic crystal structure database (icsd-2014)," 2014.

[128] T. Hoshina, R. Sase, J. Nishiyama, H. Takeda, and T. Tsurumi, "Effect of oxygen vacancies on intrinsic dielectric permittivity of strontium titanate ceramics," *Journal of the Ceramic Society of Japan*, vol. 126, no. 5, pp. 263–268, 2018. https://doi.org/10.2109/jcersj2.17250.

[129] E. Buixaderas, I. Gregora, M. Savinov, J. Hlinka, L. Jin, D. Damjanovic, B. Malic, *et al.*, "Compositional behavior of raman-active phonons in $Pb(Zr_{1-x}Ti_x)O_3$ ceramics," *Physical Review B*, vol. 91, no. 1, p. 014104, 2015. https://doi.org/10.1103/PhysRevB.91.014104.

[130] C. Pascual-Gonzalez, G. Schileo, and A. Feteira, "Band gap narrowing in ferroelectric $KNbO_3 - Bi(Yb, Me)O_3$ (Me= Fe or Mn) ceramics," *Applied Physics Letters*, vol. 109, no. 13, p. 132902, 2016. https://doi.org/10.1063/1.4963699.

[131] L. Luisman, A. Feteira, and K. Reichmann, "Weak-relaxor behaviour in Bi/Yb-doped $KNbO_3$ ceramics," *Applied Physics Letters*, vol. 99, no. 19, p. 192901, 2011. https://doi.org/10.1063/1.4963699.

[132] S. Abhinay and R. Mazumder, "Synthesis of ferroelectric $0.9KNbO_3 - 0.1Ba(Nb_{1/2}Ni_{1/2})O_{3-\delta}$ through one step hydrothermal reaction: Characterization and photocatalytic properties," *Journal of Solid State Chemistry*, vol. 289, p. 121362, 2020. https://doi.org/10.1016/j.jssc.2020.121362.

[133] S. Sriphan, S. Kiravittaya, P. Kidkhunthod, and T. Bongkarn, "Insight into an atomic arrangement of $[KNbO_3]0.9 - [BaNi_{0.5}Nb_{0.5}O_3]0.1$ powder formed at various calcination temperatures by x-ray absorption spectroscopy," *Results in physics*, vol. 7, pp. 1550–1555, 2017. https://doi.org/10.1016/j.rinp.2017.04.029.

[134] H. Ghoudi, S. Chkoundali, Z. Raddaoui, and A. Aydi, "Structure properties and dielectric relaxation of $Ca_{0.1}Na_{0.9}Ti_{0.1}Nb_{0.9}O_3$ ceramic," *RSC Advances*, vol. 9, no. 44, pp. 25358–25367, 2019. https://doi.org/10.1039/C9RA03967H.

[135] A. Z. Simões, F. G. Garcia, and C. dos Santos Riccardi, "Rietveld analysys and electrical properties of lanthanum doped $BiFeO_3$ ceramics," *Materials Chemistry and Physics*, vol. 116, no. 2-3, pp. 305–309, 2009. https://doi.org/10.1016/j.matchemphys.2009.04.036.

[136] S. Pradhan and B. Roul, "Effect of gd doping on structural, electrical and magnetic properties of $BiFeO_3$ electroceramic," *Journal of Physics and Chemistry of Solids*, vol. 72, no. 10, pp. 1180–1187, 2011. https://doi.org/10.1016/j.jpcs.2011.07.017.

[137] M. Choi, F. Oba, Y. Kumagai, and I. Tanaka, "Anti-ferrodistortive-like oxygen-octahedron rotation induced by the oxygen vacancy in cubic $SrTiO_3$," *Advanced Materials*, vol. 25, no. 1, pp. 86–90, 2013. https://doi.org/10.1002/adma.201203580.

[138] T. Teranishi, R. Kanemoto, H. Hayashi, and A. Kishimoto, "Effect of the $(Ba + Sr)/Ti$ ratio on the microwave-tunable properties of $Ba_{0.6}Sr_{0.4}TiO_3$ ceramics," *Journal of the American Ceramic Society*, vol. 100, no. 3, pp. 1037–1043, 2017. https://doi.org/10.1111/jace.14700.

[139] M. Wieser, "Atomic weights of the elements 2005 (IUPAC Technical Report)," *Pure and Applied Chemistry*, vol. 78, no. 11, pp. 2051–2066, 2006. https://doi.org/10.1351/pac200678112051.

[140] V. V. Daniel, *Dielectric relaxation.* Academic press: New York, 1967. https://doi.org/10.1016/0022-2860(68)80044-4.

[141] J. Blakemore, *Solid State Physics*, vol. 2. Cambridge University Press, 1985. https://doi.org/10.1107/S0108767386099646.

[142] F. U. Ermawati, S. Pratapa, S. Suasmoro, T. Hübert, and U. Banach, "Preparation and structural study of $Mg_{1-x}Zn_xTiO_3$ ceramics and their dielectric properties from 1 Hz to 7.7 GHz," *Journal of Materials Science: Materials in Electronics*, vol. 27, no. 7, pp. 6637–6645, 2016. https://doi.org/10.1007/s10854-016-4610-6.

[143] E. Barsoukov and J. R. Macdonald, *Impedance spectroscopy: theory, experiment, and applications.* John Wiley & Sons, 2005. https://doi.org/10.1002/0471716243.

[144] A. Delgado, M. F. García-Sánchez, J.-C. M'Peko, A. R. Ruiz-Salvador, G. Rodríguez-Gattorno, Y. Echevarría, and F. Fernández-Gutierrez, "An elementary picture of dielectric spectroscopy in solids: physical basis," *Journal of chemical education*, vol. 80, no. 9, p. 1062, 2003. https://doi.org/10.1021/ed080p1062.

[145] J. Fletcher, A. West, and J. Irvine, "The AC impedance response of the physical interface between yttria-stabilized zirconia and $YBa_2Cu_3O_{7-x}$," *Journal of the Electrochemical Society*, vol. 142, no. 8, p. 2650, 1995. https://doi.org/10.1149/1.2050068.

[146] E. Burtsev, *On the theory of optical absorption spectra of ferroelectric crystals,* 1973. Taylor & Francis. https://doi.org/10.1080/00150197308237689.

[147] J. Y. Han and C. W. Bark, "Structural and optical properties of Fe doped bismuth titanate thin film deposited by RF sputtering," *Japanese Journal of Applied Physics*, vol. 55, no. 2S, p. 02BC09, 2016. https://doi.org/10.7567/jjap.55.02bc09.

[148] H. Sun, Y. Wu, X. Xie, Y. Lu, T. Yao, J. Zhong, and X. Chen, "Ferroelectric, magnetic, and optical properties of aurivillius compound $Bi_5FeTi_{2.5}Co_{0.5}O_{15}$," *Journal of Materiomics*, vol. 4, no. 4, pp. 353–359, 2018. https://doi.org/10.1016/j.jmat.2018.09.005.

[149] Q.-P. Ding, Y.-P. Yuan, X. Xiong, R.-P. Li, H.-B. Huang, Z.-S. Li, T. Yu, Z.-G. Zou, and S.-G. Yang, "Enhanced photocatalytic water splitting properties of $KNbO_3$ nanowires synthesized through hydrothermal method," *The Journal of Physical Chemistry C*, vol. 112, no. 48, pp. 18846–18848, 2008. https://doi.org/10.1021/jp8042768.

[150] M. Alexe and D. Hesse, "Tip-enhanced photovoltaic effects in bismuth ferrite," *Nature communications*, vol. 2, no. 1, pp. 1–5, 2011. https://doi.org/10.1038/ncomms1261.

[151] P. P. Biswas, S. Pal, V. Subramanian, and P. Murugavel, "Large photovoltaic response in rare-earth doped $BiFeO_3$ polycrystalline thin films near morphotropic phase boundary composition," *Applied Physics Letters*, vol. 114, no. 17, p. 173901, 2019. https://doi.org/10.1063/1.5090911.